The Thesis Committee for Michael L. Elmuccio
Certifies that this is the approved version of the following thesis:

Progress towards Visualizing the Controlled Assembly of Gold Nanoparticles on DNA

APPROVED BY

SUPERVISING COMMITTEE:

Supervisor:

Brent L. Iverson

Eric Anslyn

Progress towards Visualizing the Controlled Assembly of Gold Nanoparticles on DNA

by

Michael L. Elmuccio, B.S.

Thesis

Presented to the Faculty of the Graduate School of

The University of Texas at Austin

in Partial Fulfillment

of the Requirements

for the Degree of

Master of Arts

The University of Texas at Austin

May 2011

Acknowledgements

Abstract

Progress towards Visualizing the Controlled Assembly of Gold Nanoparticles on DNA

Michael L. Elmuccio, MA

The University of Texas at Austin, 2011

Supervisor: Brent Iverson

Our laboratory has used the 1,4,5,8 Naphthalenetetracarboxylic diimide (NDI) unit to develop threading polyintercalators that bind DNA with the NDI units intercalated in between GpG steps and two different peptide linkers, which connect the NDI units, situated in either the major or minor grooves. The first generation bisintercalators, G_3K and βAla_3K, were shown to bind two different sequences of DNA, where the peptide linkers reside in the major and minor grooves respectively. These binding modules were then combined to generate threading polyintercalators that bound different DNA sequences with simultaneous occupation of both grooves. In particular, a cyclic bisintercalator was designed and DNAse I footprinting revealed a strong preference for

the sequence 5'-GGTACC-3'. NMR structural studies of the complex with d(CGGTACCG)$_2$ verified a pseudocatenane structure in which the NDI units reside four base pairs apart, with one linker located in the minor groove and the other in the major groove. This was the first structurally well-characterized pseudocatenane complex between a sequence-specific cyclic bisintercalator and its preferred binding sequence.

The ability to simultaneously occupy both groves of the same sequence is interesting for several reasons. Most significantly, it raises questions about a complex DNA intercalator's ability to locate its preferred sequence within a long strand of DNA. In order to directly assess this, the intercalator was modified (**CBI-Cys)** to incorporate a gold nanoparticle probe to allow for the direct visualization of the intercalator locating its preferred sequence within a long DNA strand. The appropriate protocols to visualize DNA using electron and atomic force microscopy were unsuccessful; however, the foundation has been set for future work to develop the appropriate method to determine the mechanism by which the cyclic bisintercalator locates its preferred sequence.

Additionally, the bisintercalators developed in our laboratory offered a unique opportunity to exploit their sequence specificity for controlled nanoparticle assembly. Over the past decade, nanoparticles and DNA have been used to develop novel nanoparticle assembly systems with the goal of developing electronic devices and nanomaterials. The **G$_3$K** bisintercalator was synthetically modified to incorporate a gold nanoparticle probe. This intercalator-nanoparticle conjugate, **BisKC•Au**, maintained its binding specificity (5'-GGTACC-3') to a modified DNA fragment containing multiple **G$_3$K** binding sites.

The atomic force microscope has become the most promising tool in visualizing individual DNA molecules. A modified procedure utilized **APS** to allow for the direct visualizing of plasmid DNA. The framework is now in place to confirm the controlled

assembly of the gold nanoparticles. This protocol can then be used for the **βAla₃K** bisintercalator to lead to the development of a nanoparticle assembly system that can precisely control the organization of multiple types of nanoparticles.

Table of Contents

List of Tables

List of Figures

Chapter 1: Introduction to DNA Intercalators and to the Investigations of DNA Binding Complexes Using Electron and Atomic Force Microscopy

1.1 DNA STRUCTURE

The DNA double helix contains two individual strands of DNA that are assembled according to Watson-Crick base-pairing rules: adenosine pairs with thymine and guanidine pairs with cytosine. The bases are covalently linked by a sugar-phosphate backbone. Relative to each other, the sugar-phosphate backbone is highly polar and negatively charged, while the bases are nonpolar and provide hydrophobic aromatic surfaces. During double helix formation, the phosphate-sugar backbone becomes exposed to the aqueous environment while the hydrophobic base pairs are stacked in the interior to minimize contact with the water environment. When the bases become stacked, the water molecules around the hydrophobic bases can make more hydrogen bonds with each other, which results in a desolvation driving force for double-helix formation.

DNA exists in solution in three major forms: A, B, and Z. B-DNA is the form that predominates under physiological conditions. The right-handed double helix of DNA has 10 base pairs per complete turn (approximately 34 Å per 10 bp turn) with the anti-parallel strands linked by Watson-Crick pairing rules. There is a wide, shallow major groove and a narrow, deep minor groove. The A-form of DNA generally exists in solutions with decreased water concentrations. The A-form DNA structure is more compact and wider than B-form DNA, with 11 base pairs per turn. The Z-DNA form of DNA exists at times when there are repeats of C and G base pairs, and exists as a left-handed helix with 12 base pairs per turn. It is longer and narrower compared to B-form DNA, but this form is

rare. DNA structure is determined by a variety of factors including sequence, solvent, counter-ion environment, ligand binding, and topological strain. (Ivanov 2003, Mazur).

1.2 DNA BINDING THERMODYNAMICS

The thermodynamic parameters of DNA-binding complexes have been thoroughly reviewed, including detailed understandings of DNA-drug (Chaires 1998, Haq and Ladburry 2000) and DNA-transcriptional factor (Patikoglu and Burley 1997) interactions. The Gibbs free energy (ΔG) associated with a small-molecule-binding DNA can be reasonably simplified into five terms using the following equation. The focus of this equation is primarily concerned with DNA intercalators and groove-binding molecules. ΔG_{obs} is the experimentally observed binding free energy, estimated from the association constant K using the standard Gibbs relationship, $\Delta G_{obs} = -RT \ln K$.

$$\Delta G_{obs} = \Delta G_{conf} + \Delta G_{t+r} + \Delta G_{hyd} + \Delta G_{pe} + \Delta G_{mol}$$

ΔG_{conf} refers to the free energy cost of conformational changes. For intercalation, the DNA base pairs must separate to allow for the insertion of the intercalating moiety. This results in local unwinding of the DNA helix. The formation of this intercalation cavity will certainly cost energy, with estimated costs of 4-10 kcal/mol. For groove-binding molecules, this type of conformational change is not likely and the free energy cost for this term contributes minimally to the overall ΔG.

ΔG_{t+r} takes into consideration the entropic cost of binding as the formation of a bimolecular complex will result in the loss of translation and rotational degrees of freedom. While the exact numbers have been highly debated, the approximation of a 15 kcal/mol entropic penalty was investigated and it was concluded that this number was an appropriate estimation (Spolar and Record, 1994). These numbers have not been fully

investigated for groove binding molecules, but one can assume that at the very least, the overall entropy value would be unfavorable, as the groove binding still leads to the formation of a bimolecular complex.

Since these two previous parameters clearly indicate unfavorable binding thermodynamics, some interactions must provide enough favorable energetic contributions to overcome these positive free energy contributions and allow for DNA binding. ΔG_{hyd} is the free energy contribution that results from the hydrophobic effect. Since intercalators and groove binders contain hydrophobic aromatic rings, the transfer of these systems from the aqueous environment into the DNA grooves or interior of the helix would be energetically favorable. Solvent-accessible surface area and heat capacity changes have been used to quantify this energy contribution. These studies have shown that the favorable hydrophobic effect provides enough energy to overcome the unfavorable energetic costs, and is the largest driving force for DNA binding, in particular DNA intercalation (Spolar and Record, 1994, Chaires, 1998).

As the binding molecules intercalate, or occupy the grooves, they will release the bound counter ions into solution, resulting in a favorable energetic contribution to binding known as the polyelectrolyte effect (ΔG_{pe}) (Manning, 1978). It has been experimentally determined that this contribution, while favorable, is not overly significant when compared to the favorable energy received from the hydrophobic effect, and is not considered a primary driving force.

The final classes of interactions include the non-covalent molecular interactions that occur upon binding. ΔG_{mol} refers to hydrogen bonding, van der Waals contacts, and electrostatic bonding. There seems to be a disagreement between experimentally determined values for these types of interactions. It is not entirely clear how each of these interactions affect the overall binding energy. Hydrogen bonding can be

investigated by high-resolution structural studies of the DNA-molecular complex but it may not be possible to exactly determine each energetic contribution. Hydrogen bonding does likely contribute favorably to the enthalpy associated with binding and may have a role in defining particular sequence specificities (Chaires, 1998).

1.3 SMALL MOLECULES BINDING DNA

The two most common types of DNA binding modes are intercalation and groove binding; some molecules exhibit both of these modes.

1.3.1 Groove Binding Molecules

Netropsin and distamycin are two of the most well-studied minor groove-binding molecules. Both of these molecules contain aromatic pyrrole units linked by amide bonds and bind AT rich sequences of DNA. These molecules are structurally flat, with a crescent shape to them that allows for a favorable interactions via the curvature of the minor groove of DNA. The driving force for this interaction comes from a combination of the hydrophobic transfer of the polyamide moiety into the DNA grooves, as well as favorable van der Waals and hydrogen bonding interactions that contributes to a favorable ΔG. (Chaires and Bailly, 1998). Distamycin, isolated as a natural product, was one of the first naturally occurring minor grove binding DNA molecules discovered (Hahn, 1975). It was later determined that distamycin bound to A,T sequences of DNA as an antiparallel 2:1 complex as well as a 1:1 complex (Pelton and Wemmer, 1989).
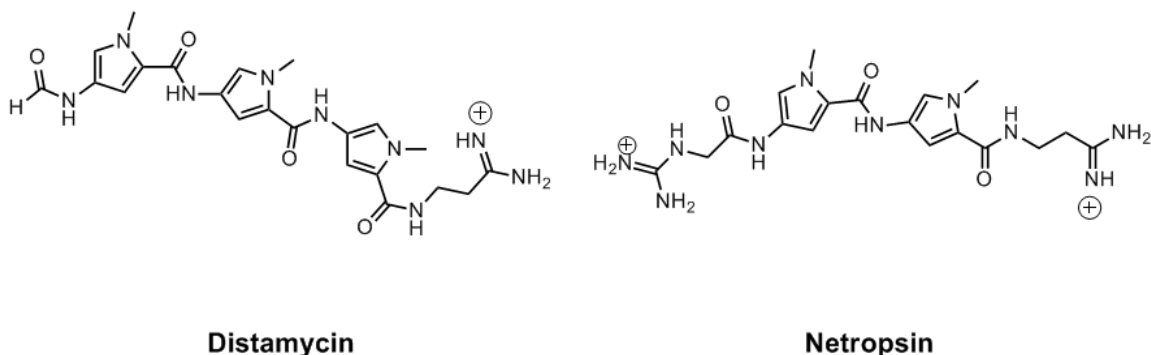
Figure 1.1 Structures of distamycin and netropsin.

The interaction of netropsin with a DNA complex was studied, and an X-ray crystal structure showed that netropsin formed a 1:1 complex with a 4-base pair TTAA sequence. The NH's of the amide linkages point towards the minor groove floor and makes specific hydrogen bonds with the A-T and T-A base pairs. (Dickerson, 1985). It was reasoned that it may be possible to change the recognition from AT to GC by adding an imidazole, which would be able to accommodate the exocyclic NH_2 of G,C base pairs.

1.3.2 Sequence Specific Polyamides

The 2:1 distamycin-DNA complex inspired the Dervan group to develop a sequence recognition code for these polyamides. (Dervan, 2001). The distamycin motif contains three consecutive N-methyl pyrrole (PyPyPy) groups and can bind A,T sequences as antiparallel 2:1 and 1:1 complexes. A polyamide, developed in the Dervan lab, containing an imidazole and two pyrroles (ImPyPy) was shown to bind in a 2:1 antiparallel fashion to 5'-(WGWCW)-3' where W is either A or T. The key is that the G and C positions were consistent, and it was suggested that the addition of an Im/Py pairing could change the recognition from an A-T pair to a G-C pair.

The Dervan group then began to construct hairpin polyamides utilizing γ-aminobutyric acid linkers to connect two antiparallel peptides that bind to the minor

groove, and were able to develop a recognition code based on the Py and Im motifs (White 1997). An Im-Py paring could recognize G-C, while a C-G was recognized by Py-Im. Py-Py was shown to bind either A-T or T-A. By replacing pyrrole with hydroxypyrrole (Hp), differentiation between A-T and T-A pairs became possible; the hydroxyl group would sterically clash with the edge of adenosine but had a favorable hydrogen bonding interaction with the carbonyl O of thymine. The design of this "four base pair code" (Figure 1.2) led to increased binding affinities (K_D ~10^{-9}M). An extended sequence of 16 base pairs was also recognized by linking additional Py/Im units but initially resulted in reduced affinity due to mismatches in the curvature of the DNA minor groove and the ligands. By introducing flexible β-alanine residues, the recognition of the sequence 5'-ATAAGCAGCTGCTTT-3' was achieved with a $K_D \sim$ 30 pM.

Some of these polyamides were shown to regulate gene expression, the ultimate goal of most small molecules that bind DNA. A polyamide was shown to reduce the level of 5S RNA produced by binding to the sequence d(AGTACT)$_2$ which is the site for a TFIIIA transcription factor. By binding to this sequence at a higher affinity than the TFIIIA enzyme, it was possible to reduce the amounts of 5S RNA transcribed (Gottesfeld 1997). In another study, the HIV-I enhancer/promoter regions, which contained multiple binding sites for several transcription factors, was selected as a target, and designed polyamides were shown to bind the appropriate target sequences. These ligands were able to inhibit viral transcription and were effective at inhibiting viral replication with minimal cell toxicity (Dickinson 1998).
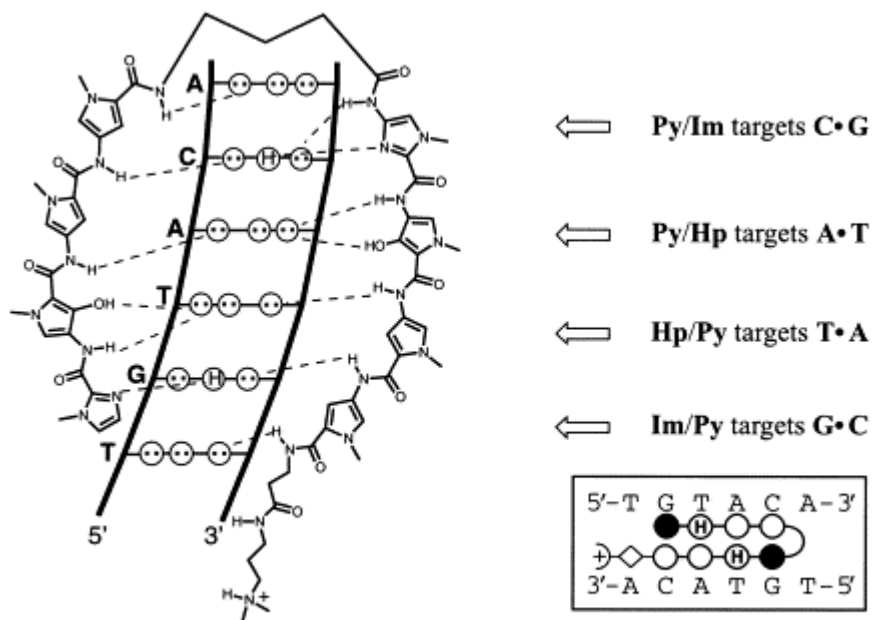
Figure 1.2 Binding model for the complex formed between ImHpPyPy-γ-ImHpPyPy-β-
Dp and a 5'-TGTACA-3' sequence that allowed for the establishment of a
four base pair code. Reprinted from *Bioorg. & Med. Chem,* 9, Molecular
Recognition of DNA by Small Molecules, Dervan, P. B., 2215-2235,
Copyright 2001, with permission from Elsevier.

1.3.3 DNA Intercalators

DNA intercalators contain an extended planar heteroaromatic ring system that
allows for its insertion between DNA base pairs. A common characteristic of these
heteroaromatic rings is that they have an electron-deficient portion that allows for
favorable electrostatic complementarity with relatively electron-rich DNA base pairs.
Intercalation leads to the extension of the DNA double helix by approximately 3.4 Å per
moiety since the DNA base pairs must vertically separate to incorporate the intercalating

7

chromophore. There is also local unwinding of the helix at the intercalation site along with distortions to the sugar-phosphate backbone. The distortion at the intercalation site prevents another moiety from intercalating at the adjacent site; an idea referred to as the neighbor exclusion principle (Crothers, 1968). The structural distortions also lead to changes in the hydrodynamic properties of DNA. These changes can be monitored by viscosity and gel electrophoresis mobility.

There are various types of DNA intercalators (Figure 1.3) that differ in the number of intercalating moieties as well as which grooves, if any, are occupied by substituents attached to the main chromophore. Ethidium bromide is one of the simplest know DNA intercalators that non-specifically bind DNA. It is often used as a means to visualize DNA bands in agarose or PAGE electrophoresis due to the fluorescent enhancement that occurs upon ethidium intercalating between the DNA base pairs. Actinomycin D is an example of a more complex intercalator that binds to DNA by intercalating its phenoxazone chromophore but also contains a peptide which occupies the minor groove (Waring 1970)

The inclusion of two intercalating moieties has led to design of bis-intercalators that have the potential to increase affinity as well as lead to new sequence specificities. Since monointercalators can only bind a dinucleotide step, there are only 10 possible sequences. However, the addition of two intercalating moieties that cover 4 base pairs could lead to 136 possible binding sites, and expansion to 6 base pairs leads to 2080 possible binding sites. Several bisintercalators, including ditercalinium, luzopeptin, and bis-daunorubicin, have been developed. Ditercalinium consists of two chromophores connected by a rigid diethylbipiperidine chain. Although it has a high binding affinity ($>10^{-7}$ M), it binds without much specificity with only some preference for binding GC-rich regions over AT-rich tracts (Mendoza 1990). Luzopeptins are antibiotics that

contain a decadepsipeptide that links together two quinoline chromophores and have a preference to bind AT-rich sequences (Huang 1983). They are structurally similar to echinomycin but bind with at least an order of magnitude higher affinity (Fox 1990).

Naphthalene diimide (NDI) and nogalamycin are examples of threading intercalators, the characteristic feature of which is that substituent's are able to simultaneously occupy both DNA grooves. NDI had been initially studied by Wilson *et al* (Wilson 1991). He used various alkyl amino substituents and spectroscopic and kinetic studies to determine that the positively charged substituents occupied both DNA grooves. The stopped flow kinetic experiments revealed that both the NDI association and dissociation rates are significantly slower than those of intercalators with similar binding constants and supported a threading mechanism. Nogalamycin is an antibiotic that contains an anthraquinone chromophore with two bulky sugar substituents. An X-ray crystal structure indicated that the bicyclo amino sugar occupies the minor groove and the nogalose sugar sits in the minor groove (Williams 1990).
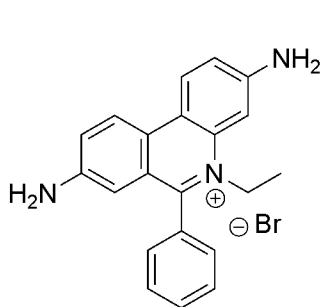
Ethidium Bromide
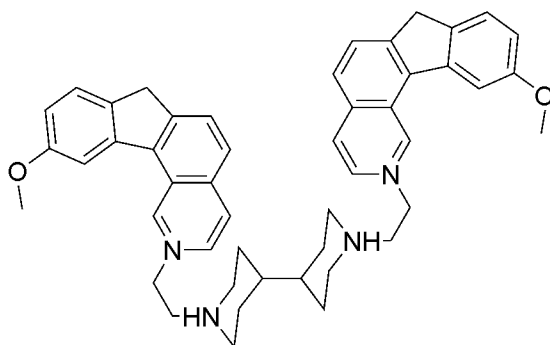
Ditercalinium
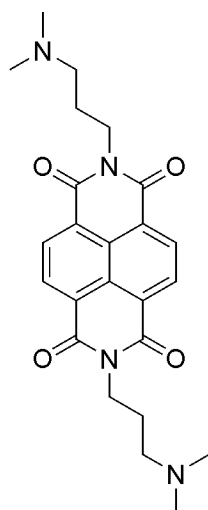
Napthalene bis(dicarboximide)
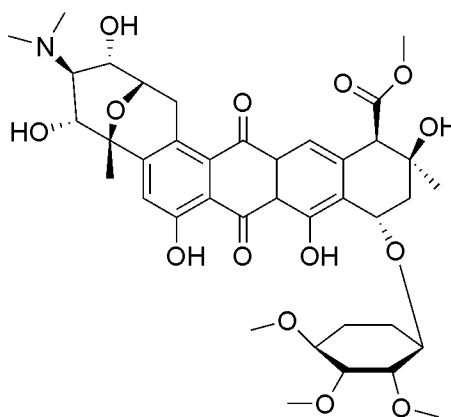
Nogalamycin

Figure 1.3. Structures of DNA intercalators.

1.4 INTERCALATORS DEVELOPED IN THE IVERSON LABORATORY

1.4.1 Initial Development

The Iverson laboratory began investigating the ability of an electron-deficient Naphthalene diimide (NDI) unit and an electron-rich Dialkoxynaphthalene (DAN) unit to

10

fold and self-assemble in an aqueous environment (Figure 1.4). Lokey *et al*. utilized this NDI moiety to develop a new set of polyintercalating molecules that were connected in a head-to-tail fashion using flexible peptide linkers. DNase I footprinting and UV-Vis based kinetic studies revealed that these molecules had a preference for poly(dGdC) over poly(dAdT). Viscometric titration and unwinding studies supported a full intercalation mode. Estimated dissociation constants (K_D) for the mono, bis-, tetra-, and octa-intercalators were 5×10^{-6} M, 2.5×10^{-7} M, 1.25×10^{-7} M, and 1.56×10^{-8} M, respectively.

Napthalenediimide (NDI)   **Dialkoxynapthalene (DAN)**
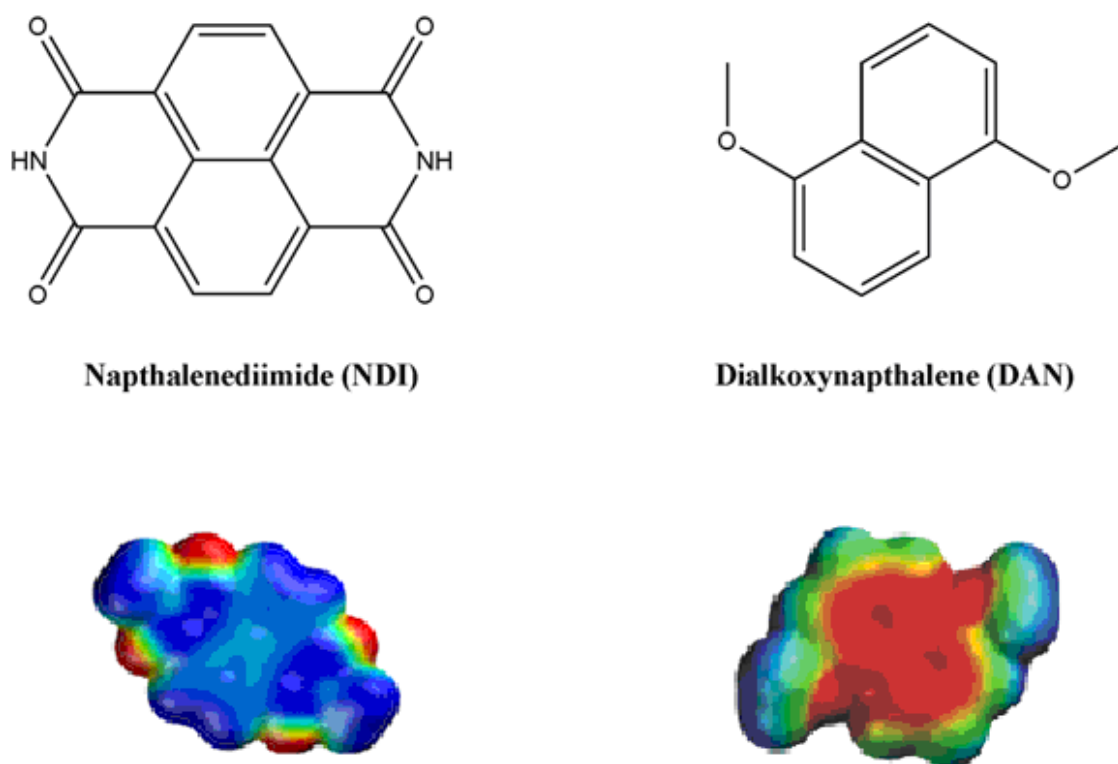
Figure 1.4. Structures and electrostatic potential maps of the NDI and DAN complexes. Blue represents areas of electron deficiency and red represents electron rich areas.

1.4.2 Bis-Intercalators

Based on these previous studies, the effect of the peptide linker between NDI units was examined to determine whether the peptide linker could alter sequence specificity. A combinatorial library of peptide linkers connecting two NDI units was developed and examined against a 231 bp restriction fragment of pBR 322 plasmid (Guelev 2000). A cleavage enhancement band observed in the footprinting results led to the identification of novel specificity for the bis-intercalator containing a β-Alanine based peptide linker that preferentially bound a non GC-rich sequence. This was significant because this molecule showed a change in sequence specificity from the initial molecules that had a preference for GC-rich sequences.

DNAseI footprinting led to the identification of two distinct compounds which exhibited significantly different binding properties (Figures 1.5 and 1.6). A bis-intercalator containing the *tris*-glycine-lysine linker (G_3K) showed a preference for the sequence d(CG│GTAC│CG)$_2$ (Guelev 2001). NMR structural studies confirmed that a 1:1 complex was formed with the NDI units intercalated between GpG steps and the peptide linker residing within the major groove. The compound containing the *tris*-β-alanine-lysine (β-Ala$_3$K) linker was shown to bind the sequence d(CGATAAGC)·d(GCTTATCG) as a 1:1 complex. The NMR structural studies again confirmed that the NDI units intercalate at the ApG and GpA steps. The key difference is that the peptide linker resides in the minor groove. These bis-intercalators bind two different DNA sequences with different groove preferences once bound. The G_3K peptide linker is 3 methylene units shorter than and not as flexible as the β-Ala$_3$K peptide linker. This difference could explain why the β-alanine linker resides in the longer and narrower minor groove.

X Y Z =

G₃K binds to 5'-GGTACC-3'

(beta-A)₃K binds to 5'-GATAAG-3'
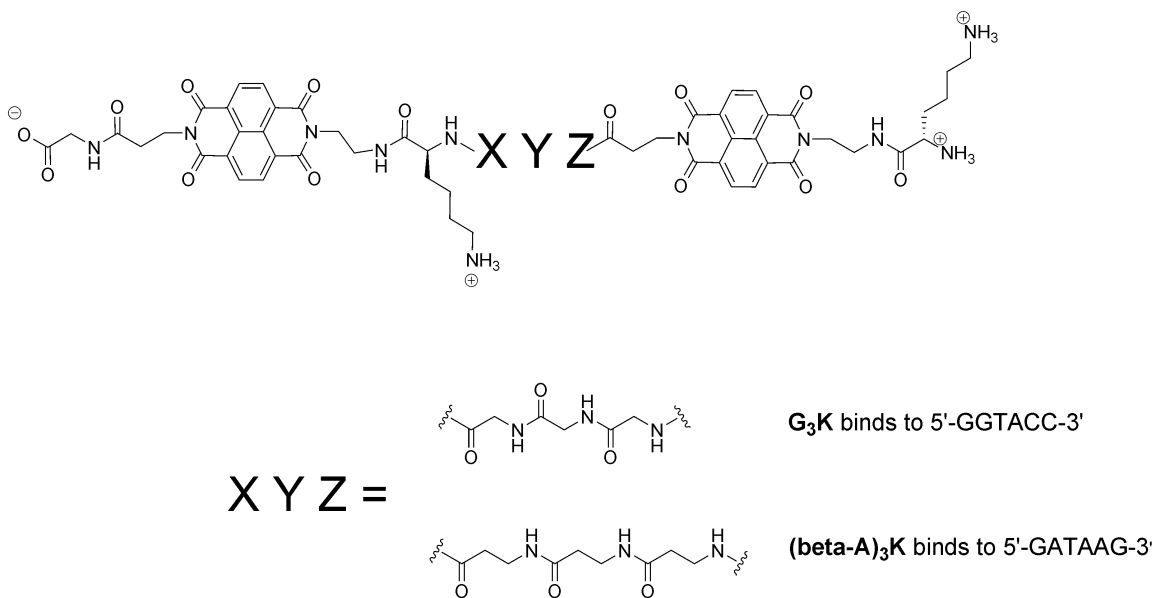
Figure 1.5. Structures of the major-groove and minor-groove-binding intercalators. The G₃K peptide linker resides in the major groove, while the β-Ala₃K peptide linker resides in the minor groove.
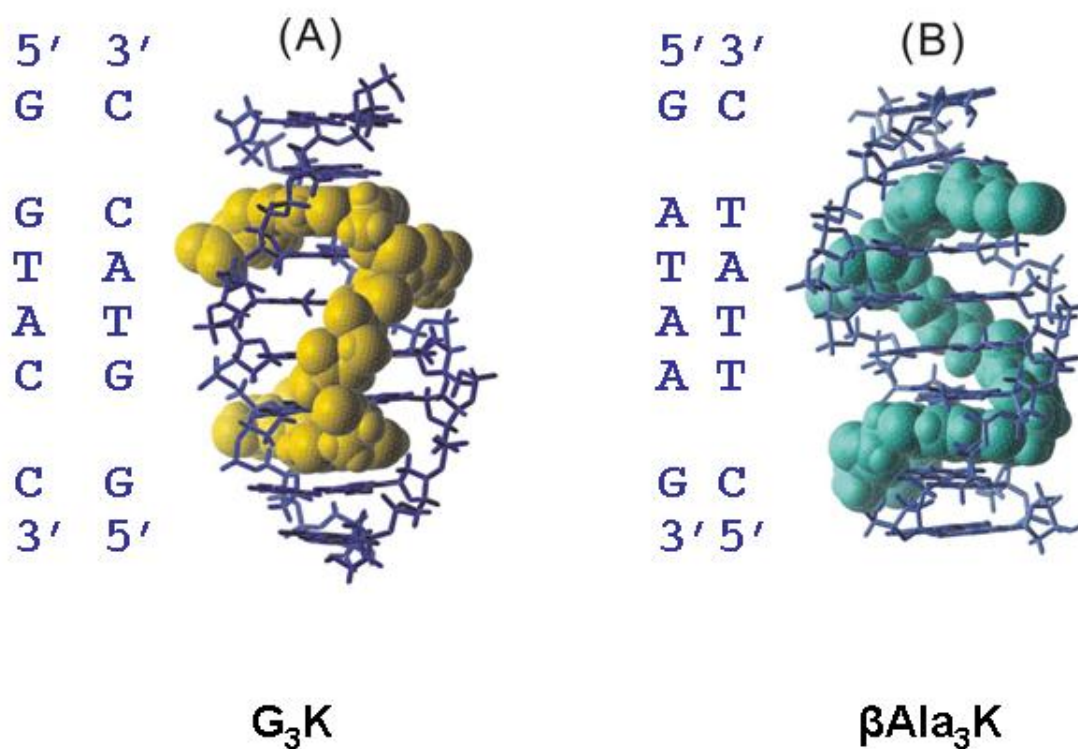
Figure 1.6. Space-filling models of the intercalator-DNA complexes, showing the occupation of the major and minor grooves by G_3K and βAla_3K, respectively.

1.4.3 Threading Tetraintercalator

The development of these NDI-based bis-intercalators verified that both the major and minor grooves of DNA could be targeted through threading intercalation. The development of a novel threading polyintercalator, in which both grooves could be targeted simultaneously, was based on the structural studies of the bis-intercalators. An adipic acid linker was chose to replace the G_3K linker because it greatly facilitated synthesis of the tetramer on the solid phase resin. Computer modeling indicated that the adipic acid would maintain the properties of the G_3K with regard to linker length and certain hydrogen bonding contacts. Four NDI units were linked in an alternating fashion

14

using the beta-alanine peptide linker followed by the adipic acid which acted as a cross linker between the two bis-intercalators (Lee 2004).

NMR structural studies confirmed that this novel tetraintercalator bound the sequence d(GATAAGTACTTATC)$_2$ with 1:1 stoichiometry (Figures 7 and 8). These NMR studies were simplified because the adipic acid linker provided C2 symmetry for the tetraintercalator, and the appropriate 14-base pair DNA binding site was palindromic. The resulting tetraintercalator-DNA complex was thus C2-symmetric, requiring that only half of the NMR signals be identified. This landmark study showed that the peptide linkers occupied the grooves in a threading pattern as predicted with the beta-alanine linker residing in the minor groove, followed by the adipic acid in the major groove, and again the beta-alanine linker in the minor groove. This was the first structurally characterized threading polyintercalator and it verified that the sequence-specific binding of longer threading polyintercalators could be predicted from bis-intercalator modules.
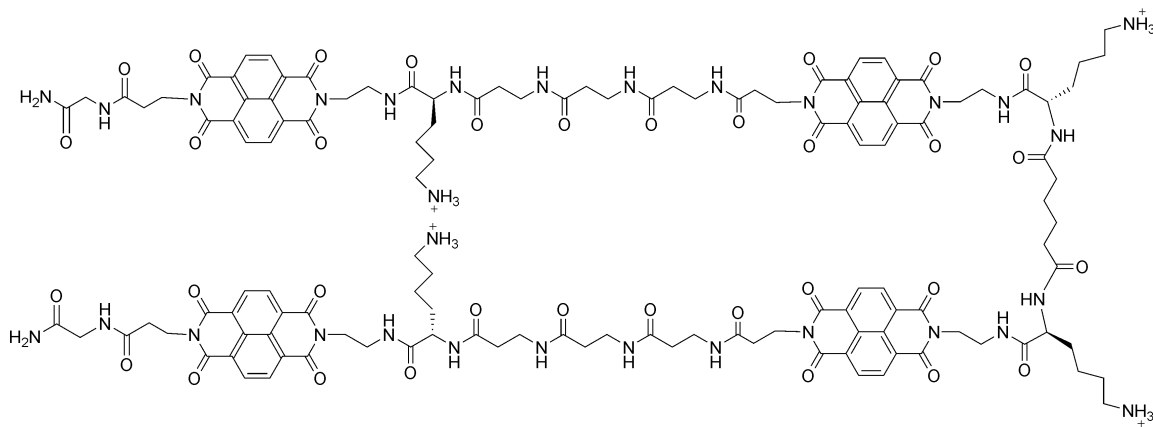
Figure 1.7. Structure of the tetraintercalator

15
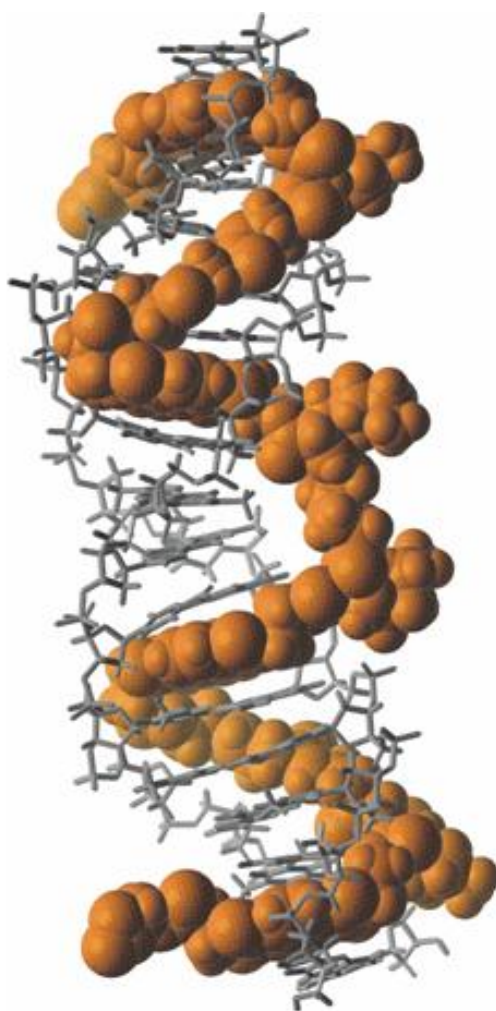
5'-G|ATAA|GTAC|TTAT|C-3'
3'-C|TATT|CATG|AATA|G-5'

Figure 1.8. A spacefilling model of the tetraintercalator-DNA complex. This landmark structural characterization of the threading polyintercalation mode of binding verified that the linkers occupied the minor, major, and minor grooves in an alternating fashion. Reprinted with permission, from the Journal of the American Chemical Society, Copyright 2004, and American Chemical Society.

1.4.4 Cyclic Bis-Intercalator

Based on the previously discussed bis-intercalators, a novel structurally characterized cyclic bis-intercalator was developed and structurally characterized. Two NDI units were incorporated to contain both the tri-gylcine and tri-beta-alanine peptide linkers (Figure 1.9). DNaseI footprinting showed that this cyclic molecule preferentially bound to 5'-GGTACC-3' with a K_D of approximately 10^{-7} M. Interestingly, the cyclic molecule did not exhibit binding to the 5'-GATAAG-3' sequence for the β-Ala$_3$K bis-intercalator, suggesting that the glycine peptide linker drives the specificity of the cyclic molecule. NMR structural data verified that the NDI units intercalated between the GpG steps with the G$_3$K linker resided in the major groove and the β-Ala$_3$K linker in the minor groove. This is the first structurally characterized pseudocatenane complex between a sequence-specific cyclic bis-intercalator and DNA (Chu 2009).

A cyclic structure provides unique opportunities for developing novel DNA intercalators. The complex is interesting for various reasons The imino protons between base pairs have exchange half-lives that are typically in the 1-50 ms range. It is possible that a cyclic bis-intercalator may be able to exploit this DNA breathing to form a pseudocatenane-like complex with DNA. It is also reasonable to assume that such a complex would have extremely slow dissociation kinetics, owing to the fact that significant DNA distortion is likely required for the release of a bound cyclic intercalator. Additionally, the cyclic intercalator has the ability to occupy simultaneously both DNA grooves of the same sequence.
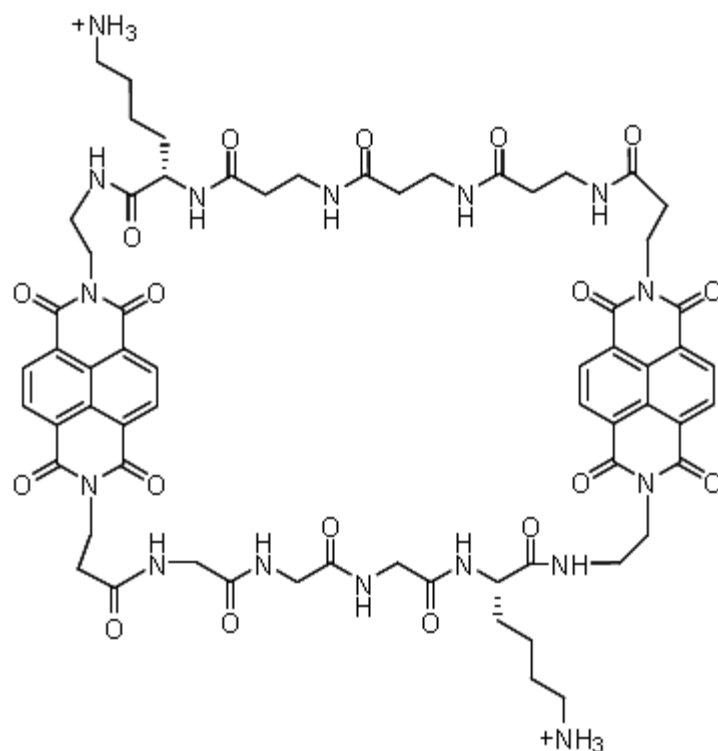
Figure 1.9 Structure of the cyclic *bis*-intercalator.

1.5 VISUALIZATION OF SMALL MOLECULES AND PROTEINS BINDING DNA

In order to undertake a detailed investigation of how a DNA binding molecule locates its binding site, translates along DNA, or alters DNA conformations, it is necessary to visualize individual DNA molecules. Atomic Force Microscopy (AFM) and Transmission Electron Microscopy (TEM) are the two most prevalent techniques for such a study and allow for the direct visualization of DNA binding complexes. What separates these techniques from other conventional biochemical techniques is that these studies allow for the direct visualization of a small molecule or large protein interacting with DNA. This offers a complementary technique to traditional biochemical analyses that provides a more complete picture of a DNA binding process.

18

1.5.1 Atomic Force Microscopy Principles

The basic components of an AFM include a laser, cantilever, photodiode detector, and a piezoelectric transducer (Figure 1.10). The cantilever contains a sharp tip at its free end that interacts with the sample surface and formulates an image representative of the sample surface being investigated. The intermittent-contact (tapping) mode is utilized for biological samples such as DNA.
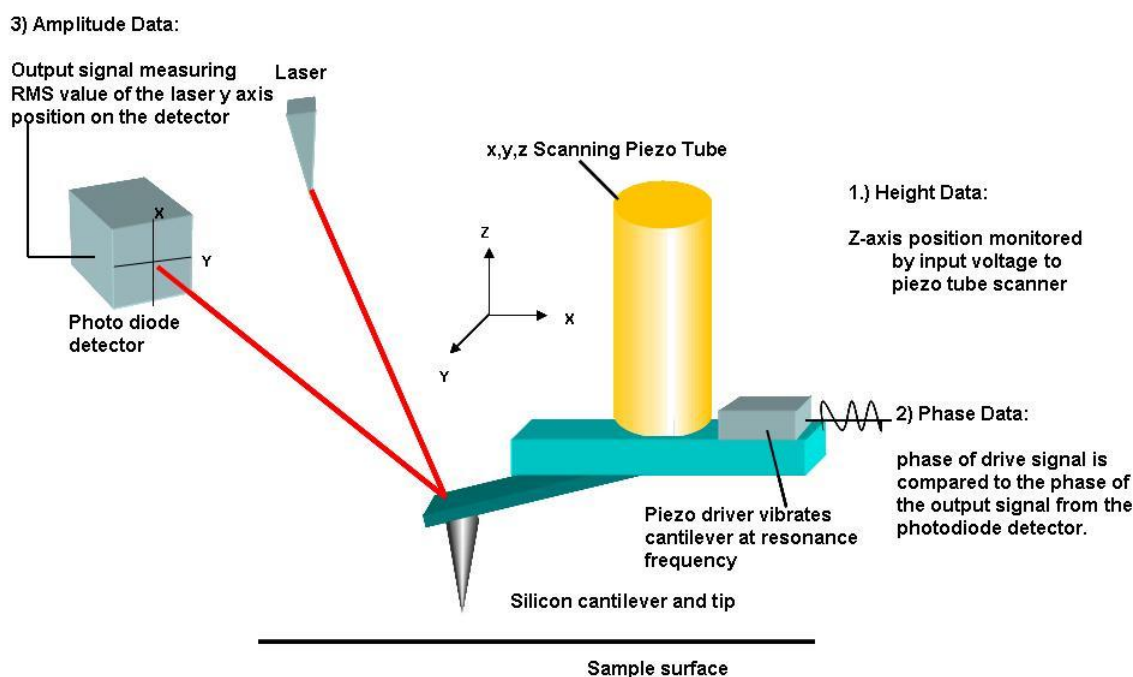
Figure 1.10. Diagram of the AFM cantilever and tip which can generate images from data in the x, y, and z axes.

The laser is first aligned with the cantilever and is then reflected off the cantilever and into the photodiode detector. As the cantilever bends, change in the position of the laser results in a deflection signal. This deflection signal can measure changes in the x and y direction, allowing for phase and amplitude images. Images reported here, however, are topographic images that depend on changes in the z-axis. This is dictated in part by the piezoelectric transducer. This transducer uses a feedback loop that maintains

the oscillation of the tip at its characteristic resonance frequency. This frequency is automatically tuned prior to interacting with the sample surface. When the tip approaches the surface, different forces such as electrostatic interactions, van der Waals forces, and dipole-dipole interactions act on the tip and change the oscillation of the cantilever resulting in deviations from the resonant frequency. These deviations allow one to obtain a topographical image of the sample surface.

For DNA samples, a mica surface is generally chosen, as a freshly cleaved surface is anatomically flat. Even the smallest deviations in topography can be detected on mica making it an optimal surface to image DNA. When cleaved, however, the mica surface will have a negatively charge at a neutral pH due to the presence of siloxy groups. Therefore, it is necessary to provide a positive charge on the surface that can electrostatically bind DNA via its negatively-charged phosphate backbone.

1.5.2 DNA Based Studies in the AFM

The information that can be obtained by directly visualizing a certain interaction is a powerful reason why the AFM is used to study DNA-small molecule interactions. The two most common types of studies involve investigating DNA-protein interactions and assessing structural effects of DNA upon intercalation. These studies can confirm information that is derived from conventional solution-based techniques and also offers unique experimental images that can't be obtained in any other manner.

DNA-protein complexes have been studied extensively (Kaguni 2006), including transcriptional factors (Cases 2005), and investigations into structural changes (Bates 2005). For example, RecA protein plays an integral role in genetic recombination, in which two homologous DNA molecules pair and exchange regions of their DNA strands. One of the steps in this process is the competitive binding that occurs with the single stranded DNA-binding protein (SSB) (Meyer 1990). SSB binds to ssDNA and removes

the inhibitory secondary structure that would otherwise block the binding of RecA (Reddy 2000) but it is also competitive, since RecA must also displace the SSB protein (Morrical 1986). A study was undertaken by Goh *et al.* to examine directly the structural effects of the protein complexes with and without the ATPγS cofactor to assess the competitive binding between SSB and RecA. The images obtained were able to definitively show that RecA has a higher affinity for ssDNA than SSB only when ATPγS is present, which confirmed previous fluorescence measurements. Furthermore, the direct visualization of the structures showed that the RecA protein can overwhelm the SSB protein to elongate the DNA and formed extended structures that are required to interact with dsDNA.

The intercalator-based AFM studies have generally been concerned with assessing DNA morphology due to its interactions with various intercalators. Examples of intercalators studied include ditercalinium (Berge 2002), echinomycin (Tseng 2005), and nogalamycin (Banerjee 2008). The investigations into echinomycin binding to DNA confirmed the elongation and unwinding of the DNA helix that had been previously deduced from X-Ray and NMR studies. The most substantial result showed a clear change in plasmid structure that was quantitatively analyzed to reveal supercoiling transitions at varying concentrations of intercalator (Figure 1.11). This was one of the first studies that directly visualized the structural changes of DNA induced by DNA intercalation. The ditercalinium investigations using small 292 bp fragments of DNA also showed measured increases in contour length corresponding to the intercalator binding at every other available binding site. The AFM studies also provided direct evidence that the DNA was increasing in its rigidity with increasing concentrations of intercalator (Figure 1.12).

Most recently, an investigation into nogalamycin binding plasmid DNA was undertaken by Banarjee. Nogalamycin had been previously studied binding to a small DNA fragment using X-ray crystallography and NMR.   However, this report provided the first opportunity to visualize directly nogalamycin's effects on a longer stretch of DNA. It was shown that at increased incubation times, the plasmid DNA began to transition from a circular supercoiled structure to a tight plectonemic superhelix. UV-Vis and CD experiments were carried out in parallel and confirmed these structural changes. This type of investigation was integral in defining nogalymycin's ability to act as a DNA intercalator on longer strands of DNA (4631 bp) and built upon initial structural investigations of nogalamycin on a much smaller DNA hexamer.
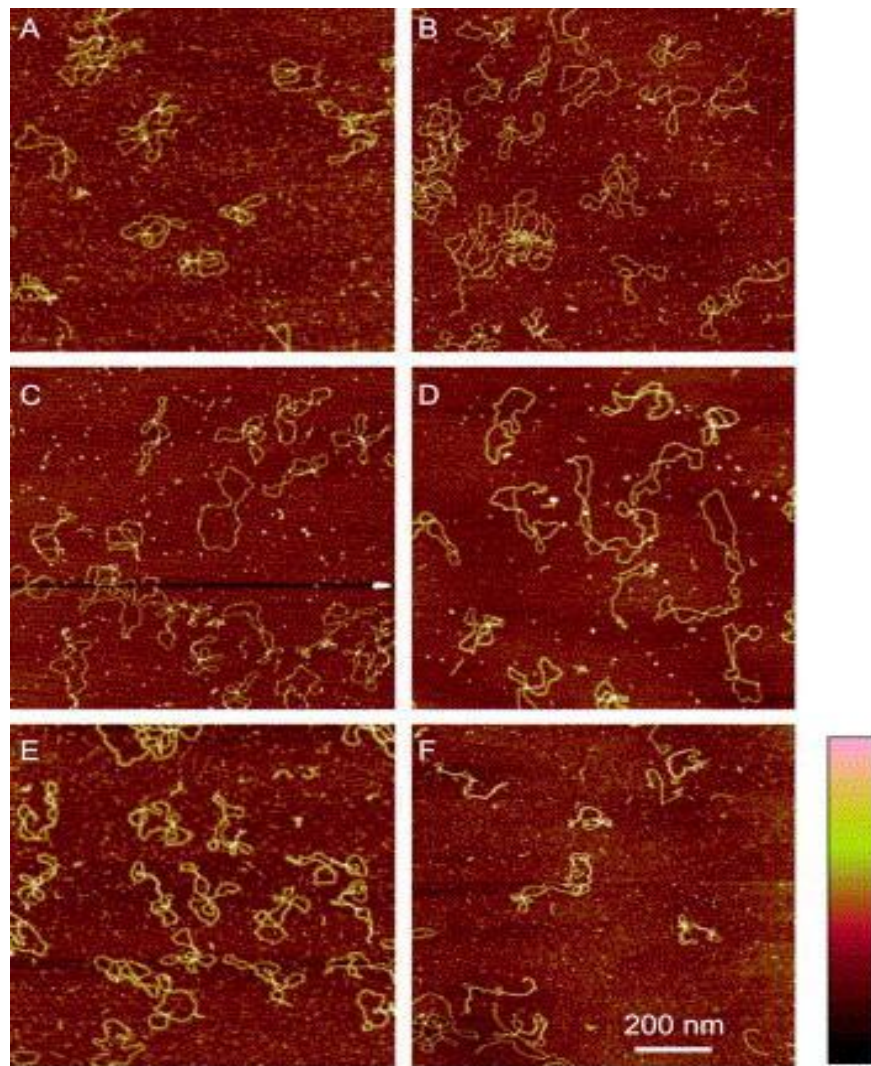
Figure 1.11. Plasmid structure of echinomycin changing as the concentrations of echinomycin was altered. (A) DNA alone, (B) 50 nM, (C) 250 nM, (D) 500 nM, (E) 5 uM. (F) 50 uM echinomycin. The height scale bar on the right is from 0 to 2.5 nM. Reprinted from *J. Mol. Biol.,* 345, Atomic Force Microscopy study of the structural effects induced by echinomycin binding to DNA, Tseng Y. D., 745-758, Copyright 2005, with permission from Elsevier
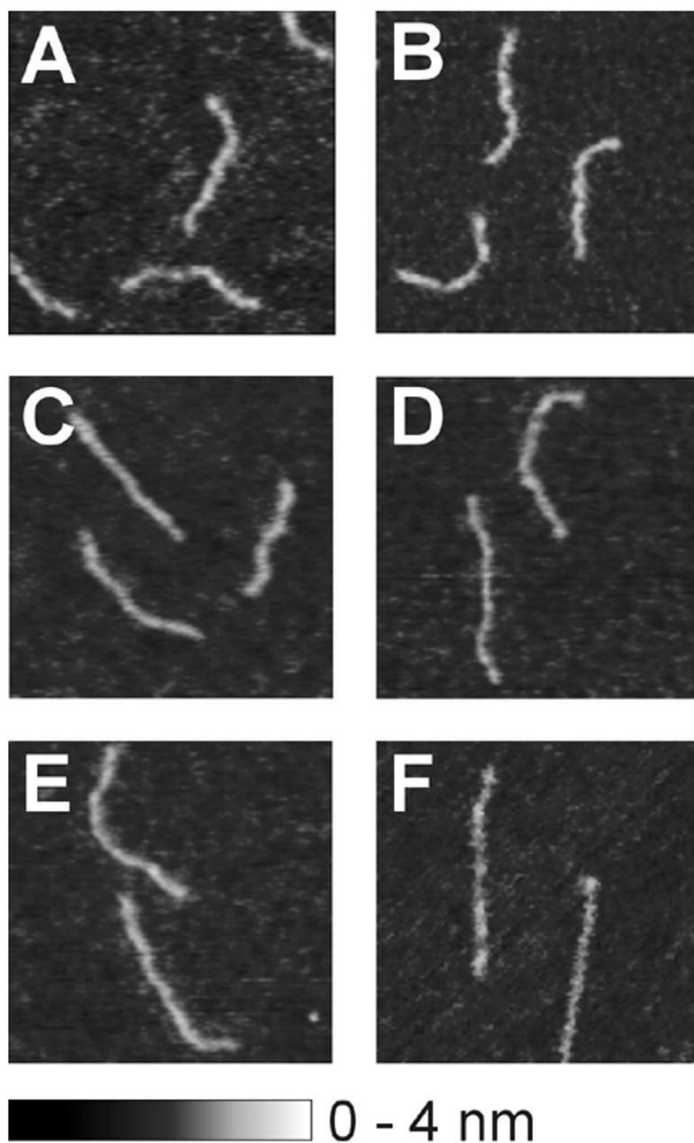
Figure 1.12. AFM images showing the effect of ditercalinium binding to 292 bp DNA fragments. Bis-intercalation of ditercalinium into DNA causes an evident lengthening and increased rigidity. The molar ratios are 5,10,25,35, and 50 to 1 in A, B, C, D, E, and F respectively. Reprinted from *Nucleic Acids Research,* 30, Structural perturbations in DNA caused by bis-intercalation of ditercalinium visualized by atomic force microscopy, Berge, T., 2980-2986, Copyright 2002, with permission from Oxford University Press.

1.5.3 Transmission Electron Microscopy Principles

The electron microscope (EM) is a complex apparatus that relies on the interaction of electrons with a sample surface; these interactions allow for image formation. At the top of the microscope is an electron gun that generates an electron beam. Two of the most common types of electron guns are based on the principles of thermionic emission: a tungsten filament cathode and a Lanthanum Hexaboride (LaB$_6$) based cathode. Energy, in the form of heat, is provided to the metal surface. When sufficient energy is provided, some electrons will overcome the work function of the metal. An anode present will help to accelerate these electrons as they are repelled from the cathode and move towards the anode. This process helps to determine the accelerating voltages that vary from different microscopes (40 eV to 200 eV).

Once a beam of electrons is formed, a series of electromagnetic lenses and electrostatic coils help guide the electron beam through the microscope. The lenses cause a magnetic field that allows one to direct the movement of the electrons, while the electrostatic coils can help shift the beam by coupling two deflections in opposing directions. There are also sets of apertures in front of each set of lenses that block out any electrons not directly in the center of the microscope. This is important because the electromagnetic lenses require that the electron beam passes through the exact center of the lens to avoid astigmatism (circular irregularity).
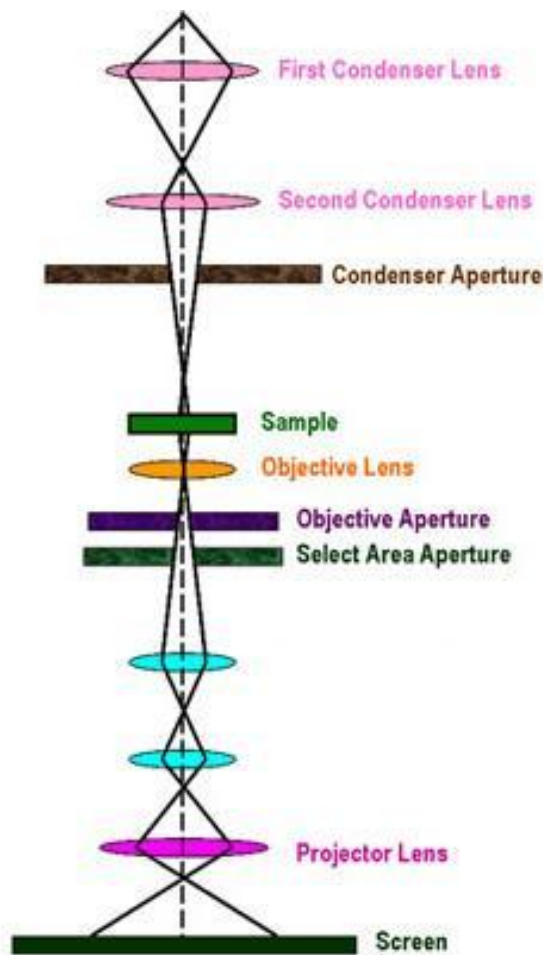
Figure 1.13 Simple diagram of the lens system in the electron microscope.

     The first set of lenses are the condenser lenses that take the electrons as they flow from the electron gun and focus them into a concentrated beam. This system usually consists of two lenses that can be used to control the spot size of the beam and the beam intensity. After this, the electrons pass through the specimen and the objective lens systems helps to focus the electron beams that pass through the sample. These beams then move through a series of lenses that help to magnify the beam onto a phosphor

26

screen. This screen is usually coupled to a CCD camera, allowing for the visualization of an image.

The most important principle for image formation relies on what happens to the electrons when they pass through the sample. Figure 1.14 summarizes the common interactions that occur between the electron beam and sample. For traditional TEM, the density of the material present determines the image that is formed. The sample surface is generally a carbon coated grid. Since carbon is not a very dense atom, it allows for most of the electrons to transmit through it with very little scattering. This results in most of the electrons passing through the sample. When more dense materials, such as atoms of higher atomic number or proteins with significant density are present, electrons are scattered or deflected and do not pass through the objective lens. This allows for the formation of an image as these denser materials will appear as dark objects against the brighter carbon film background since the electrons were not transmitted through that part of the sample surface. It is also possible to using a scanning beam (STEM) that utilizes the scattered electrons to formulate an image. The beam is focused onto the sample (the condenser lens is bypassed) and scans the sample surface. The backscattered electrons are detected by a high angle diffraction detector and this sometimes allows for better resolution for smaller samples. These types of images result in a dark background and sample features will appear as white objects since they deflect the electrons and this is what is measured.

For biological samples such as DNA, it is necessary to add a contrast agent. DNA is made of phosphorous, oxygen, nitrogen, and carbon, of which all have very little scattering power. By adding a contrast agent such as uranyl acetate, one is able to indirectly visualize the DNA. The dense uranium atoms will scatter the electrons

significantly more than the immediate carbon film surrounding the DNA molecule and the individual DNA molecules can be visualized in the microscope by reverse contrast.

Incident
high-kV beam

Secondary
electrons (SE)

Backscattered
electrons (BSE)

Characteristic
X-rays

Auger electrons

Specimen

Elastically
scattered
electrons

Direct
beam

Inelastically
scattered
electrons
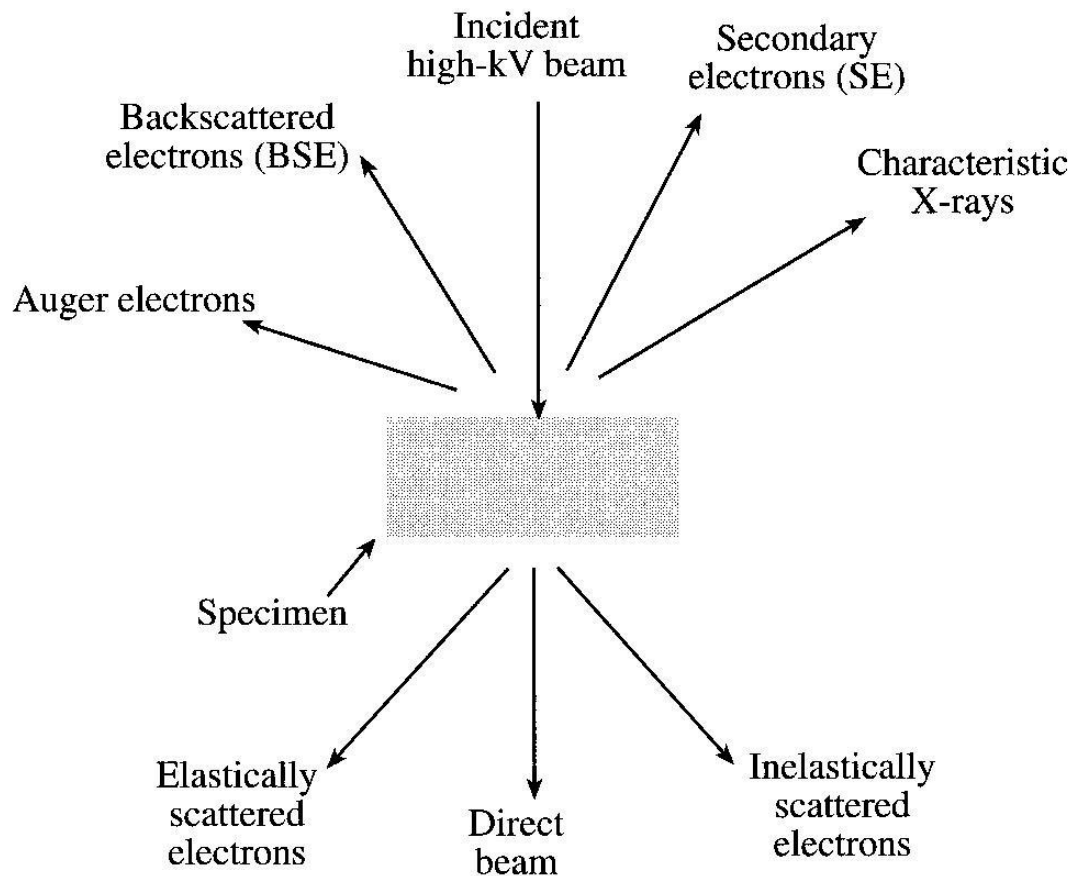
Figure 1.14. Various interactions occur when the electron beam interacts with the sample surface. The carbon grid does not significantly contribute to either electron scattering or backscattering. The elastically scattered electrons are primarily responsible for the formation of the image in the TEM mode, while the backscattered electrons are responsible for the formation of an image in the STEM mode.

1.5.4 DNA Based Studies in the TEM

An early study used electron microscopy to visualize directly the structural effects of the cAMP·cAMP receptor protein (CRP) complex binding DNA. At the time, circular

dichromism studies had determined that CRP complexes with short oligonucleotides induced conformational changes in the DNA (Crothers 1984) while electrophoretic studies confirmed that CRP binding significantly reduced the electrophoretic mobility of the CRP complexes with 100 to 300 base pair fragments of DNA (Kolb 1983). This led to the hypothesis that CRP induces DNA bending. In order to test that hypothesis, Clore *et al.* investigated the binding of CRP to both 2685 and 301 bp fragments of linear DNA. With the 301 bp fragment, it was shown that the protein kinked the DNA into V-shaped complexes. Close inspection of the micrographs revealed that the protein lies on top of the apex with the DNA bent away from the protein. The 2685 bp fragment showed similar effects and interestingly showed a decrease of non-specific binding when compared to the smaller fragment. The 301 bp fragment had a higher population of DNA, molecules with the protein bound at the ends of the DNA and significantly reduced with the larger fragments. This was the first direct evidence of the structural effects that CRP had upon DNA binding, which confirmed previously hypothesized results based on more conventional biochemical analytic techniques.

The binding of p53 to Holliday junctions was directly visualized and complemented by gel shift assays to determine the degree of specificity that p53 exhibited for these junctions (Griffith 1997). The gel shift assays were used to verify that p53 was binding to the four and three arm junctions and the electron microscopy was used to determine the exact positioning of the p53 protein. Based on statistical analysis of individual DNA molecules, 61% of the Holliday junctions contained a p53 protein and of those, over 80% of the p53 was located specifically at the junction, indicating a high degree of specificity of the p53 protein for those junctions. It was also possible to use the electron micrographs to determine the exact structural characteristics of the DNA junctions with regard to the junction angles of the tetrameric DNA species.
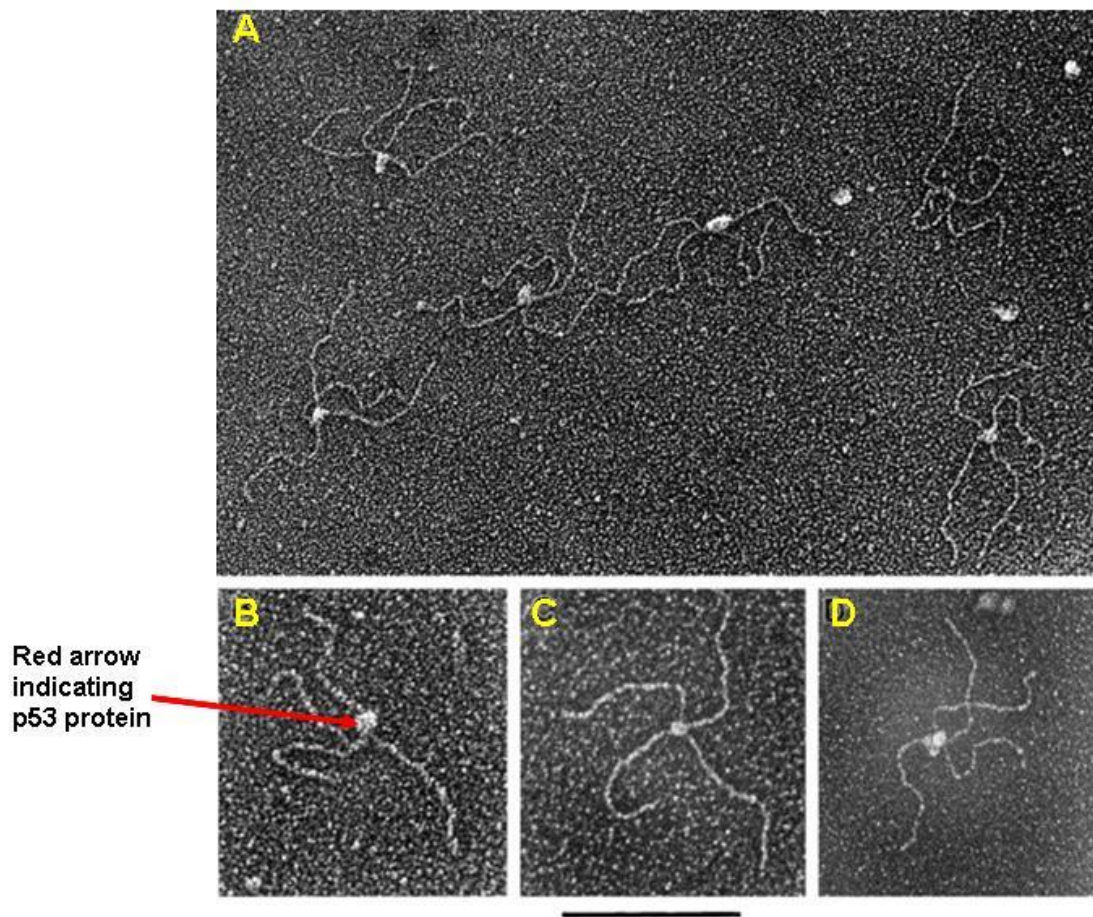
Figure 1.15. Electron micrographs showing the direct visualization of human p53 bound to Holliday junction DNAs. The scale bar equals 0.6 um (A) and 0.05 um (B-D). Reprinted from *The Journal of Biological Chemistry,* 272, Human p53 binds Holliday junctions strongly and facilitates their cleavage, Griffith, J., 7532-7539, Copyright 1997, with permission from The American Society of Biochemistry and Molecular Biology.

The interaction of Rec-A protein binding to DNA has been extensively studied by electron microscopy. One study in particular examined the effect DNA intercalation had upon the binding of RecA protein to dsDNA. When RecA protein was mixed with DNA in low salt buffers, it did not bind DNA. However, the addition of ethidium bromide in the exact same incubation conditions facilitated RecA binding to DNA. Intense microscopic studies were able to ascertain directly the structural effects that the

30

intercalator induced binding had on DNA with regard to helical pitch and intense coverage of the intercalators on the DNA. It was hypothesized that the coverage of the DNA by the intercalators created nucleation sites that greatly enhanced the ability of the RecA protein to bind to the dsDNA (Griffith 1990).

1.6 NANOGOLD PROBES

Gold clusters are gold compounds with a core of multiple gold atoms with the gold atoms at the surface covalently attached to organic groups. Undecagold, $Au_{11}(P(C_6H_5)_3)_7$, was one of the first gold clusters structurally characterized by X-ray diffraction (McPartlin 1969). Modifications of the ligand shell led to water-soluble analogs that are an integral requirement for analyzing biological systems (Bartlett 1978). A larger gold cluster was eventually developed that was larger in size (1.4nm, ~67 gold atoms) allowing for easier visibility (Hainfeld Nanogold Incorporated). Nanogold Incorporated® manufactures these small 1.4 nm gold nanoparticles® with various functionalities to allow for 1:1 site specific conjugation to a variety of functional groups and antibodies. The attractive features of these probes are their chemical stability, high contrast density, monodisperse size, and water solubility. They are more stable than colloidal gold particles, which generally rely on non-site-specific interactions to label biological molecules. These probes have been used extensively for various applications and a few examples will be highlighted.

An often utilized application of these nanoparticle probes is to use them as a means to detect the localization of particular proteins or peptides. By labeling the protein of interest with a gold nanoparticle, one is able to then asses the biological systems containing the labeled protein and directly visualizes its distribution. An early study investigating the use of gold nanoparticle probes exploited the biotin-avidin binding interaction. The smaller, undecagold cluster was modified to incorporate a biotin

derivative and was mixed with the avidin protein. The electron microscopy images obtained showed the presence of the gold nanoparticles onto the avidin only when functionalized with biotin. This study was significant as it showed these nanoparticles had the potential to be used as biological probes (Safer 1982).

Another study examined the binding of various peptides to sites in rat spinal cord tissue. After labeling four different peptides with the gold nanoparticles, they were run on PAGE gels to confirm that the nanoparticles were bound to the peptide and to confirm that the binding specificity was not altered. After incubation with the various tissues, the tissues were examined under the electron microscope. This study provided a clear depiction of the various localizations of the respective peptide receptors within the tissue (Heppelmann 1999).

Chapter 2: Progress towards the Development of a Method to Directly Visualize the Mechanism by which a Cyclic Bis-Intercalator Locates its Preferred Binding Sequence

2.1 GOAL AND PURPOSE

Covalent linkage of a gold nanoparticle probe to a sequence specific cyclic bis-intercalator (Chu 2007) (Figure 2.1) will allow for the indirect visualization of the intercalator binding to DNA and begin to further our understanding of how these complex intercalators can locate their preferred binding site along a large sequence of DNA. This is important in helping to gain a deeper understanding of binding kinetics. If the binding site located mechanism favorably translates to locating preferred sequences in cellular DNA, these intercalators may be candidates for *in vivo* studies.
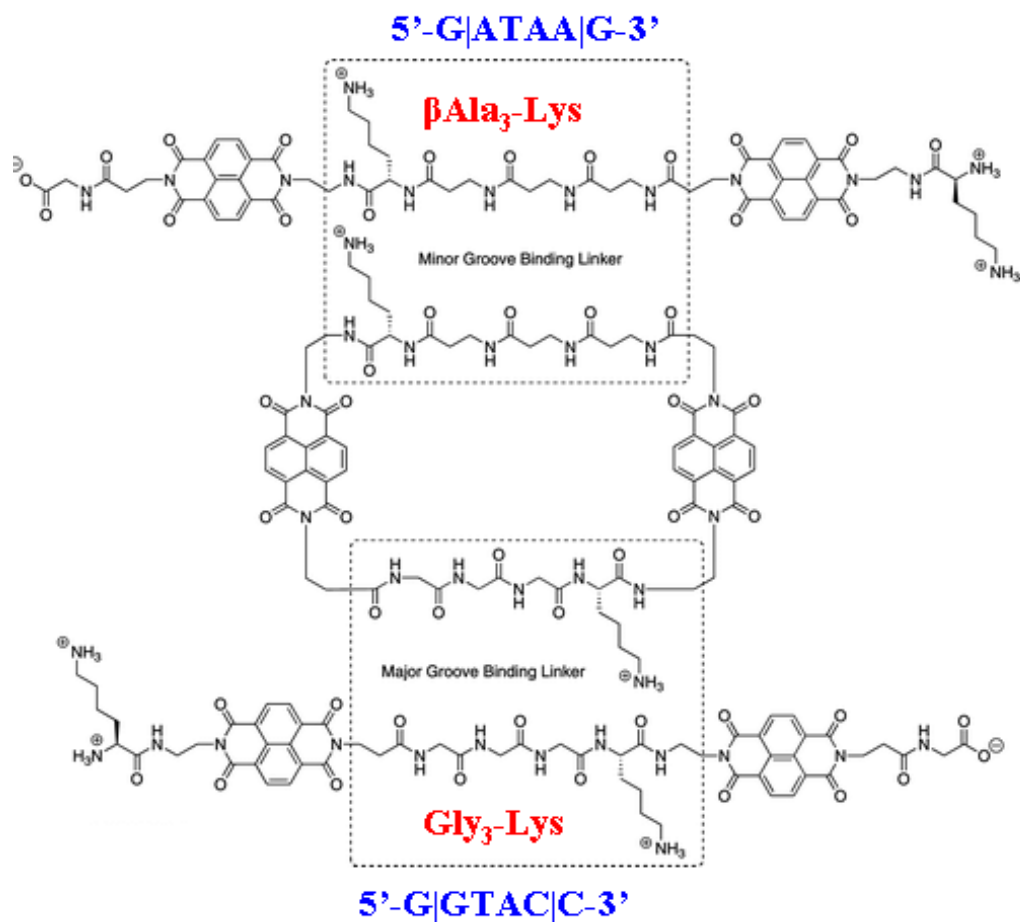
Figure 2.1. Structure of the cyclic *bis*-intercalator. (Center) with the linker components of both previously characterized *bis*-intercalators. The cyclic *bis*-intercalator showed a strong specificity for the G_3K sequence, 5'-GGTACC-3'.

2.2 INTRODUCTION

The biotin-streptavidin interaction is one of the strongest interactions in biological systems, with a dissociation constant of about 10^{-15}M (Green 1975). This strong interaction is the aspiration for developing synthetic systems that could potentially mimic this strong mode of binding. Our laboratory has developed a tetraintercalator which shows a strong binding interaction ($K_D \sim 10^{11}$ M) to a 14-base pair sequence of DNA.

Some initial investigations into how the tetraintercalator locates its binding site using DNAse I footprinting were undertaken (Garen Holman, Dissertation Univ. of Texas at Austin). Based on a model summarized in Figure 2.2, one could decipher whether or not the molecule randomly associates and dissociates from the DNA until its preferred sequence is located or whether it initially associates with DNA and then slides along the DNA until its preferred sequence is located. Most recently, investigations into its dissociation half-life have shown that the tetraintercalator binds with a remarkable estimated half-life of 16 days.

Actinomycin D has been intensively studied with regard to its sequence specificity and structural-binding characteristics. Fox and Waring studied its time dependent binding using DNAseI footprinting and proposed that the intercalator initially bound to DNA in a non-specific manner but quickly dissociated as the ligand moved along the DNA until the preferred sequence was located. This type of association-dissociation mechanism is widely accepted as a possible binding-site location mechanism for protein-DNA interactions and could certainly be carried over to threading polyintercalation. For association-dissociation, the molecule will randomly associate with the DNA and if it is not the correct site, it will completely dissociate and then randomly re-associate at another site until, the preferred sequence is located. Another proposed mechanism occurs when an initial binding event, likely at the ends of the DNA, leads to the molecule sliding along the DNA, without completely dissociating, until the binding site is located. Finally, a less prevalent mechanism is termed intersegmental transfer, where the molecule may bind one site on DNA and cause a DNA bending event that would result in a transfer of the molecule to the new binding site. These mechanisms are summarized in Figure 2.3.
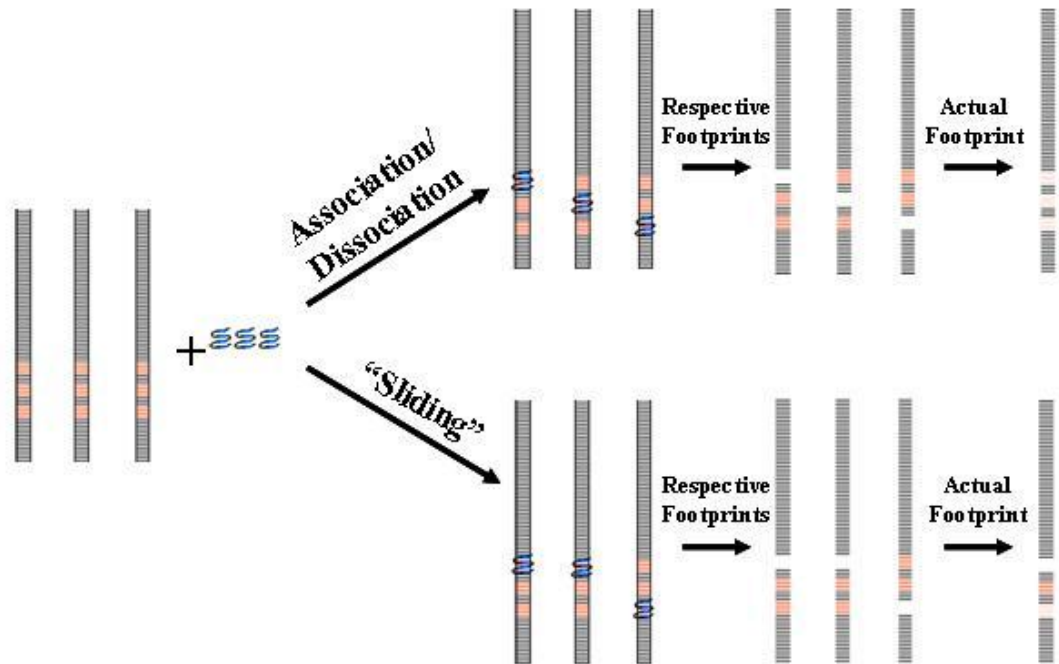
Figure 2.2. By placing three binding sites at one end of DNA, the footprint obtained should provide insight into the binding site location mechanism. A sliding mechanism would block the interior binding site from being significantly occupied, while similar occupation of all three binding sites would suggest an association-dissociation mechanism. This graphical representation was designed by Garen Holman.

Sliding

Association-Dissociation

Intersegmental Transfer
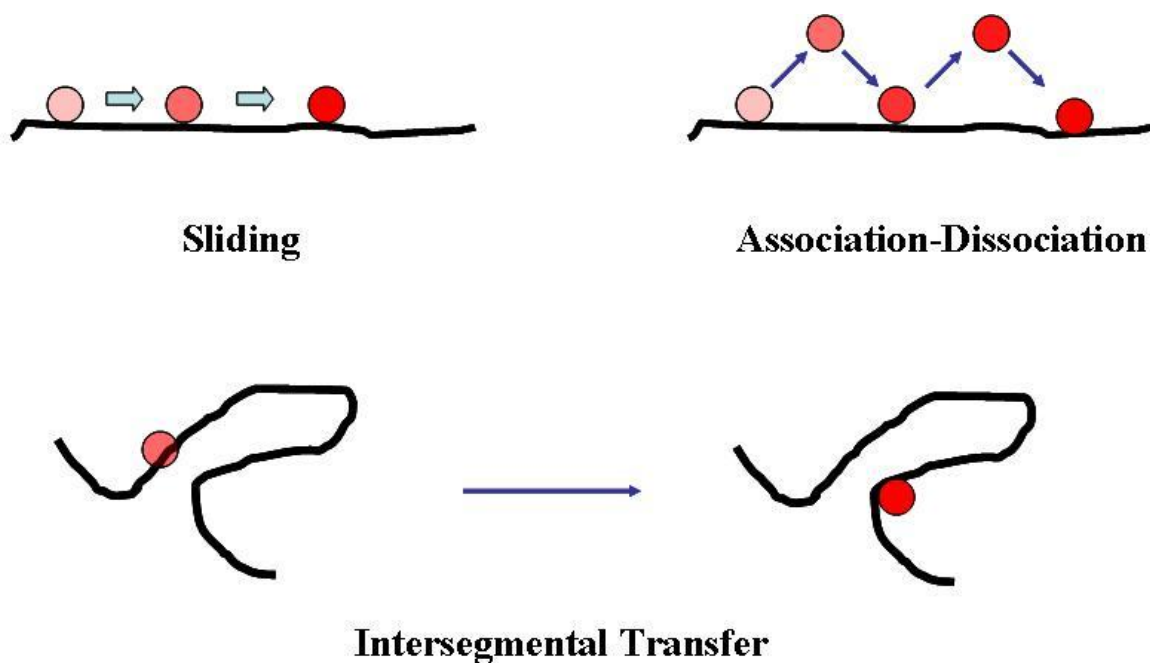
Figure 2.3. Simplistic models for binding site location.

Figure 2.4 shows a model of the cyclic *bis*-intercalator bound to its preferred sequence. One can imagine that significant DNA distortion is necessary to allow this intercalator to bind its preferred sequence. If one binding site is present within a long strand of DNA containing non-specific sequences, it is intriguing to think about how a DNA intercalator can locate that sequence. Based on the previous data for our tetraintercalator, the cyclic *bis*-intercalator may behave in a similar manner with regard to its strong binding (long dissociation half-life) in conjunction with the significant distortion of the DNA likely required for the cyclic *bis*-intercalator to bind to the 5'-GGTACC-3' sequence. While DNA footprinting allows one to gain a strong understanding of sequence-specificity, footprinting alone may not directly determine the mechanism by which an intercalator locates its binding site.

The sliding and association-dissociation mechanisms are the most likely possibilities for how the cyclic *bis*-intercalator would locate its preferred sequence. As the molecule intercalates, it would be expected that there would be significant structural distortions to the DNA with regard to local base pair opening. These distortions are not going to be energetically favorable due to the strain that would be introduced to the double helix. Therefore, one could imagine that this molecule should be highly selective for its preferred sequence. It would also be reasonable to expect slow dissociation kinetics once bound to the preferred sequence, which would make intercalation unlikely at non-specific sites due to its complex binding. This type of non-specific binding may not be detected using traditional DNAse I footprinting if it occurs at random sequences and with a minimal number of binding events. It is also possible that there is significant electrostatic binding due to the lysine side chains on the cyclic *bis*-intercalator. This is expected, but the extent to which it occurs may be ascertained through the direct visualization of the DNA.
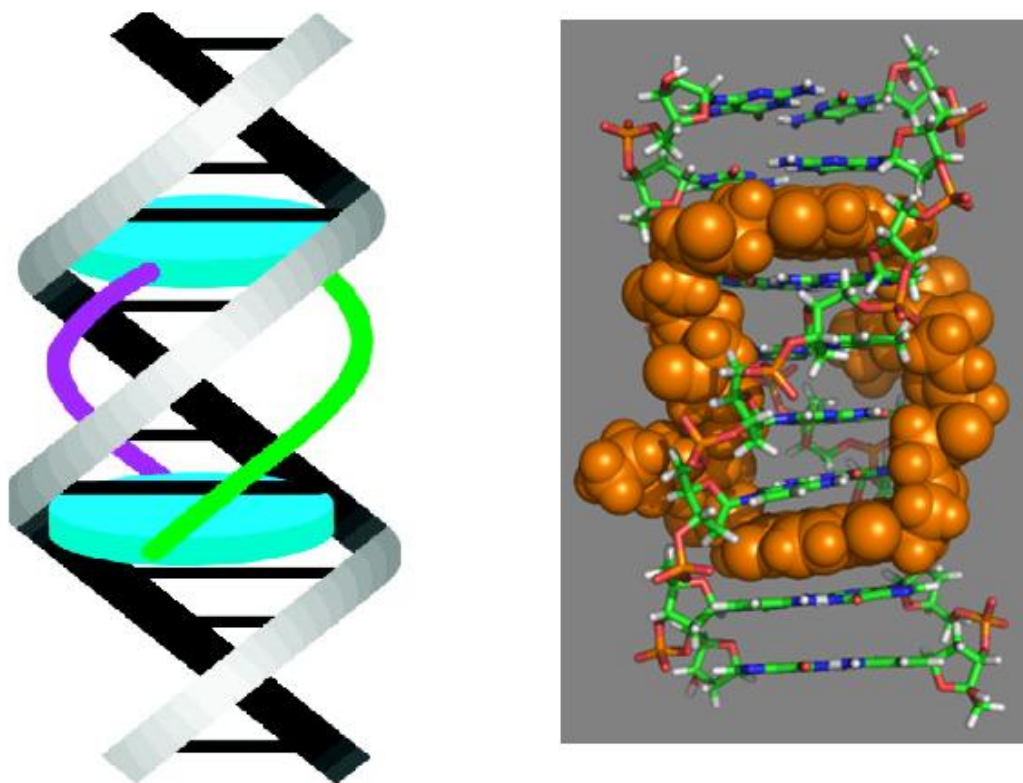
Figure 2.4 A simple model for intercalation for a cyclic *bis*-intercalator (left) and a structural characterization of the bound complex (right) based on NMR data. These results were obtained by Y. Chu in the Iverson laboratory.

Cellular DNA is highly compact and DNA is not as accessible as it would be purely in solution. The DNA is wrapped around histone molecules to form nucleosome core particles and these nucleosomes are the primary substrates for most biological activity in the genome. Therefore, the sliding type mechanism may be the most viable with regard to potential future examinations into the *in vivo* capabilities of these types of intercalators. It would be useful for a DNA binding molecule to bind the DNA at the most accessible portion in the nucleosome and then slide along the DNA until it locates its binding site since binding sites located in the internal portions of DNA may be hard to

reach in the histones. While these types of cellular studies for the cyclic *bis*-intercalator are not within future experimental designs, they would provide great insight into its viability as a potential *in vivo* gene-targeting molecule and assist in our understanding of how these complex intercalators can locate their preferred sequence within a long strand of DNA.

2.3 EXPERIMENTAL DESIGN

Gold nanoparticles offer an excellent choice as a molecular probe owing to their high density, which allows them to be visualized in the electron or atomic force microscope. The nanoparticles designed by Nanoprobes® will be used because of their monodisperse size and extensive use as molecular probes. Incorporating a cysteine residue onto the cyclic *bis*-intercalator (CBI) will allow for conjugation to a maleimide functionalized gold nanoparticle and the appropriate reaction characterization and purification protocols can then be developed.

It will then be necessary to design and visualize DNA containing CBI's preferred binding sequence. An approximate 500-bp DNA strand will be designed to contain one binding site located in the center of the DNA. Based on previous footprinting results on a 70 bp DNA fragment, 1.5 hours was sufficient for a clear footprint (Chu 2007). Extrapolating this to a larger strand could mean that approximately 10-hour incubation should be long enough to reach equilibrium. By examining a portion of the incubation of CBI-Cys with a single binding site DNA strand at various time points (every 30 minutes), it should be possible to assess non-specific binding and begin to develop an understanding of the binding-site location mechanism. While this will not be definitive in developing a mechanistic understanding, there is the potential for various extremes to be visualized, which would strongly support or rule out a particular mechanism. Figures 2.5 and 2.6 summarize these possibilities.

It may also be possible to develop a statistical analysis of non-specific binding. The microscopy studies could be used to assess how many nanoparticles on average are located on individual DNA strands throughout the incubation process. It is also possible that due to the expected structural distortions of the DNA induced by CBI binding, there is very little non-specific binding that can be directly assessed through the visualization of the individual DNA molecules. This could be supplemented by a DNase I footprinting experiment similar to the one undertaken by Holman on the tetraintercalator.
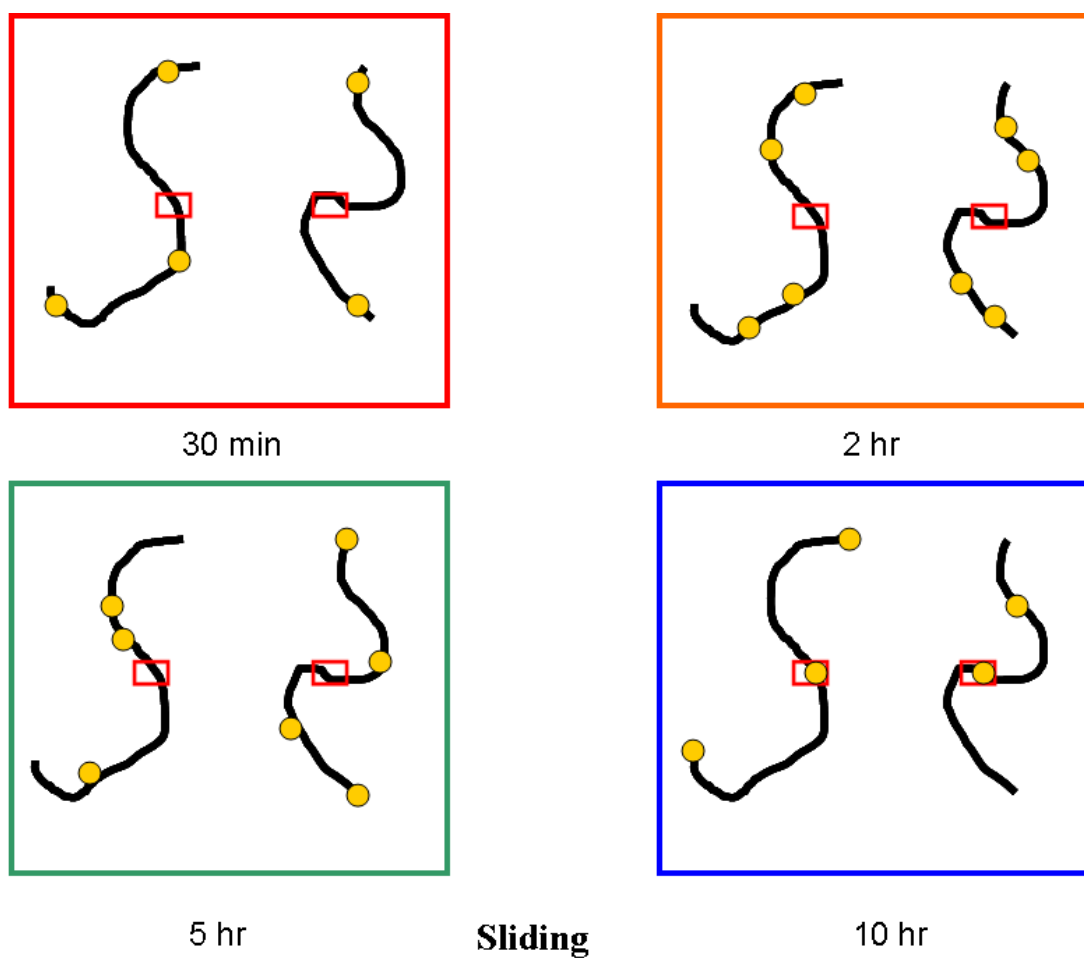
Figure 2.5. A simplistic view of the sliding mechanism. The yellow circles represent gold nanoparticle conjugated to CBI. An extreme scenario would show less intercalators randomly associated with the DNA and an increase of intercalators located at the ends of the DNA during the initial time points. The binding sites located at the center, would on average take a longer time to become occupied when compared to the association-dissociation mechanisms.
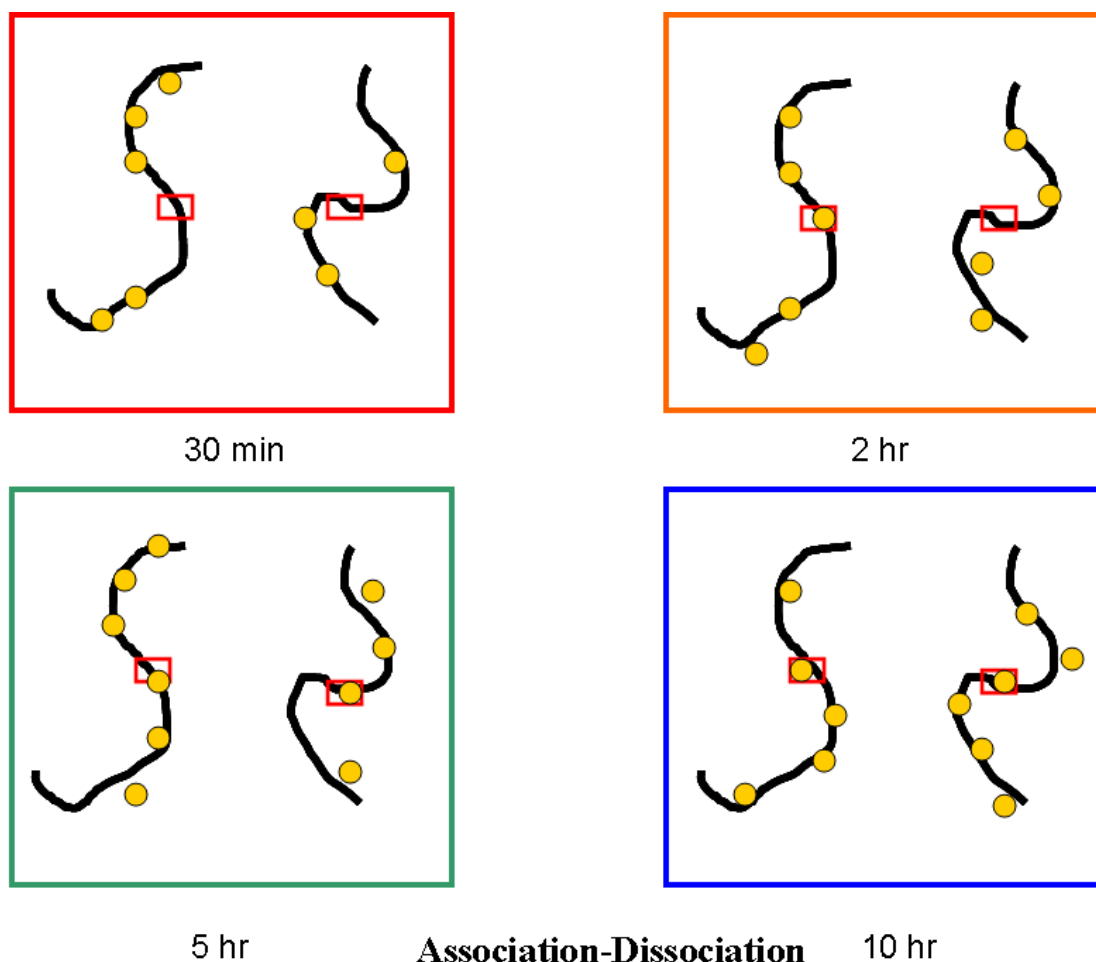
Figure 2.6. A simplistic view of the association-dissociation mechanism. With association-dissociation, it would be anticipated that more intercalators would be randomly associated with the DNA throughout the various time points. The binding sites would also become occupied at a random rate.

2.4 SUMMARY OF RESULTS

The cyclic *bis*-intercalator was designed and synthesized to incorporate a cysteine residue on the β-Alanine peptide linker (CBI-Cys) (Figure 2.9). The nanoparticles were conjugated to the intercalator and the proper purification protocol was developed. The necessary 1:1 ratio was not achieved (Figure 2.12, Table 2.1). The DNA visualization was partially successful in that some plasmid images were obtained (Figure 2.16).

However, the electron microscopy proved to be unreliable and the methodology used for the AFM plasmid images (Figure 2.18) was not successful in visualizing smaller DNA fragments.

2.5 SYNTHESIS OF CBI-CYS

2.5.1 Results

The original CBI contains two lysine residues. Directly conjugating this to a functionalized gold nanoparticle would lead to challenging purification of mono and di-conjugated species. Incorporation of a cysteine residue would allow for a 1:1 conjugation to the mono-functionalized gold nanoparticle containing a maleimide functional group provided the reaction occurred at the appropriate pH (Figure 2.7).
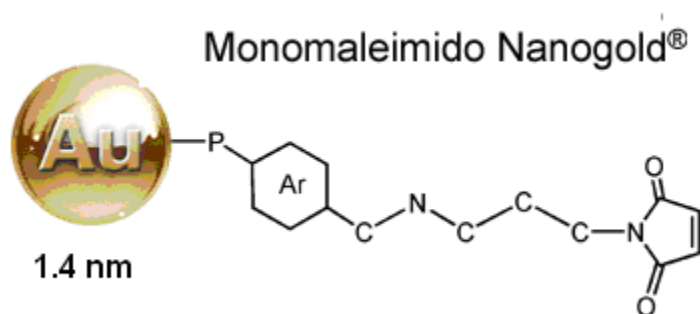
Figure 2.7. Monomaleimido Nanogold®.

The remaining lysine residue was used as a synthetic handle to the solid phase resin. A low loading PEG resin was used to maximize the cyclization, because a higher loading resin would lead to an increase in intermolecular reactions and hinder the intramolecular cyclization. An additional protecting group resistant to basic conditions was necessary to allow for the synthesis of a cyclic product. An allyl group was used as

the orthogonal protecting group because it would not be affected by the basic conditions necessary to remove the Fmoc group.

The allyl group was incorporated into an Fmoc-protected lysine amino acid and the NDI amino acid, while the cysteine residue was incorporated into the NDI unit using a solution phase peptide coupling protocol (Figure 2.8). Activation of the resin using N-N'-disuccinimidyl carbonate (DSC) and 4-(dimethyl amino) pyridine (DMAP) formed a carbonate to which the allyl protected lysine residue was attached for the first coupling step. Three glycine residues were attached to the N-terminus of the lysine residue using standard solid phase synthesis protocols. The allyl group of the lysine residue was then removed using a palladium catalyst ($Pd(PPh_3)_4$) in an overnight reaction (Fernandez-Forner 2001) followed by the coupling of the allyl-modified NDI amino acid. The NDI-cysteine amino acid was then incorporated onto the glycine residue, followed by three successive couplings of β-alanine residues. The allyl group was then removed in a second overnight reaction and the cyclization (Figure 2.9) was complete within 96 hours using PYBOP and 1-hydroxy-7-azobenzotriazole (HOAT). The product was cleaved from the resin and the identity of CBI-Cys **(5)** in both its oxidized and reduced forms was confirmed by high res ESI-MS and MALDI-TOF.

2.5.2 Discussion

CBI-Cys was rigorously purified via HPLC. Since the purification occurs in an acidic environment, the pH is low enough (thiol pKa approximately 8.3) so that equilibrium will strongly favor the protonated form and prevent oxidation during purification. However, the conjugation with the maleimide-functionalized nanoparticles best occurs in a pH range of 6-7 and so the intercalator is to be added from a neutral aqueous solution. It was therefore necessary to characterize the oxidized product so that it could be detected prior to conjugation.
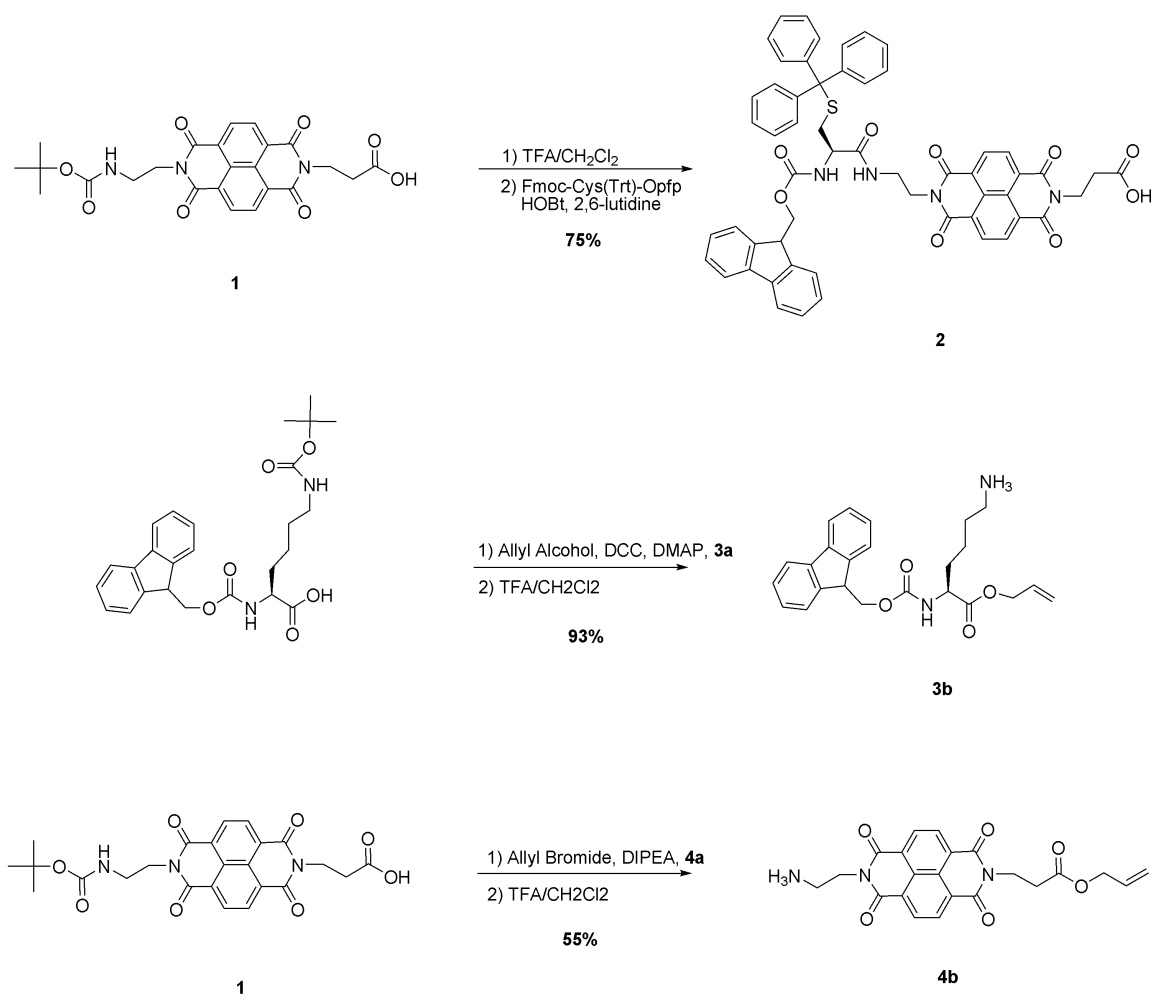
Figure 2.8. Synthesis of starting materials for solid phase synthesis.
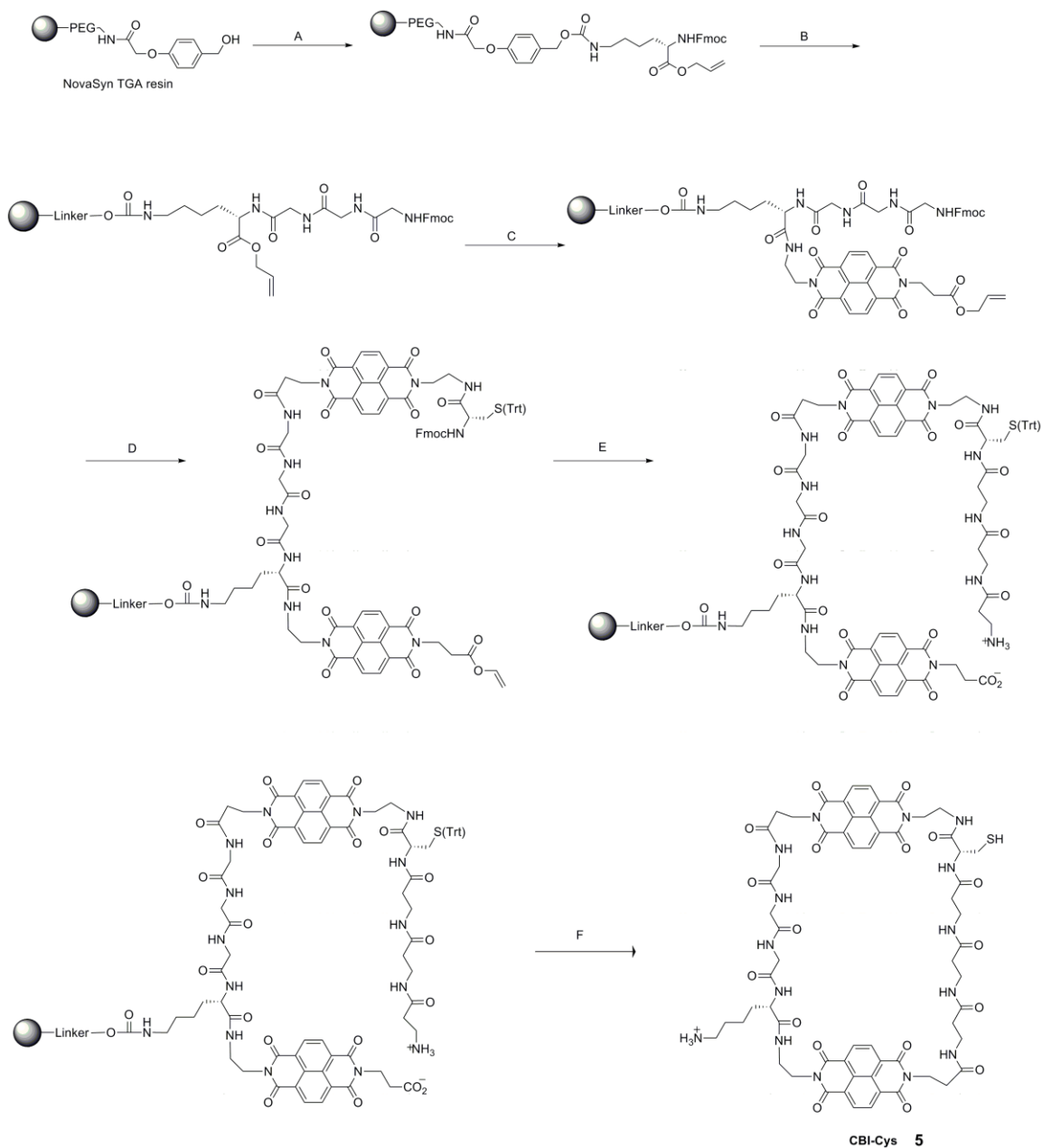
Figure 2.9. Solid Phase Synthesis of CBI-Cys. (A) Activation of resin, followed by coupling of **3b**. (B) Coupling of three glycine residues. (C) Coupling of **4b**. (D) Selective removal of the allyl protecting group, followed by the coupling of **2**. (E) Coupling of three beta-alanine residues, followed by the removal of the allyl protecting group. (F) Cyclization of the linear dimer to form CBI-Cys **5**.

47

A small sample of CBI-Cys was left in water for several days, the oxidized product was verified by ESI-MS and MALDI-TOF. As a further means of verifying that oxidization had occurred, tris-(2-carboxyethyl)-phosphine (TCEP) was used as a reducing agent. Upon adding an excess of TCEP to the solution, the reduced peak reappeared and the peak area of the oxidized product was significantly decreased (Figure 2.10). This verified that the second peak present was the oxidized species of CBI-Cys and provided a simple means to show that the CBI-Cys was primarily in its reduced form prior to the conjugation reaction.
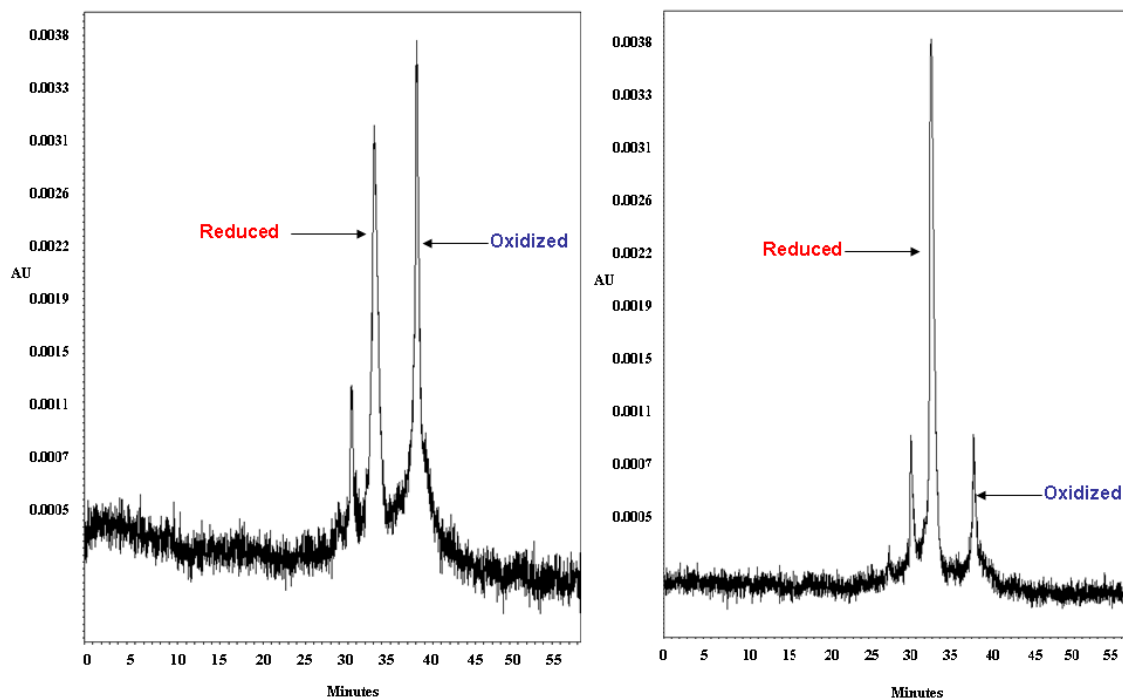
Figure 2.10. HPLC chromatograph of oxidized and reduced solutions of CBI-Cys. The figure on the right represents the solution after the addition of TCEP.

2.6 NANOPARTICLE CONJUGATION TO CBI-CYS

2.6.1 Nanoparticle Conjugation Results

After confirming that CBI-Cys was present in its reduced form, the stock solution concentration was determined using UV-Vis spectroscopy. A large excess of CBI-Cys was added to the nanoparticle (AuNP) solution and incubated overnight. The nanoparticles were analyzed via reverse-phase HPLC to determine if this would be a sufficient purification method. However, it was not possible to determine appropriate conditions to elute the nanoparticles as a single peak (Figure 2.11). Therefore, dialysis was chosen as a purification means, owing to its simple set-up and its cost effectiveness compared to expensive size-exclusion columns. After overnight dialysis, UV-Vis spectroscopy was used to assess the conjugation. After the initial dialysis, it was determined that there was an approximate 3:1 ratio (Figure 2.12, Table 2.1) of CBI-Cys to AuNP. Several dialyses were unable to get the ratio below 2:1 of CBI-Cys to AuNP.

2.6.2 Nanoparticle Conjugation Discussion

HPLC was thought to be a reasonable means of purifying the reaction due to the rigorous characterization of CBI-Cys via this method. Various solvent systems using combinations of aqueous, buffered, and organic solvents (methanol, isopropanol, and acetonitrile) were attempted but none of the combinations allowed for the nanoparticles to elute as one sharp or evenly broad peak. The likely reason for this is that the reverse phase column being used was not meant to separate highly dense materials such as gold nanoparticles. One could reason that this inconsistency would cause the nanoparticles to non-uniformly elute through the column, following multiple random pathways and leading to a long elution time with non-uniformity in the peak height and area. Membrane centrifugation was also attempted, using a membrane with a molecular weight

49

cut off below that of the nanoparticle but larger than CBI-Cys, so that unreacted CBI-Cys could be removed. However, this lead to the nanoparticles "crashing out" of solution as its concentration was rapidly increased due to the decrease in solution volume and caused significant sample loss.
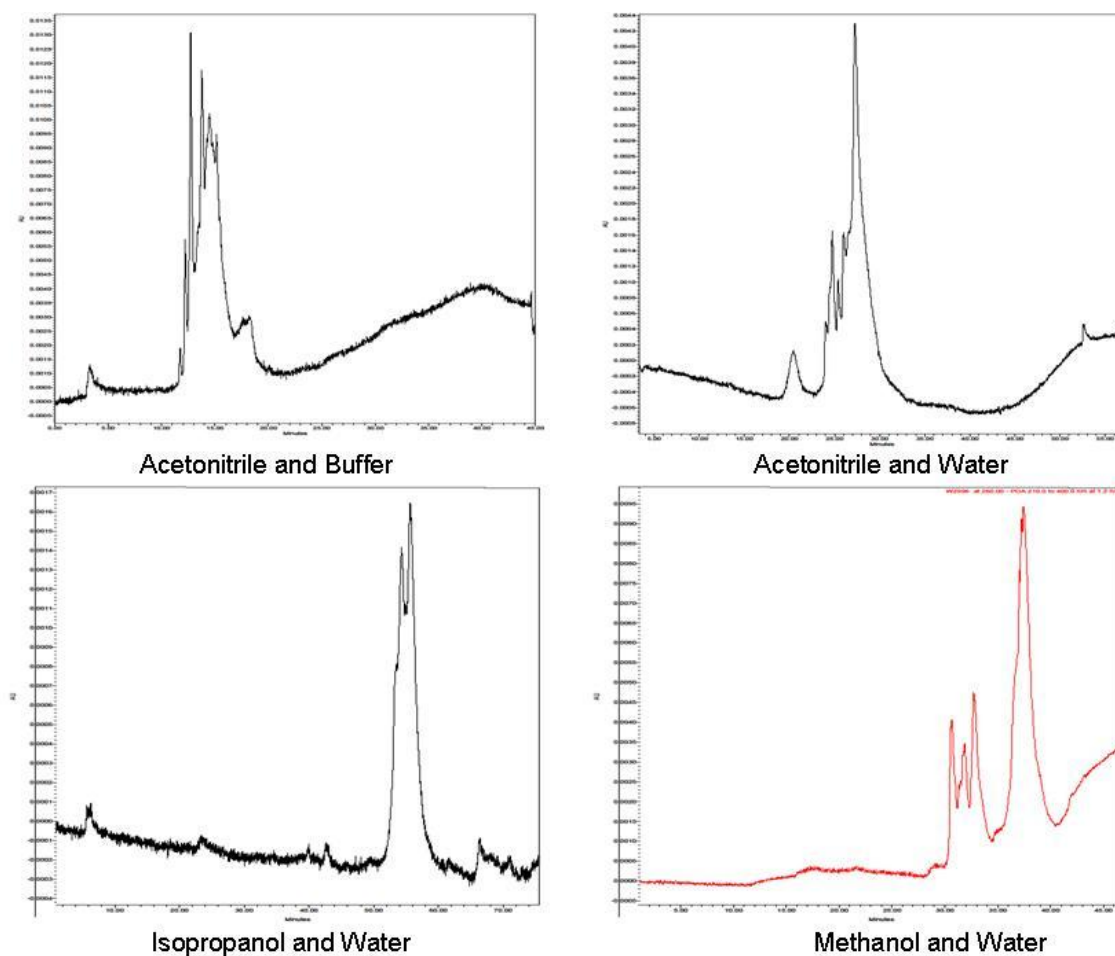
Figure 2.11. Summary of nanoparticle purification attempts.

Dialysis was then chosen as an alternative means of purification. It allows one to avoid chromatographic techniques such as HPLC or size exclusion and still utilizes the difference in molecular weight as a means of separating unreacted material. However, as

stated previously, several dialyses (including several overnight dialyses) were unable to bring the ratio of CBI-Cys to Au near a 1:1 ratio (Dialysis 2, Table 1). It was initially hypothesized that the hydrophobicity of the NDI portion of the intercalators may have been causing them to aggregate around the nanoparticles, so that multiple intercalators were non-covalently associated with the nanoparticles and unable to be separated through dialysis. Adding a detergent, such as SDS, should be able to break up any aggregated intercalator. However, this technique did not improve the overall ratio, which remained at approximately 2.5:1 (Dialysis 3 and 4, Table 1).
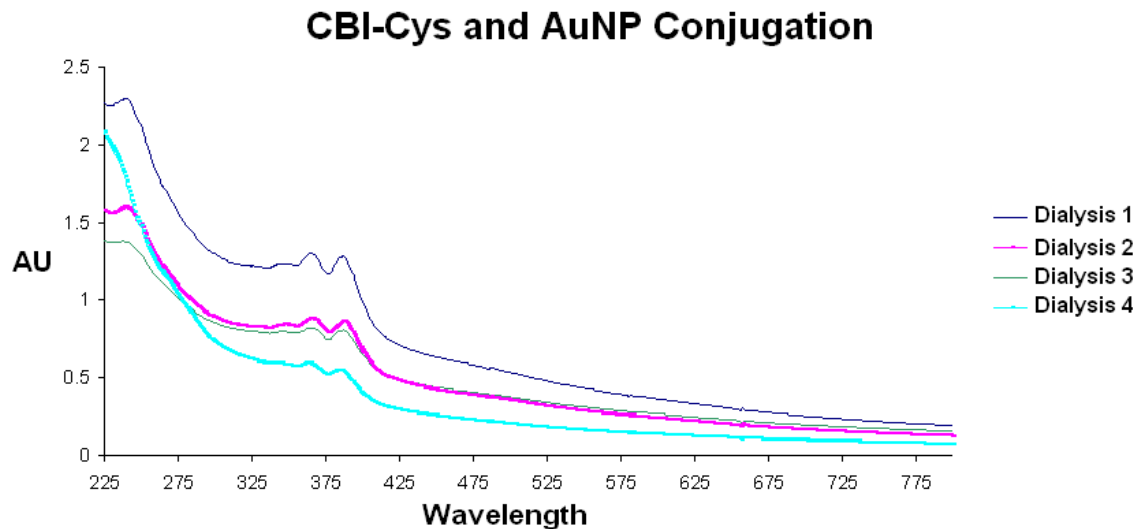
Figure 2.12. UV-Vis Data of gold nanoparticle conjugation to cyclic *bis*-intercalator.

Dialysis	Absorbance at 420	Absorbance at 385	Absorbance at 385 from CBI-Cys	NP Concentration (M)	CBI-Cys concentration (M)	Ratio of CBI-Cys to Au
1	0.736	1.271	0.3584	4.718×10^{-6}	1.308×10^{-5}	2.77
2	0.494	0.858	0.254	3.167×10^{-6}	8.957×10^{-6}	2.82
3	0.505	0.8002	0.174	3.237×10^{-6}	6.350×10^{-6}	1.96
4	0.303	0.551	0.176	1.924×10^{-6}	6.423×10^{-6}	3.33

Table 2.1. Calculation of Au: CBI-Cys ratio. The ratio of the nanoparticles absorbance at 385/420 was given by the manufacturer to be 1.24. The following equation was then used based on that ratio, to determine the absorbance at 385 due to CBI-Cys: $A_{385(CBI-Cys)} = A_{385} - (1.24 * A_{420})$. The extinction coefficient of the nanoparticles at 420 is 1.56×10^{5} and CBI-Cys at 385 is 2.74×10^{4}.

It was then reasoned that since a significant excess of thiol-containing CBI-Cys was added to the nanoparticles and the conjugation reaction proceeded overnight, the excess thiols began to exchange with the phosphorous containing ligands which stabilize the outer layer of the nanoparticles. This phenomenon has been extensively studied (Muray Langmuir 2004; Hutchinson J Am Chem Soc 2005). It is likely due to the enthalpic favorability of the gold-thiol bond when compared to the gold-phosphorous bond. Future conjugations of the CBI-Cys or any other cysteine-substituted intercalators will have to be done at a much lower concentration of thiol with a shorter reaction time.

2.7 GOAL AND PURPOSE OF MICROSCOPY

In order to assess the binding mechanism for the cyclic *bis*-intercalator, it is necessary to determine the appropriate conditions that allow for the assessment of individual DNA molecules.

2.8 TRANSMISSION ELECTRON MICROSCOPY

2.8.1 TEM Results

Several methods exist for visualizing DNA in the electron microscope. One of the most common methods used is rotary shadowing. However this type of sample preparation would not be appropriate for these particular experiments. The methods attempted were all unsuccessful in the visualization of DNA molecules (Figures 2.13, 2.14, 2.15) with the exception of a protein spreading application (Figure 2.16). This same method did not allow for the visualization of smaller DNA molecules.

2.8.2 TEM Discussion

Table 2.2 summarizes the methods attempted and points out what makes each technique unique. Unlike AFM visualization of DNA, there is little found in the literature which accurately describes the process by which DNA is bound to the sample surface. The most common technique uses a carbon surface that is plasma-treated. This is necessary in order to provide a hydrophilic surface for deposition of DNA from aqueous solutions. Beyond that, there is a lack of experimental data that discusses the process by which DNA binds to the carbon-coated grid.

For all techniques employed, it was necessary to add a contrast agent, since DNA does not contain atoms dense enough to significantly alter the path of the electron beam. Initial studies using only the uranyl acetate stain led to images with large white aggregated areas but not individual DNA strands. Various concentrations of both negative stain and DNA were used and did not produce appropriate results (Figure 2.13). It was possible that the DNA was either aggregating on the grid or not spreading appropriately or that it was not uniformly absorbing to the grid.

Technique Employed	Unique Element	Result	Reference
Uranyl Acetate Staining	Negative staining	Could not visualize DNA	Bozolla and Russell
Alcian Blue with Uranyl Acetate Staining	Non-protein DNA spreading	Could not visualize DNA	Schnos and Inman
Poly-l-lysine with Uranyl acetate staining	Positively charged monolayer	Could not visualize DNA	
Rec-A protein	Protein to assist in DNA spreading	Imaged plasmid DNA	Savva

Table 2.2. Summary of electron microscopy DNA visualization methods.

In order to examine this, a non-protein based method was employed to hopefully assist in the spreading of the DNA on the carbon film. Alcian blue is a species with a positive charge at neutral pH and should provide a surface that would allow for the DNA to absorb to the grid based on an electrostatic interaction with the phosphate backbone. Polylysine was also used in a separate application. The main difference is that alcian blue is an aromatic molecule, so there could be a concern that once the DNA solution is added to the pretreated grid, any alcian blue molecules that dissociate from the grid surface could interact with the DNA in an intercalating manner. The use of poly-*l*-lysine avoids this issue and still provides a positively charged surface. Unfortunately, neither of these methods resulted in the successful imaging of DNA molecules (Figures 2.14, 2.15).

The final attempt utilized a protein-spreading method via Rec-A, which binds the DNA (Domborski 1983) and allows for it to spread along the carbon coated grid. The DNA sample was again stained with uranyl acetate and images of individual plasmid DNA were obtained (Figure 2.16). When using the same method with smaller linear

DNA fragments, however, images were not obtained. While this was promising, the preparation required for this method raised concerns. The protein has to slightly unwind the DNA helix in order to bind. This process could easily displace already bound intercalator, especially if it was weakly bound to a non-specific sequence in the DNA. During the preparation, the sample is also heated and this could adversely affect the interaction between the DNA and intercalator-nanoparticle conjugate. This would interfere with the analysis and could provide misleading results.
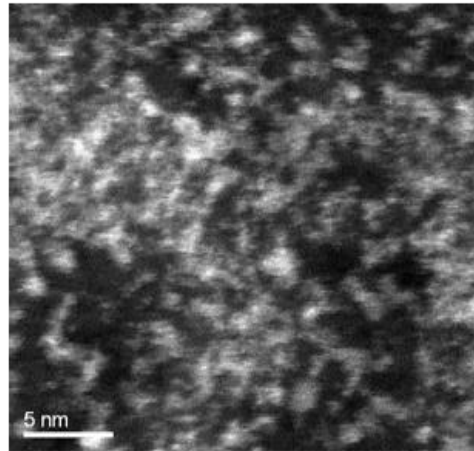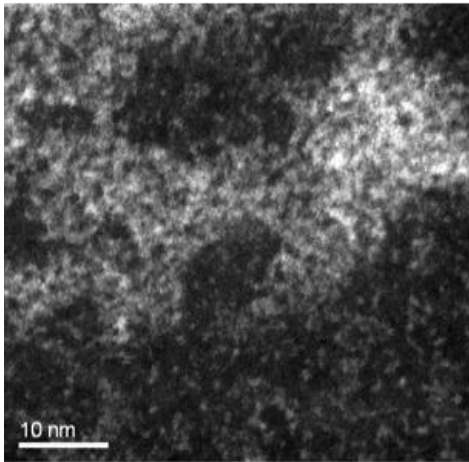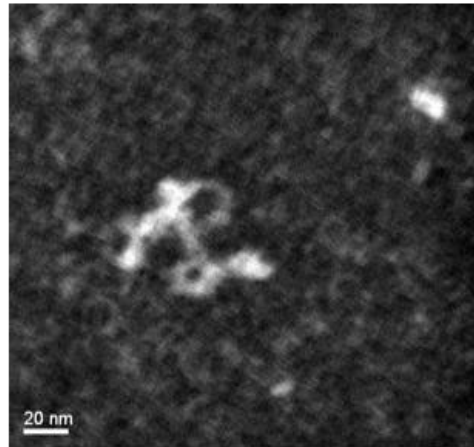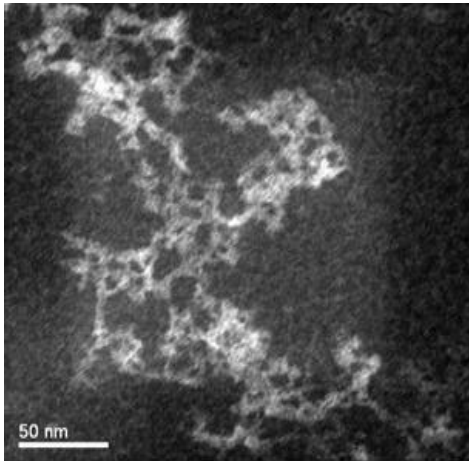
Figure 2.13. Images using a uranyl acetate stain.
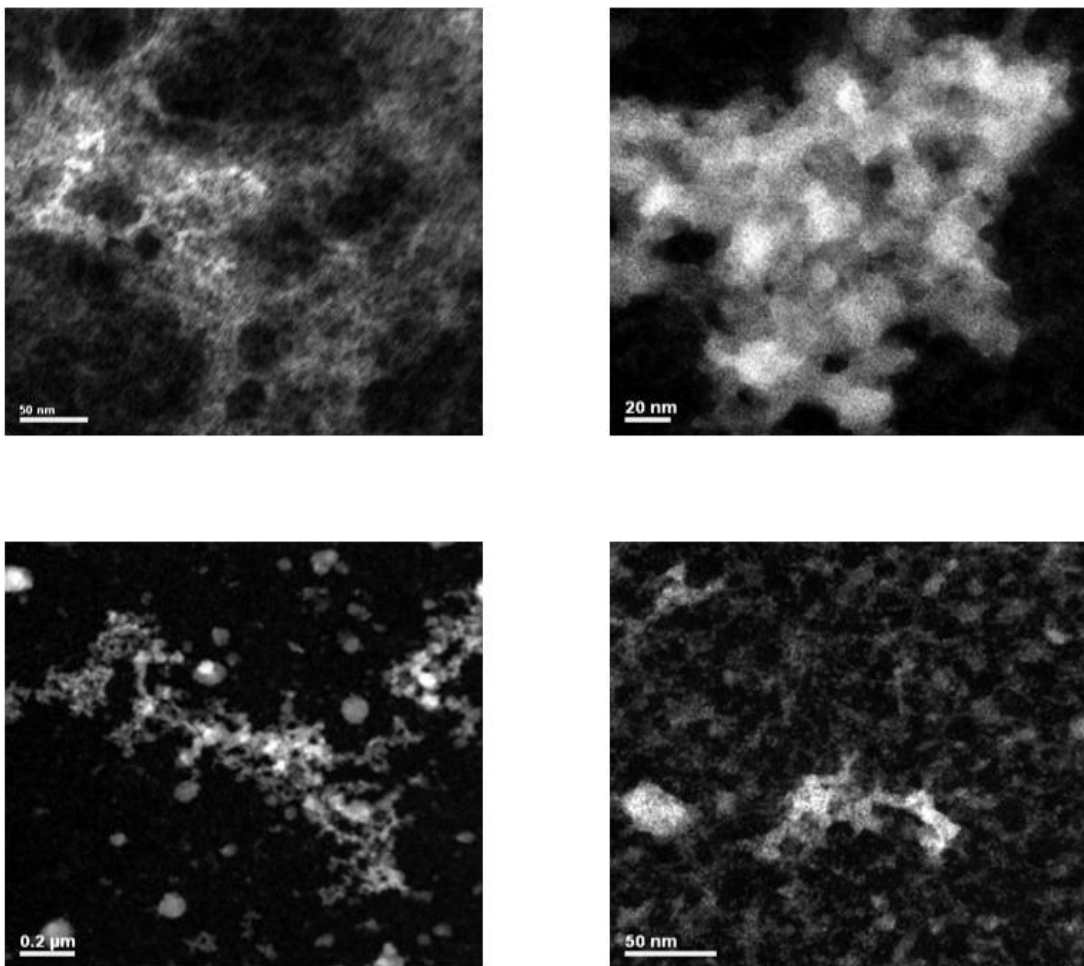
Figure 2.14. Pre-treatment of the grid with poly-l-lysine followed by Uranyl Acetate
        Stain.
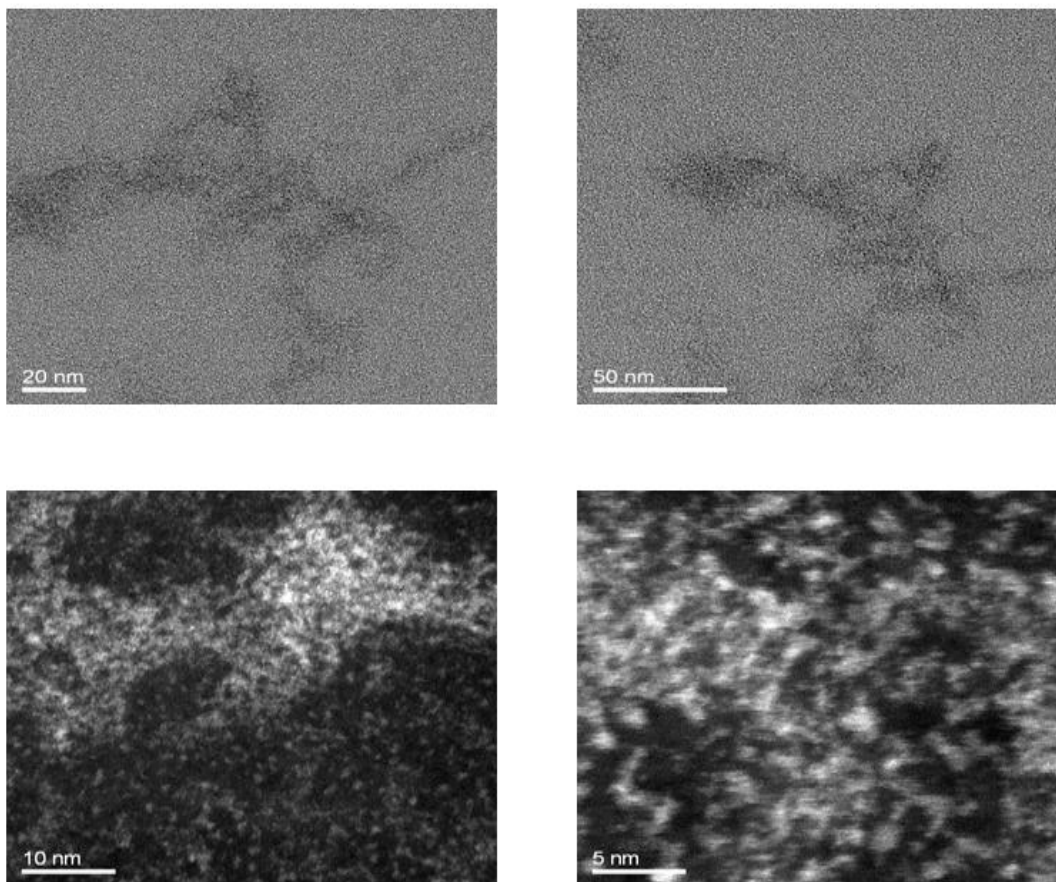
Figure 2.15. Alcian Blue pretreatment followed by Uranyl acetate stain.
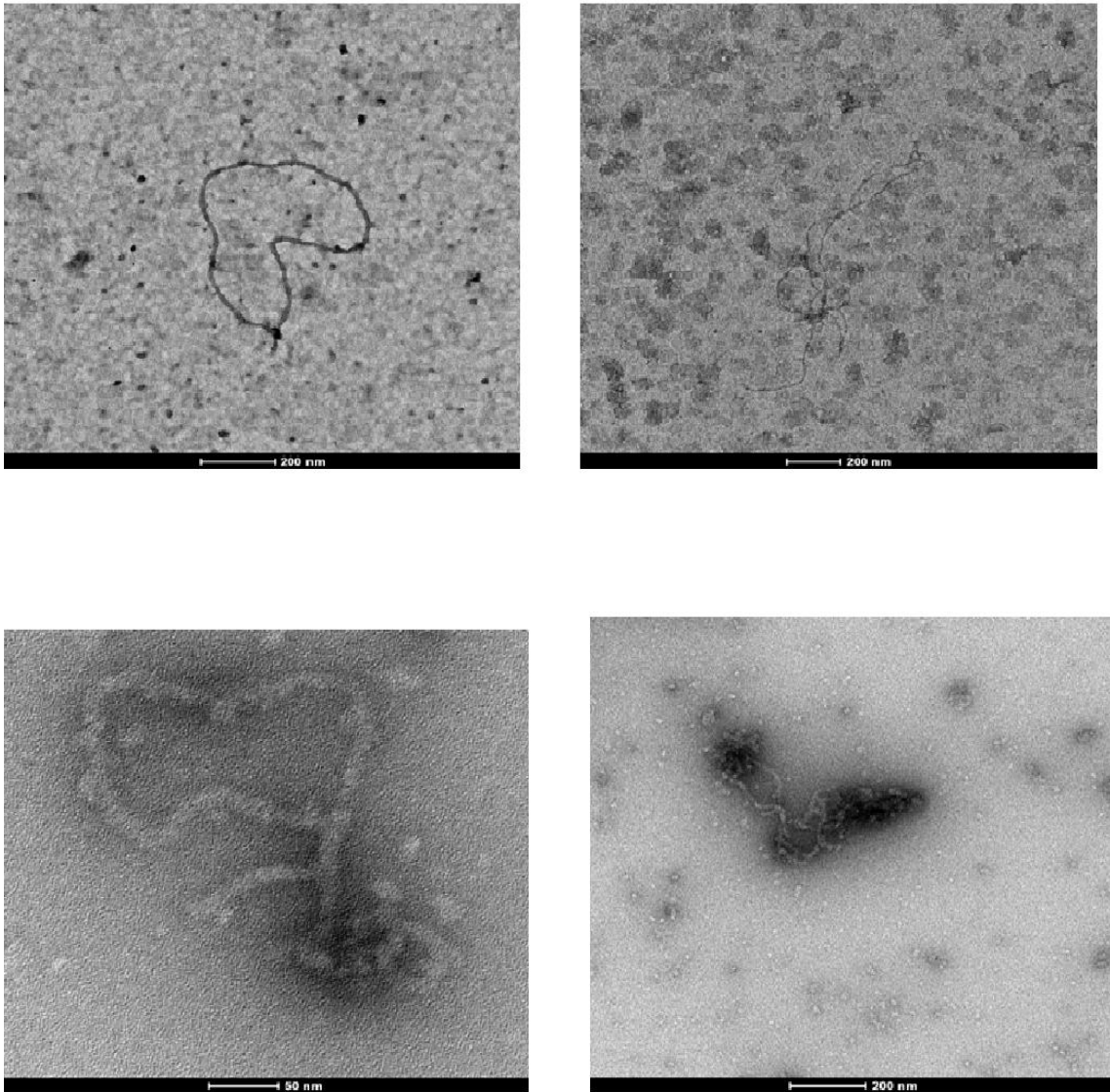
Figure 2.16. Images of plasmid DNA obtained via the RecA protein coating technique. The scale bar is 200 nm for all images, except the bottom left image which has a scale bar of 50 nm.

2.9 ATOMIC FORCE MICROSCOPY BACKGROUND

2.9.1 AFM Results

Images of plasmid DNA were obtained using a magnesium ion-based method for DNA absorption to a mica grid (Figure 2.18). However this method was unsuccessful in imaging the smaller DNA molecules. Polylysine was also used but resulted in significant background noise with regard to deciphering small topological changes.

2.9.2 AFM Discussion

Beyond the chemical processes of DNA binding to the mica surface, it is vitally important that the mica sheets are properly cleaved to provide a flat sample surface. Initial studies were inconclusive due to poor mica cleavage, resulting in large peaks and valleys in the mica surface (Figure 2.17). Once the issue was solved, the next problem was to determine proper concentrations of $MgCl_2$ and DNA to allow for the analysis of individual DNA molecules.

Table 2.3 summarizes the concentrations of DNA and $MgCl_2$ used for both the plasmid DNA and the smaller 500 bp fragments. Decreasing the DNA concentration did not improve the separation of DNA molecules. It is possible that the divalent salt concentration was too high, causing an overloading of DNA molecules which absorbed to the surface. One study found that adding monovalent salts such as NaCl helps to avoid DNA aggregation because the Na^+ ions compete with magnesium to bind the mica surface. It is also possible that premixing the DNA with the $MgCl_2$ solution may have caused the individual DNA molecules to aggregate in solution. Future studies should explore these possibilities by using different ratios of divalent: monovalent salts as well as pretreating the mica surface with $MgCl_2$.

202.6 nm · 5.3 nm

0   5 um   0.0   5 um

Unevenly cleaved Mica Surface   **Evenly Cleaved Surface**
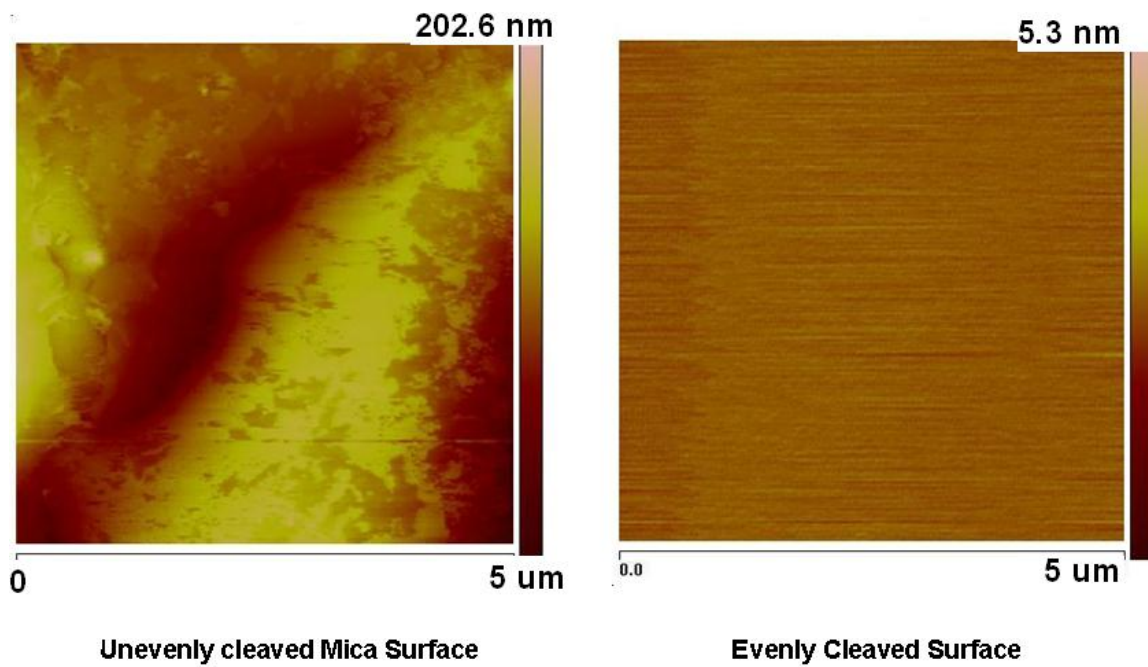
Figure 2.17. A comparison of an unevenly cleaved and evenly cleaved surface clearly shows that it would be difficult to visualize small DNA molecules on an unevenly cleaved surface. The scale bar on the right is the height measurement (topography). DNA has a height of approximately 2 nm on mica.
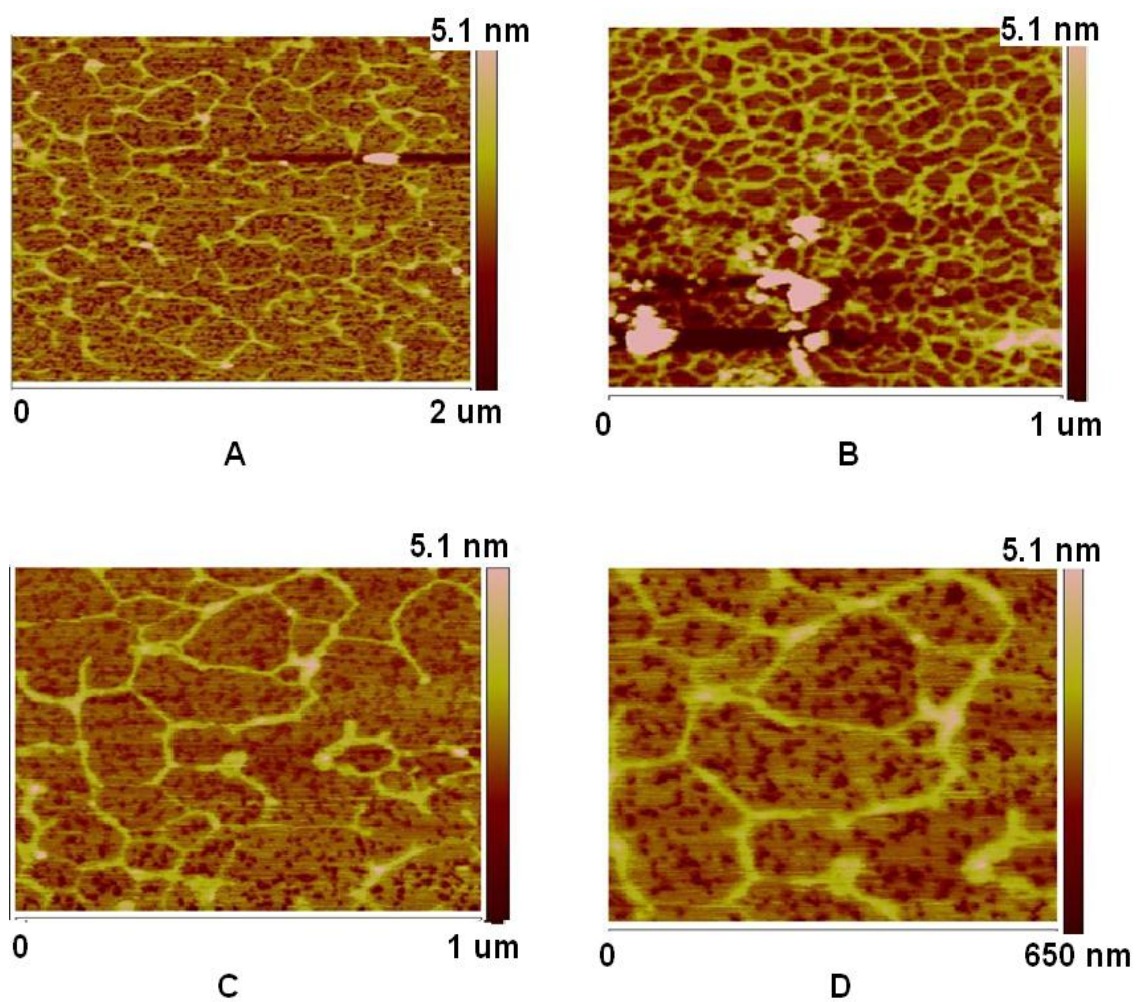
Figure 2.18. Plasmid Images of DNA. A and B represent different areas of the grid, with C and D representing areas of increased magnification of B.

DNA Type	DNA Concentration (nM)	MgCl$_2$ (nM)
Plasmid (5400 bp)	15.15	1.8
Plasmid (5400 bp)	1.515	1.8
Linear DNA (500 bp)	149	1.9
Linear DNA (500 bp)	156	9
Linear DNA (500 bp)	3	1.9
Linear DNA (500 bp)	15	1.9

Table 2.3. Summary of salt and DNA concentrations for AFM Images.

While the plasmid DNA images were obtained through this method, the smaller DNA fragments were not visible. Various concentrations of salts and DNA were used and were unsuccessful (Table 2.3). It is possible that the smaller DNA fragments, containing less negatively charged sites, may not initially approach the mica surface and as such, the first binding event is not occurring. Again, mica pre-treatment may enhance binding because the divalent salts can reversibly bind to the surface without any initial competition from the DNA. This could reduce the repulsive forces of the negatively-charged mica surface by maximizing the initial divalent salt binding to the mica.

2.10 CHAPTER SUMMARY

The ultimate objective was to gain visual evidence that would assist in our understanding of how a complex cyclic *bis*-intercalator could locate its preferred sequence within a long strand of DNA. Such an experiment requires the proper techniques to study individual DNA molecules. Microscopy and DNA visualization is an

entirely separate area of research, with a significant learning curve to not only understand the principles behind the operation of the instruments, but to also understand the differences between all the various techniques used to prepare and visualize DNA samples.

For our purposes, it has become apparent that DNA visualization via electron microscopy may not be the most appropriate technique for our initial studies. One aspect of sample preparation that was not used was rotary shadowing, as the coating of such a heavy metal would likely obscure the small gold nanoparticles. This may have very well been the reason why individual DNA molecules were not visualized. Fortunately, the Atomic Force Microscope offered a new hope in DNA visualization. Not only were actual images of DNA obtained, but the literature provided more details of the process by which DNA is absorbed to a mica surface and this provides a means of reasoning why certain sample preparations may or may have not worked properly.

With regard to the nanoparticle probe, the initial conjugation reactions showed that an excess of thiol containing intercalator can exchange with the gold's phosphorous based ligands. Future experiments can be targeted to avoid this issue and ensure a 1:1 conjugation. It is imperative that each nanoparticle bound to the DNA can be assumed to have only one intercalator conjugated to it in order to accurately assess the mechanism of binding site location.

2.11 FUTURE GOALS

The AFM has shown to be the most promising with regard to visualizing individual DNA molecules. Future work in that area should focus on a larger concentration range of divalent cations and DNA as well as examining other techniques used to modify chemically the mica surface, such as the APTES modification. This type

of surface modification could potentially provide a stronger interaction than the divalent salt bridge, and may assist in the visualization of smaller DNA strands.

The nanoparticle conjugation also needs to be optimized but there should also be studies to examine whether the nanoparticle actually interferes with DNA binding. The synthesis needs to be redesigned to allow for incorporation of the gold nanoparticle on both the major and minor groove and each of these species tested, assessing where the nanoparticle should be placed to maintain optimal binding. Recent experiments have indicated that the nanoparticle covalently linking directly off the peptide linker can inhibit binding and that extending the cysteine residue from the linker has assisted in maintaining binding specificity.

It may also be possible to attempt a different approach if the 1:1 conjugation cannot be achieved or if the nanoparticles inhibit binding. An approach often utilized to examine protein-based interactions involves the attachment of a biotin molecule to the protein of interest, incubation of the protein with the DNA, and then final incubation of that complex with streptavidin coated gold nanoparticles. The biotin molecule may be incorporated to the cyclic *bis*-intercalator during solid phase synthesis and would allow for the identification of the cyclic *bis*-intercalator after it is bound to DNA to avoid the potential problem of the nanoparticle inhibiting binding. These types of nanoparticles are also generally larger in size and would be more easily visualized in the AFM.

EXPERIMENTALS

General

All chemicals were purchased from Sigma-Aldrich or Acros organic. Peptide starting materials and coupling reagents were purchased from Novabiochem. Dialysis membranes and TCEP were purchased from Piercenet. Silica 60 F_{254} glass-based plates (Merck) were used for TLC. Flash Chromatography was carried out using ICN SiliTech 32-63D 60 A^o silica gel. All NMR spectra were recorded on Varian 400 or 600 MHz Instruments. CDCl$_3$ (δ_H = 7.26, δ_C = 77 ppm), DMSO-d$_6$ (δ_H = 2.5, δ_C = 140.9 ppm), and D$_2$O (δ_H= 4.67 ppm) were used as solvents. Nanoparticles were purchased from Nanoprobes Incorporated®. TEM grids and poly-l-lysine were purchased from Electron Microscopy Sciences, containing carbon or formvar coated over copper (400 mesh.) Mica sheets were purchased from Ted Pella Inc, or SPI. AFM probes were purchased from NanoAndMore. Either NCH or PPP-NCH probes under the non-contact, tapping mode section were used.

TEM Samples of AuNP

All carbon coated grids were plasma treated prior to sample preparation. Nanoparticle samples were prepared by addition of 5 uL of gold nanoparticle solution to the grid, and after five minutes, the solvent wicked off and dried under a lamp for several minutes. Varying concentrations were used and at least 5 different areas of the grid were examined to ensure images were representative of the entire sample. Images were obtained on a JEOL 2010F Transmission Electron Microscope operating at 200 kv using both the TEM and STEM mode.

TEM Samples of DNA

All carbon coated grids were plasma treated prior to sample preparation. For negative staining samples, a 5 uL drop of DNA solutions of varying concentrations was placed on a carbon or formvar coated copper grid and incubated for 1-10 minutes. The grids were

washed with 5 uL of diH_2O one time and then uranyl acetate solutions ranging from 0.5 to 3% were placed onto the grid for 30 seconds. The uranyl acetate was removed and the grid washed twice with diH_2O.

For the alcian blue protocol, a solution of 0.2% in alcian blue with 3% acetic acid was prepared in diH_2O. Then, 1 mL of this stock solution was diluted to 100 mL, filtered through a 0.45 um syringe filter and 5 uL of this solution was incubated on a plasma treated carbon coated grid for 5 to 10 minutes. The grid was washed with water two times, followed by addition of DNA solutions at varying concentrations for 5 minutes, again washed with water, and then stained with 0.5% uranyl acetate for 30 seconds. The staining solution was removed and the grid washed twice with water and dried under a lamp for 1 to 2 minutes.

For the poly-l-lysine method, a solution of 2% poly-l-lysine was diluted 1,000x and 5 uL was added to a plasma treated carbon coated grid for 5 to 10 minutes. The solution was removed and then 5 uL of DNA was added for 5 minutes, wicked, and washed twice with water. The grid was then dried under a lamp for 1 to 2 minutes.

Texas A&M DNA Imaging

Courtesy of Dr. Christos Savva at the Microscopy and Imaging Center at Texas A&M University, a method involving RecA protein was utilized to visualize individual DNA plasmids. 2 uL of a 40 ng/uL solution of DNA plasmid (7000 bp) was added to 11 uL of 25 mM TEA buffer at pH 7.6. To this solution, 1 uL of RecA protein (2 mg/mL), 2 uL of 2 mM ATP, and 4 uL of 1 mM Mg acetate were added. The solution was incubated at 37° C for 5 minutes. Then, 1 uL of ATP-γS was added to give a total concentration of 0.5 mM. This solution was then incubated for 30 min at 37° C followed by the addition of 2.3 uL of 2% glutaraldehyde in 75 mM TEA buffer. This solution was then incubated at 37° C for 15 minutes, followed by the addition of 2 uL of 2.5 M glycine and 0.5 uL of 0.5

M HEPES pH 7.6. The DNA samples (4 uL) were then added to a plasma treated carbon coated grid for 2 min, blotted with filter paper, and then placed onto a uranyl acetate stain droplet (2%) for 30 seconds. A TEM operating at 100 kV was utilized for imaging.

AFM Samples

Plasmid DNA (7000 bp) and a smaller DNA fragment (500 bp) was prepared using the divalent cation approach. After freshly cleaving a mica sheet (3.05 mm), a solution of DNA was mixed with $MgCl_2$, at the concentrations listed in Table 3, and the salt-DNA solution was incubated on the mica sheet for 10 minutes. The solution was blotted off with filter paper, washed with 5 uL of diH_2O three times, and dried under a stream of nitrogen. A Dimension 3100 AFM with a Nanoscope IV controller was utilized. The height scale bar was adjusted to 5nm as the flattest areas of the mica were examined. All images were first order flattened. Tip used had resonant frequencies ranging from 285 to 350 kHz.

***Tert*-butyl 2-aminoethylcarbamate**. To a solution of CH_2Cl_2 was added ethylenediamine (40 mL, 0.598 moles). The solution was cooled to $0^{o}C$ and a solution of tert-butoxy-ditert-butoxy carbamate (43.5 g, 0.199 moles) was added drop wise over 3 h. The reaction was allowed to warm to r.t. and the reaction was stirred overnight. The organic solvent was concentrated *in vacuo* and the remaining white solid dissolved in H_2O and filtered. The H_2O was extracted with CH_2Cl_2 (3 x 200 mL) and the organic solvent was then washed with brine (3 x 300 mL). The organic solvent was dried over Na_2SO_4 and concentrated to afford 1 as an orange oil (11.8g, 37%.) ^{1}H NMR (400 MHz, $CDCl_3$) δ 3.09 (q, 2H, *J*= 5.6), 2.71 (t, 2H, *J*= 5.6), 1.36 (s, 9H); [13]C (400 MHz, $CDCl_3$) δ 155.7, 79.5, 52.8, 44.3, 28.4; HRMS (ESI) calculated for $C_7H_{17}N_2O_2$ $[M+H]^+$ 161.129, found 161.128.

N-(2-*tert*-Butoxycarbonylaminoethyl)-N'-(2-carboxyethyl)-1,4,5,8-napthalenetetracarboxylic diimide (NDI monomer) (1). β-Alanine (6.5 g, 0.0729 mol) and 1,4,5,8-napthalenetetracarboxylic dianhydride (19.6 g. 0.0729 mol) were sonicated in 250 mL of DMF for 1 h to effect dissolution. The mixture was then transferred to a 3-neck 1L round bottom flask, followed by the addition of TEA (10.3 ml, 0.0732 mol). The mixture was heated in a microwave reactor (Mars) at power = 600W, max = 100%, and spin = 3. The procedure followed a 2 min ramp to 140 C, holding at 140ºC for 10 min, then cooling to 65ºC. A mixture of 1 (11.7 g, 0.0729 mol) and TEA (10.3 ml, 0.0732 mol) was then added to the 3-neck round bottom flask. The flask was placed back into the microwave and the same settings and procedure as before were used. The flask was cooled and the solvent removed *in vacuo*. The resultant solid was dissolved in CH_2Cl_2/TEA/MeOH (85:10:5) and purified via column chromatography in a 5-7% MeOH gradient in 10% TEA in CH_2Cl_2. The collected fractions were concentrated and the resultant solid re-dissolved in 15 mL CH_2Cl_2, followed by addition of 15 mL of AcOH to neutralize the product. Addition of 500 mL of hexanes precipitated the product which was filtered, washed with H_2O, and dried *in vacuo* to afford 2 as a tan solid (8.5g, 40%). ^{1}H NMR (400 MHz, DMSO-d_6) δ 8.61 (s, 4H), 6.92 (t, 1H, *J*= 12.4), 4.27 (t, 2H, *J*= 4), 4.13 (t, 2H, *J*= 5.6), 3.28 (q, 2H, *J*= 5.6), 2.63 (t, 2H, *J*= 7.4), 1.25 (s, 9H); [13]C (400 MHz, DMSO-d_6) δ 173.2, 159.3, 155.2, 139.6, 135.2, 120.6, 79.5, 48.3, 38.9, 34.1, 31.3, 28.2; HRMS (ESI) calculated for $C_{24}H_{23}N_3O_8$ $[M+Na]^+$ 504.1382, found 504.1377.

3-(7-(2-(2-(((9H-fluoren-9-yl)methoxy)carbonylamino)-3-(tritylthio) (propanamido)ethyl)-1,3,6,8-tetraoxo-7,8-dihydrobenzo[lmn][3,8]phenanthrolin-2(1H,3H,6H)-yl)propanoic acid (Fmoc-Cys(Trt)-(CH₂)₂-NDI-(CH₂)₂-CO₂H or NDI-Cys monomer) (2). To a 100 mL round bottom flask was added 2 (1.25 g, 2.59 mmol) which was dissolved in 10 mL of CH_2Cl_2 followed by addition of 5 mL of TFA. After

TLC indicated complete boc removal, the solution was concentrated *in vacuo* followed by washing/evaporation with heptanes (3 x 50 mL). The solid was dried under vacuum overnight. The solid was then dissolved in 50 mL of NMP, followed by additions of HOBt (0.357 g, 2.59 mmol), Fmoc-Cys(Trt)-Opfp (1.95 g, 2.59 mmol), and 2,6-lutidine (1.06 mL, 9.09 mmol). The solution was stirred for 36 h. The solution was diluted to 500 mL with EtOAc and washed with 0.1M HCl (3 x 250 mL). The organic layer was concentrated to 250 mL and precipitated with 250 mL of hexanes. The precipitate was washed with diethyl ether and purified via column chromatography in CH_2Cl_2/MeOH (95:5) to afford 3 as a yellow, crystalline solid (1.71g, 75%). ^{1}H NMR (400 MHz, DMSO-d$_6$) δ 8.54 (s, 4H), 8.05 (t, 1H, *J*= 5.2), 7.84 (d, 2H, *J*= 7.6), 7.63 (d, 2H, *J*= 7), 7.39 (d, 2H, *J*= 8), 7.31-7.21 (m, 15H), 7.17 (m, 2H), 4.27 (t, 2H, *J*= 15), 4.14 (m, 3H), 4.08 (t, 2H, *J*= 15.2), 2.62 (t, 2H, *J*= 7.8), 2.36 (t, 2H, *J*= 6.8) ^{13}C (400 MHz, DMSO-d$_6$) δ 175.6, 173.9, 171.1, 163.1, 162.4, 156, 144.2, 143.3, 140.9, 130.8, 129.5, 128, 127.7, 127.1, 127.0, 126.8, 126.1, 124.9, 119.9, 67.3, 66.9, 53.9, 49.5, 46.7, 39.8, 38.6, 36.4, 33.4, 30.6, 29.7, 17.6; HRMS (ESI) calculated for $C_{56}H_{44}N_4O_9S$ [M+Na]$^+$ 971.2829, found 971.2739.

Allyl2-(((9H-fluoren-9-yl)methoxy)carbonylamino)-6-(tertbutoxycarbonylamino)hexanoate (Fmoc-Lys(Boc)-OAll) (3a). To a solution of Fmoc-Lys(Boc)-OH (2.5 g, 5.33 mmol) in CH_2Cl_2 was added allyl alcohol (0.4 mL, 5.87 mmol). The solution was cooled to 0°C and DCC (1.1 g, 5.33 mmol) and DMAP (33 mg, 0.267 mmol) were added. The cloudy solution was stirred at 0°C for 4 h, followed by gradual warming to r.t. and stirring overnight. The solution was filtered through celite, concentrated, and purified via column chromatography in CH_2Cl_2/Me)H (95:5) to afford 5 as a white foam (2.51g, 93%). ^{1}H NMR (400 MHz, CDCl$_3$) δ 7.75 (d, 2H), 7.59 (d, 2H), 7.38 (t, 2H), 7.29 (t, 2H), 5.91 (m, 1H), 5.31 (dd, 1H), 5.27 (dd, 1H), 4.65 (d, 2H),

4.40 (m, 3H), 4.22 (t, 1H), 3.12 (q, 2H), 1.87 (m, 1H), 1.67 (m, 2H), 1.53-1.50 (m, 2H), 1.48 (s, 9H), 1.43-1.35 (m, 2H); ^{13}C (400 MHz, CDCl$_3$) δ 172.1, 155.8, 143.7, 141.0, 131.3, 127.5, 126.8, 124.9, 119.7, 118.6, 78.8, 66.7, 65.7, 53.6, 46.9, 39.8, 33.7, 31.7, 29.3, 28.2, 23.3; HRMS (ESI) calculated for C$_{29}$H$_{36}$N$_2$O$_6$ [M+] 508.2573, found 531.3542.

Allyl 2-(((9H-fluoren-9-yl)methoxy)carbonylamino)-6-aminohexanoate (Fmoc-Lys-OAll) (3b). To a 100 mL round bottom flask was added 5 (2.51g, 6.14 mmol) which was dissolved in 10 mL of CH$_2$Cl$_2$ followed by the addition of 5 mL TFA. After TLC indicated complete boc removal, the solution was concentrated *in vacuo* followed by washing/evaporation with ether (10 x 50 mL) to afford 7 as a thick yellow oil which foams under vacuum (1.95g, 98%). ^{1}H NMR (400 MHz, DMSO-d$_6$) δ 7.90 (d, 2H, *J*= 7.6), 7.71 (m, 2H), 7.42 (t, 2H, *J*= 7.4), 7.33 (t, 2H, *J*=7.2), 5.91 (m, 1H), 5.33 (dd, 1H, *J*= 1.2, 1.6), 5.21 (dd, 1H, *J*= 1.4, 1.6), 4.58 (d, 2H, *J*= 5.2), 4.37-4.25 (m, 3H), 4.21 (t, 1H, *J*= 6.8), 2.79-2.74 (m, 2H), 1.71-1.66 (m, 2H), 1.62-1.51 (m, 2H), 1.39-1.33 (m, 2H); ^{13}C (400 MHz, CDCl$_3$) δ 172.1, 153.7, 143.7, 141.0, 131.3, 127.5, 126.8, 124.9, 120.7, 118.6, 64.7, 65.7, 53.6, 46.9, 39.8, 33.7, 31.7, 29.3, 23.3; HRMS (ESI) calculated for C$_{24}$H$_{28}$N$_2$O$_4$ [M+H]$^+$ 408.2049, found 409.4901.

3-[7-(2-tert-Butoxycarbonylamino-ethyl)-1,3,6,8-tetraoxo-3,6,7,8-tetrahydro-1H-benzo[lmn][3,8]phenanthrolin-2-yl]-propionic acid allyl ester (Boc-(CH$_2$)$_2$-NDI-(CH$_2$)$_2$-CO$_2$OAll) (4a). To a 100 ml round bottom flask was added 2 (1.25 g, 2.59 mmol), allyl bromide (20 ml, 148 mmol), and DIPEA (1.2 ml, 6.49 mmol). The flask was heated at 75-80 °C for 6 hours with stirring under an N$_2$ atmosphere. The solution was then cooled down to room temperature, followed by addition of 250 ml CHCl$_3$. The organic layer was washed by saturated NaHCO$_3$ (3 × 150 ml), brine (3 × 150 ml), dried (anhydrous Na$_2$SO$_4$) and concentrated *in vacuo*. The product was purified via column

71

chromatography using CH_2Cl_2/EtOAc (85:15) starting at a gradient of 5% EtOAc to afford 4 as a white solid (0.840 g, 55 %). ^{1}H NMR (400 MHz, $CDCl_3$) δ 8.73 (s, 4H), 5.87 (m, 1H), 5.31 (dq, 1H, J= 1.5, 1.5), 5.18 (dq, 1.5, 1.6), 4.59 (dt, 2H, J= 1.5, 1.4), 4.52 (t, 2H, J= 7.2), 4.36 (t, 2H, J= 5.6), 3.56 (t, 2H, 5.6), 2.81 (t, 2H, 7.4) 1.21 (s, 9H); [13]C (400 MHz, $CDCl_3$) 173.1, 159.3, 155.9, 139.6, 135.2, 132.1, 120.6, 118.2, 79.5, 65.9, 49.3, 37.9, 34.3, 33.0, 28.4;   HRMS (ESI) calculated for $C_{27}H_{27}N_3O_8$ [M+] 521.1798, found 521.8719.

Allyl 3-(7-(2-aminoethyl)-1,3,6,8-tetraoxo-7,8dihydrobenzo [3,8]phenanthrolin-2(1H,3H,6H)-yl)propanoate (NH$_2$-NDI-OAll) (4b). To a 50 mL round bottom flask was added 6 (0.840g, 1.61 mmol) which was dissolved in 10 mL of CH_2Cl_2 followed by the addition of 5 mL TFA . After TLC indicated complete boc removal, the solution was concentrated *in vacuo* followed by washing/evaporation with heptanes (3 x 25 mL) and dried under vacuum overnight to afford 6 as an off-white solid (0.715 g, 98%). ^{1}H NMR (400 MHz, $CDCl_3$) δ 8.73 (s, 4H), 5.91 (m, 1H), 5.31 (dq, 1H, J= 1.5, 1.5), 5.18 (dq, 1.5, 1.6), 4.57(d, 2H, J= 8), 4.26 (m, 4H), 2.76 (t, 2H, J= 8), 2.63 (t, 2H, J=8); [13]C (400 MHz, $CDCl_3$) 173.1, 159.3, 155.9, 139.6, 135.2, 132.1, 120.6, 118.2, 65.9, 49.3, 37.9, 34.3, 33.0; HRMS (ESI) calculated for $C_{22}H_{19}N_3O_6$ [M+H]$^+$ 421.1274, found 422.4028

CBI-Cys Synthesis (5)

Resin Loading. NovaSyn TGA resin (1.0 g, loading 0.28 mmol/g) was swollen with DMF for 30 min in a peptide reactor. DSC (717 mg, 10 equiv) and DMAP (34 mg, 1 equiv) in DMF (8 mL) were added to the resin and the reaction went on for 2 hr at room temperature with continuous mechanical shaking. The resin was washed with DMF (6x), followed by addition of a solution of Fmoc-Lys-OAll 5 (1.2 g, 10 equiv), DIPEA (0.975 mL, 20 equiv) in DMF (5 mL). After 6 hr of mechanical shaking the reaction was

drained, then washed with DMF (6x), DCM (4x), DMF (4x). The Fmoc protecting group was cleaved with 20% piperidine/DMF (2 x 10 mL x 15 min).

Cyclic Intercalator Synthesis   For amino acid coupling the conditions were 5 equiv of Fmoc-protected amino acid, 5 eq of HATU and 10 eq of DIPEA in 6 mL of DMF for 1 hr at room temperature.   The unreacted amino termini were capped with 5% (v/v) acetic anhydride-5% (v/v) 2,6-lutidine in NMP (20 min). 20% piperidine/DMF (2 x 10 mL x 15 min) was used to cleave off the Fmoc groups. Between every step, the resin was washed with DMF (6x), DCM (4x), and DMF (4x) successively. For the coupling of Fmoc-Cys(Trt)-NDI and NH_2-NDI-OAll abducts to the resin, NDI abduct (3 equiv), PyBOP (3 equiv), and HOBT (3 equiv) were dissolved in NMP (7 mL) completely. This solution and N-methylmorpholine (NMM, 6 equiv) were added to the resin and the coupling reaction proceeded for 50 min. After the solvent was drained, the resin was washed with NMP (6x) and the coupling was repeated. De-allylations were carried out by treating the resin with $Pd(PPh_3)_4$ (3 equiv) in $CHCl_3$/AcOH/NMM (v/v, 37:2:1) (15 mL/g of resin) under argon for 8 hr at room temperature.   The resin was washed with 0.5% (v/v) DIPEA/DMF, 0.5% (w/w) sodium diethyldithiocarbamate/DMF and again 0.5% (v/v) DIPEA/DMF followed by the usual DMF-DCM-DMF washes. The final cyclization was initiated by adding a solution of HOAT (5 equiv), PyBOP (5 equiv), and DIPEA (10 equiv) in 6 mL of NMP to the resin.   After 72 hr, the resin was negative to the bromophenol blue free amine test. Final cleavage of the cyclic product was performed with 95/2.5/2.5 TFA/triisopropyl silane (TIPS)/H_2) (v/v) for 3 hr. The TFA solution was concentrated to dryness, followed by addition of 10 mL of H_2O. The aqueous solution was washed three times with diethyl ether and lyophilized overnight. The crude product was dissolved in 0.1% TFA/H_2O and purified by reverse-phase preparative HPLC (Waters, C18 VYDAC HPLC column, (Cat. #218TP1022) using 0.1% TFA/water (v/v)

73

as solvent A and 0.1% TFA/AcCN (v/v) as solvent B. Two runs of purification were carried out to afford pure product. For the first run, a gradient of 5% B to 12% B over 1 min, followed by 12% B to 25% B over 43 min, and then 25% B to 95% B over 3 min. For the second run, a gradient of 5% B to 95% B over 60 min was applied. The product fractions were combined and lyophilized to yield CBI-Cys (8) (5 mg, 1.2 %) as an orange powder.
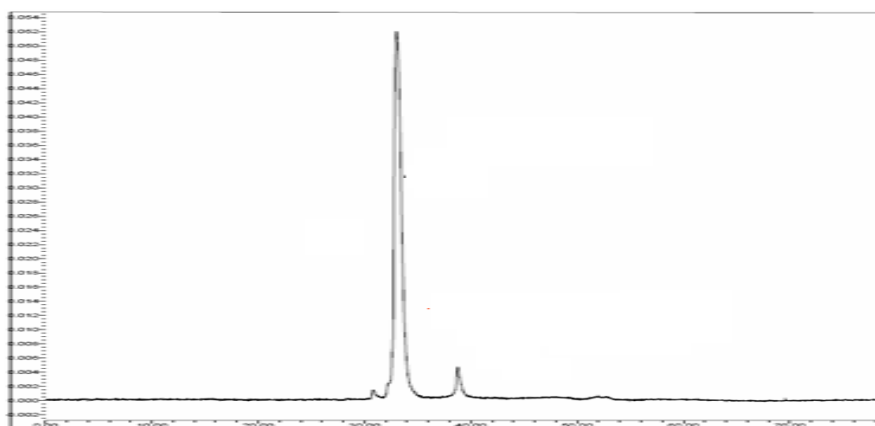
HPLC Profile of the purified CBI-Cys

HRMS (ESI) calculated for $C_{62}H_{68}N_{15}O_{18}S$ $[M+H]^+$ 1342.4580, found 1343.3575.

CBI-Cys•Au Conjugation. A freshly prepared solution of CBI-Cys in diH$_2$O (9.58 x 10^{-4} M) was prepared and analyzed via HPLC to assure that CBI-Cys was in its reduced form and was then placed in the freezer to prevent oxidation. Then, a 30 nmol vial of lyopholized maleimide functionalized gold nanoparticles (AuNP) from nanoprobes® was reconstituted with 2.1 ml of diH$_2$O and 0.2 mL of isopropanol to afford a nanoparticle solution of 1.304 x 10^{-5} M. This solution was vortexed several times over a five minute period. To this solution was added 600 uL of CBI-Cys to give a final reaction volume of 2.9 mL and final concentrations of 1.982 x 10^{-4} M CBI-Cys and 1.034 x 10^{-5} M AuNP

74

and led to a 19:1 ratio of intercalator to nanoparticle. The reaction solution was stirred for 40 hours. UV-Vis measurements were not taken prior to the dialysis. A 0.02 M phosphate buffer at pH 6.2 with 150 mM NaCl was prepared. This was the same as the buffer concentration of the conjugation solution. The approximate 3 mL reaction solution was dialyzed using a 3,500 MWCO unit and dialyzed three times for 3 hours using 500 mL of buffer each dialysis. Using Table 2.1 as a guide, this first measurement then corresponded to dialysis 1. The reaction was then dialyzed overnight (12h) against 600 ml of buffer and measured as dialysis 2. The solution was removed, added to a new dialysis membrane and a freshly prepared buffer solution was used. To the reaction solution, was added a 0.2% SDS solution to give a solution 0.5% SDS and dialyzed three times for 3 hours each using 500 mL of buffer for each dialysis and again was measured as dialysis 3. Finally, additional SDS was added and the reaction solution was dialyzed overnight (12h) and again measured as dialysis 4.

Chapter 3: Introduction to Controlled Nanoparticle Assembly Systems

3.1 DNA CONTROLLED NANOPARTICLE ASSEMBLY

Nanoparticles in the size range from 1 to 100 nanometers exhibit unique electronic properties between that of bulk material and the discrete electronic levels of an atom or molecule (Daniel 2004). The ordered assembly of uniform nanoparticles in one, two, or three dimensions exhibit delocalized electron states which depend on the strength of the electronic coupling between the adjacent nanoparticles and are related to the particle size, nature of stabilizing ligands, particle spacing, and packing symmetry. It is therefore a significant challenge to organize nanoparticles in one to three dimensions in order to study the electronic and optical coupling between the particles and to use these effects to design novel materials (Katz 2004).

There are many facets of nanoparticle assembly utilizing DNA as the scaffold. Nadrian Seeman, who is considered to be the founder of the DNA nanotechnology field, originally proposed the possibility of using DNA as a structural material for bottom-up self-assembly (Seeman 1982). Since then, various DNA architectures have been designed leading to 1D, 2D, and 3D DNA structures. Some have investigated the ability to use some of these DNA structures as organizational motifs for the assembly of gold nanoparticles. Other organizational motifs involve the design of DNA-nanoparticle conjugates which use DNA base-pairing rules to govern nanoparticle assembly and the assembly of nanoparticles directly onto a preassembled DNA double helix based on some supramolecular interaction. These types of nanoparticle assemblies have shown promising applications in the development of nanolectronic, bio sensing, and nanomechanical devices (Seeman 2007, Willner 2010).

3.2 DNA NANOARCHITECTURE

The DNA nanoarchitectures developed by Seeman are based on two distinct structural modification principles: DNA sticky ends and branched DNA (Figure 3.1) (Seeman 2003). Single-stranded DNA overhangs ("sticky ends") allow for the formation of dsDNA with precise organizational control. The sticky end interaction is a highly predictable structural motif because when two sticky ends anneal, they form classical B-DNA (Qiu 1997). The sticky ends are limited in that they can only form a dsDNA helix, which from a topological standpoint represents a straight line. In order to design more elaborate structures, branched junctions were used, based on the four-arm Holliday junction which is often an intermediate in genetic recombination (Holliday 1964). Combination of these branched junctions with the sticky end overhangs provided a tool set from which various organizational motifs could be constructed.

In order to provide increased rigidity to these DNA nanostructures, Seeman developed DNA tiles which were produced by designing DNA double-crossover (DX) motifs through single strand exchange. These motifs are held together by two stable crossovers, with the termini of each of the four helices having sticky ends. These sticky ends could be modified to create a code to control the assembly of various DX tiles, which provide the ability to design elaborate structures containing multiple DX tiles. (Winfree 2003). Various architectures have been designed which are beyond the scope of the experimental work to be presented here but nonetheless are important to point out as these initial developments were crucial towards the development of more complex triple crossovers (TX) and DNA origami (Nangreave 2010).
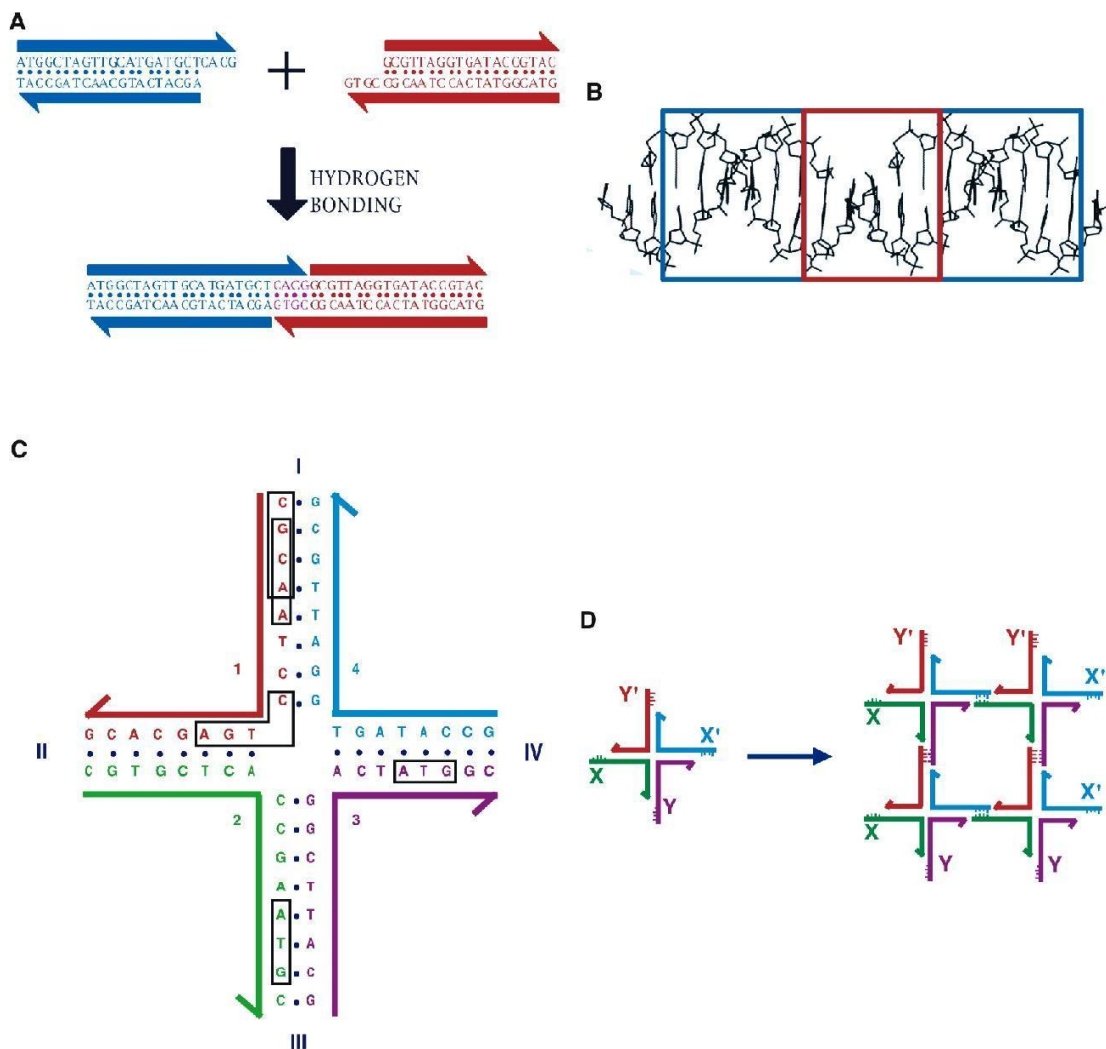
Figure 3.1 The Basics of Structural DNA Nanotechnology. (A) Sticky end cohesion. (B) Structure of a sticky end junction. (C) A stable branched junction. (D) Sticky-end assembly of multiple branched molecules. Reprinted from *Chemistry and Biology, 10*, At the crossroads of chemistry, biology, and materials: structural DNA nanotechnology, Seeman, N.C., 1151-1159, Copyright 2003, with permission from Elsevier.

3.3 NANOPARTICLE-DNA BASED ASSEMBLY

The initial work on DNA-based nanoparticle assemblies utilized the self-assembly of complimentary single strands (ss) of DNA (Mirkin 1996, Alivisatos 1996) (Figure 3.2). Mirkin utilized non-complementary ssDNA and modified them to incorporate a thiol, which allowed for conjugation to gold nanoparticles (AuNP). A DNA duplex with sticky ends complementary to the ssDNA-Au conjugates was then added into solution and formed macroscopic DNA-Au aggregates. This system was reversible and the assembly and disassembly could be controlled by changing the temperature. Alivisatos *et al*. used thiol modified ssDNA with several different sequences and conjugated them to 1.4nm gold nanoparticles (Nanoprobes®). By adding the respective complementary ssDNA, they were able to assemble the gold nanoparticles into various dimeric and trimeric conformations.

Another example utilized the strand complementarity of ssDNA conjugated to nanoparticles of two different sizes. By controlling the ratio of the various nanoparticle-ssDNA conjugates, different types of assemblies occurred and this was a good example of initial work which began investigating the ability to develop a binary assembly system (Mucic 1998). Using similar methodology, Niemeyer designed nanoparticles with multiple ssDNA components and termed these DNA AuNP's "D_n-Au", with n representing the number of ss oligos in the range of 2 to 7. The specificity from Watson-Crick base pairing allowed for the crosslinking of various NP architectures based on the varying complementary strands (Zou 2005).

One of the more elaborate examples utilizing complementary ssDNA was assisted by a unique means of purifying various ssDNA-Au conjugates through gel electrophoresis (Claridge 2005). By utilizing a branched DNA assembly methodology,

various trimeric and tetrameric structures were designed and the difference in structures allowed for a measurable change in electrophoresis mobility so that these structures could be isolated from the gel and subsequently imaged in the electron microscope (Figure x). Other more recent examples (Aldaye 2007) focused on constructing different shapes such as nanoparticle squares and triangles which could precisely control the geometric orientation of gold nanoparticles while Mastroianni utilized four different sized nanoparticles to form chiral nanostructures (Figure 3.3) (Mastroianni 2009)
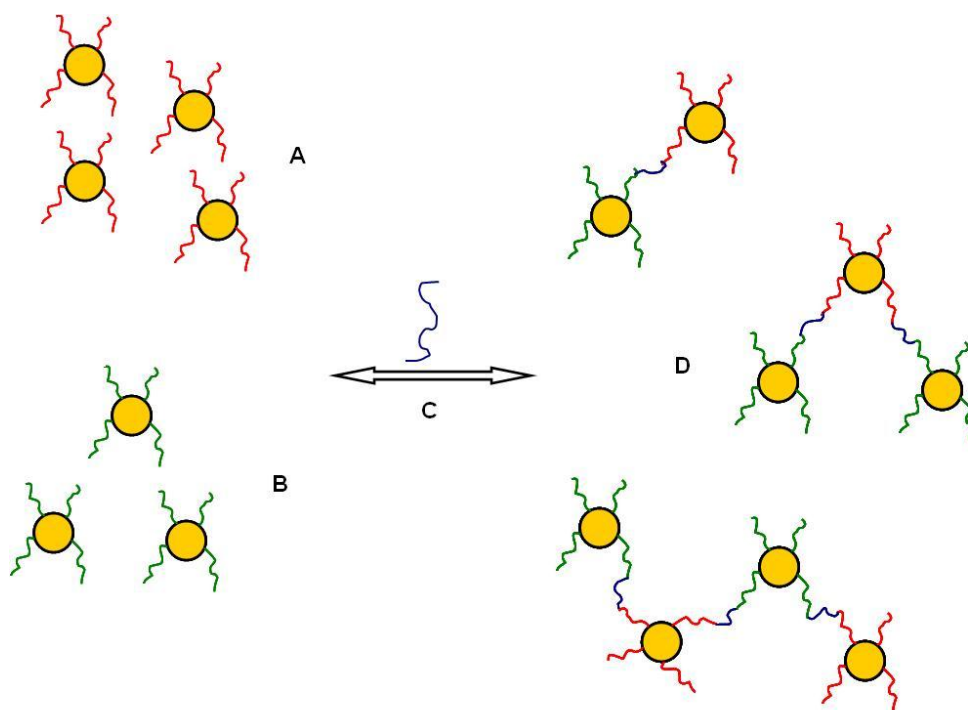
Figure 3.2. Early generation DNA-nanoparticle assembly system developed by Chad Mirkin. (A) contains gold nanoparticles modified with 3'-thiol-TACCGTTG-5' oligos and (B) modified with 3'-thiol-TTTCGTGA-5' oligos. (C) By heating and adding a linker duplex, (D) formation of various nanoparticle constructs is enabled. This system is also reversible.
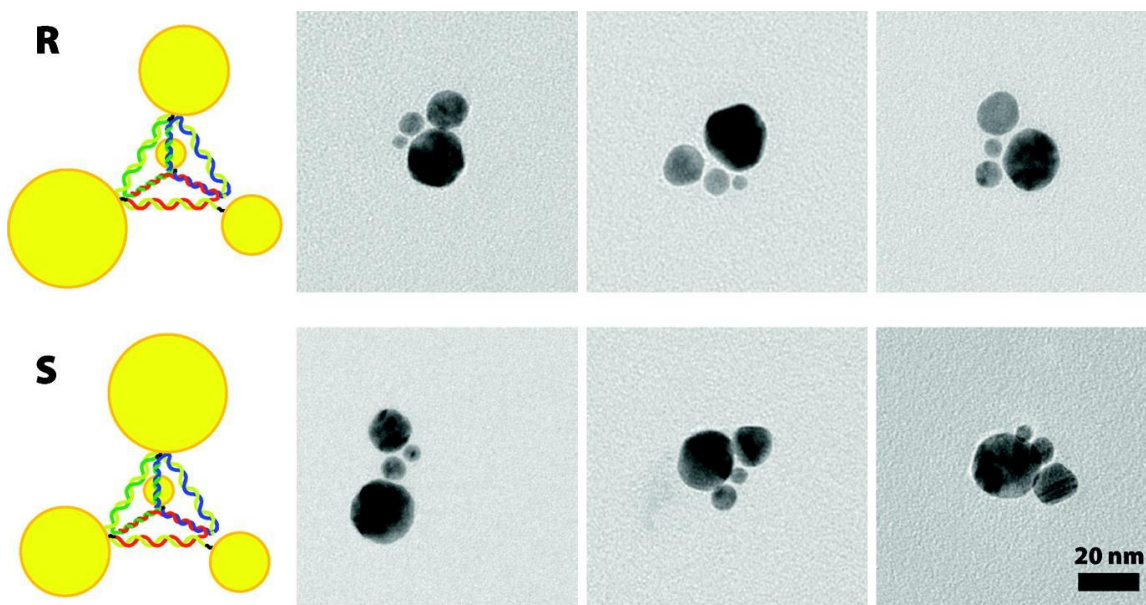
Figure 3.3. Examples of chiral pyramids. Reprinted from *J. Am. Chem. Soc., 10,*
Pyramidal and chiral groupings of gold nanocrystals assembled using DNA
scaffolds, Mastroianni, A.J., 8455-8459, Copyright 2009, with permission
from The American Chemical Society.

3.4 NANOPARTICLE ASSEMBLY DIRECTED ONTO DNA

An alternative method to using nanoparticle-DNA conjugates is to assemble the nanoparticles along a pre-assembled DNA construct. This is different in that it is not the strand complementarity of ssDNA that directs the placement of the nanoparticles but rather some indirect method which assembles the nanoparticles onto the preassembled DNA architecture, providing an alternative means for precisely controlling nanoparticle placement. The formation of 2D DNA structures designed by Seeman allowed for developments in this type of directed nanoparticle assembly.

One of the first developments utilized the formation of DNA tiles which contained a 15-base-pair adenosine ssDNA protruding from the assembled surface.

Nanoparticles were functionalized with a complementary 15-base-pair thymine single strand of DNA, added to these 2D DNA tiles, and were assembled onto the structure forming nanoparticle arrays with an average spacing of 12 to 25 nm between nanoparticles and 65 nm between nanoparticle rows (Le 2004). In an extension of this protocol, the same laboratory was able to again utilize similar DNA tiles, with the exception that the tiles contained two different single strands of DNA protruding from the tile. This allowed for the controlled patterning of two differently sized nanoparticles. Electron microscopy images clearly indicated two separate rows of nanoparticles containing 10 and 5 nm particles with very little cross contamination (Figure 3.4) (Zweng 2006). This last result was significant because it demonstrated the ability to organize a multi-component assembly onto a preassembled DNA architecture.
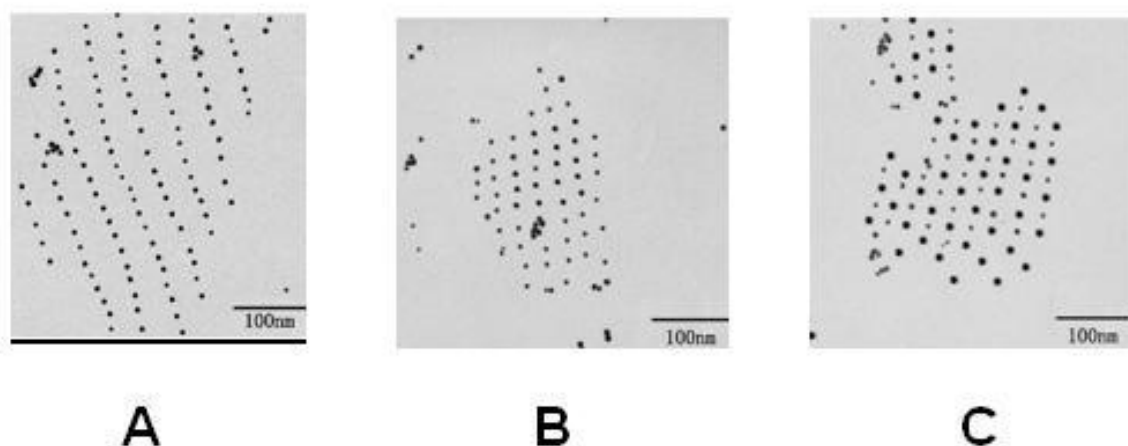
Figure 3.4. (A) and (B) represent two different sets of DNA tiles with 5 nm gold nanoparticles assembled onto them while (C) represents the use of both tiles to assemble 5 and 10 nm gold nanoparticles in alternating rows. Reprinted from *Nano Lett*, 6, Two-Dimensional nanoparticle arrays show the organizational power of robust DNA motifs, Zweng, J., 1502-1504, Copyright 2006, with permission from the American Chemical Society.

One of the most recent examples of nanoparticle assembly onto DNA investigated the 3D structure of an organized assembly (Figure 3.5) (Sharma 2009). Four DX DNA tiles were constructed with each having some unique structural feature. The central strand of tile A was conjugated with a thiol group and a 5-nm gold nanoparticle was then linked to that tile so that when assembled, the nanoparticles would be present on only one side of the tile. The C tile was altered by the addition of a stem loop which should organize opposite the nanoparticles in the array. By alternating both the addition/deletion of the stem loop with various nanoparticle sizes, different tubular arrays of nanoparticles were obtained. They also combined tiles which separately contained 5 and 10 nm gold nanoparticles on the A and C tiles respectively and used electron cryotomography to assess the structures from a 3D view. This was one of the first studies that utilized 3D analysis to further investigate the controlled assembly of gold nanoparticles and provide information on how one could potentially develop multicomponent systems in which various nanoparticle wires are controlled from a three dimensional point of view.
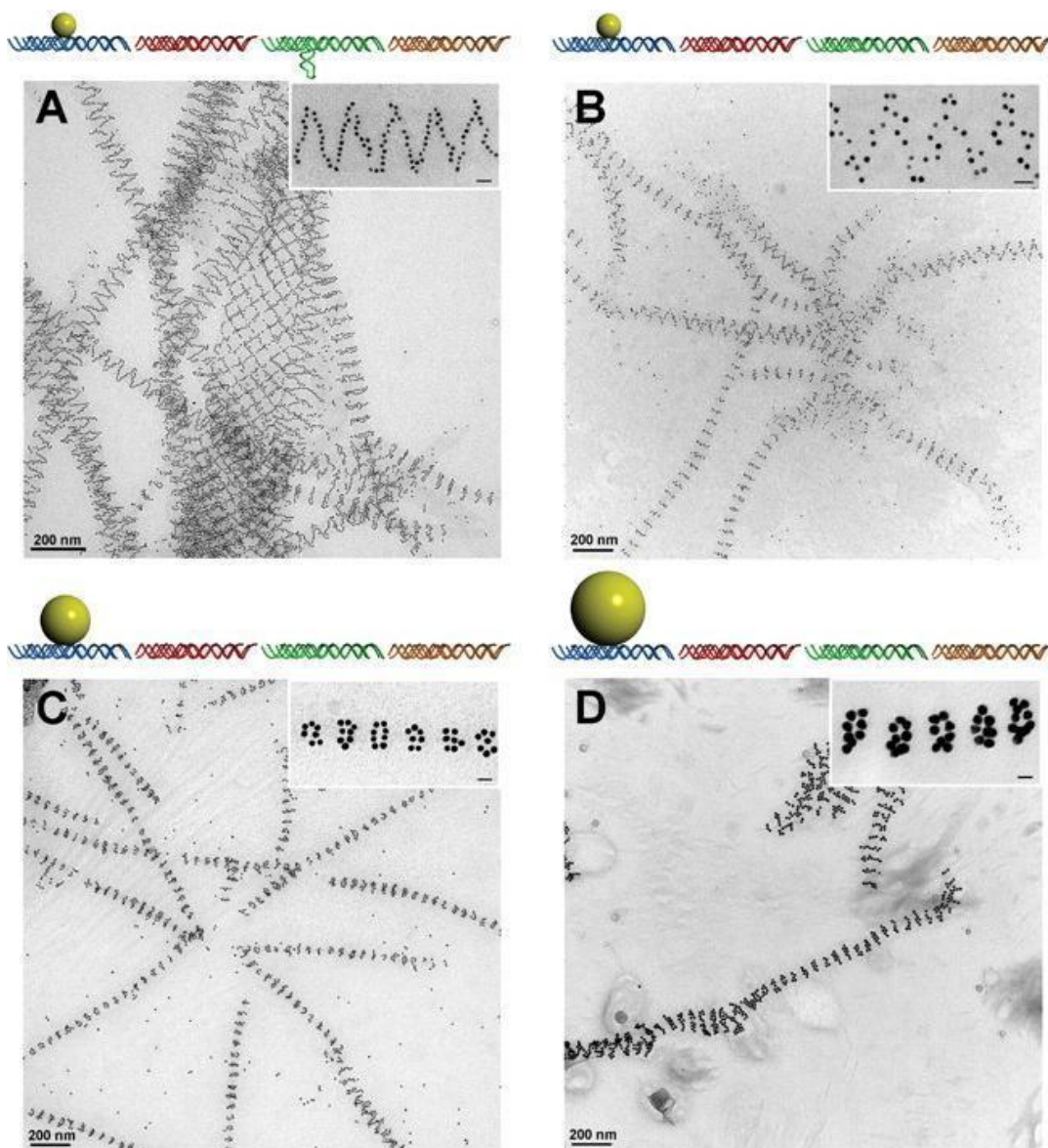
Figure 3.5. Formation of the different tube like architectures based on changes made to gold nanoparticles (AuNP) the A and C DNA tiles. (A) 5 nm AuNP on tile A and DNA stem loops on tile C. (B) 5 nm AuNP on tile A and no DNA stem loops on tile C. (C) 10 nm AuNP on tile A. (D) 15 nm AuNP on tile A. Reprinted from *Science*, 323, Control of self-assembly of DNA tubules through integration of gold nanoparticles, Sharma J., 112-116, Copyright 2009, with permission from The American Association for the Advancement of Science.

3.5 INDIRECTLY CONTROLLING THE ASSEMBLY OF GOLD NANOPARTICLES

Beyond using strand complementarity of DNA, there are two main methods used to organize nanoparticles onto DNA: immobilization of the nanoparticles at specific sites along the DNA, or direct metallization by the addition of nanoparticles followed by chemical reduction (Westerlund 2009). The main focus here will pertain to immobilization of nanoparticles using some type of specific interaction with dsDNA.

Some of the early work on directing the nanoparticle assembly onto DNA used the biotin-streptavidin interaction. The design of streptavidin-DNA hybrid molecules in combination with biotin functionalized gold nanoparticles led to the development of supramolecular aggregates labeled with gold clusters (Niemeyer 1998). Another example of the exploitation of this interaction combined the 2D DNA nanoarchitectures, specifically the DNA triple crossover molecule (TX), with the avidin-biotin interaction. The TX tiles were designed to incorporate biotin molecules and after their formation, were mixed with streptavidin functionalized gold nanoparticles. The nanoparticles were organized into two types of arrays, with an approximate spacing of 17 nm between each nanoparticle (Park 2004). These two examples show the versatility of the avidin-biotin interaction for the controlled assembly of gold nanoparticles, as the nanoparticles could be conjugated to either avidin or biotin and the same for the DNA architecture.

Electrostatic interactions between positively charged nanoparticles and the negatively charged backbone of DNA are sometimes exploited to assemble gold nanoparticles. In a unique example, small 1.5 nm gold nanoparticles were organized by designing positively charged ligands and coating the nanoparticles. The thickness of the ligand shell was altered to lead to various constructs with precise control over nanoparticle spacing in the range of 1.5 to 2.8 nm (Figure 3.6). This showed the ability to reproducibly generate evenly-spaced nanoparticle chains with a significant degree of

85

control over nanoparticle spacing by controlling the chemical features of the nanoparticles (Woehrle 2004).
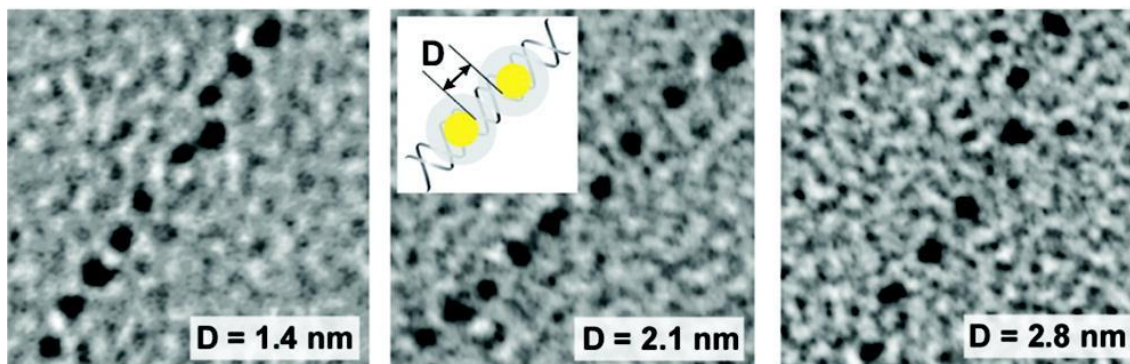
Figure 3.6. Varying ligand compositions led to nanoparticle assemblies with various spacing's. D is the distance between gold nanoparticles. The DNA is not directly visualized. Reprinted from *Langmuir,* 20, One-Dimensional Nanostructure Assemblies Formed by Biomolecular Nanolithography, Woehrle, G.H., 5982-5988, Copyright 2004, with permission from The American Chemical Society.

Another assembly motif involves the use of synthetic peptides to organize gold nanoparticles. The recombinant peptide 17H6 is expressed from *E. coli* and its assembled structure is highly dependent on its microenvironment (Top 2008). At an acidic pH, it is assembled into linear fibril structures containing an antiparallel β-sheet arrangement of alanine-rich repeats and contains some positively-charged histidine patches (Sawaya 2007). When this peptide was mixed with negatively-charged gold nanoparticles, they became assembled in a manner that followed the spacing from the positive histidine patches on the peptide fibrils. This provided a system in which negatively charged nanoparticles could be organized based on the structural motif of a peptide containing positively charged properties (Sharma Angew. Chem. Int. Ed. 48, 7078). Another example again utilized DNA tiles which incorporated a peptide (WALRRSIRRQSY) identified from a combinatorial library as a high-affinity gold

labeling peptide (Hnilova 2008). The addition of gold nanoparticles, which recognized the peptide, led to the assembly of these nanoparticles onto the DNA tiles. This study represented the first example that combines DNA-based self-assembly and peptide molecular recognition elements to demonstrate the controlled assembly of gold nanoparticles (Carter 2010).

Chapter 4: Progress towards the Development of a Controlled Nanoparticle Assembly System via Sequence Specific Bis-Intercalators with DNA as the Scaffold

4.1 GOAL AND PURPOSE

Synthetic modification of a sequence-specific DNA *bis*-intercalator to allow for conjugation of a gold nanoparticle is the first step toward developing an intercalator based nanoparticle assembly system (Figure 4.1). It is then necessary to visualize the assembled nanoparticles on the DNA, although it is not an absolute requirement to visualize the DNA itself. This study can simultaneously validate our previous experiments with the cyclic *bis*-intercalator, showing that it would be possible to use these nanoparticles to probe the mechanism by which a more complex intercalator locates its preferred sequence.
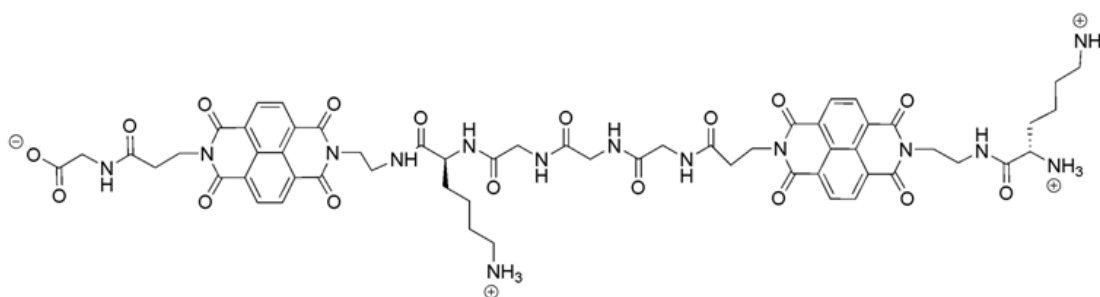
G₃K *bis*-intercalator that binds 5'-GGTACC-3'

Figure 4.1 G$_3$K *bis*-Intercalator

4.2 INTRODUCTION

DNA is the ultimate example in nature of a self-assembly system that relies on well-defined rules for association. Watson-Crick base pairing allows for the formation of

known structures based on complementary single-stranded DNA, and the power of DNA as a molecular tool is enhanced by scientists' abilities to synthesize a wide range of DNA sequences and to amplify these sequences using standard techniques such as Polymerase Chain Reaction (PCR). DNA also displays relatively high physiochemical stability and can be utilized to form multi-component structures based on branched junctions and sticky ends as previously discussed. The ability to precisely control the placement of various types of nanoparticles offers the ability to develop novel materials that may have unique electronic properties.

Because the spacing between nanoparticles plays an important role in utilizing their electronic properties, systems that allow for the precise placement of nanoparticles of varying sizes and compositions would offer the most promising means of developing useful materials. The site specific attachment of DNA binding molecules could provide a useful template to organize nanoparticles. If such a system can offer multiple binding specificities, it would be possible to organize precisely nanoparticles that differ in their properties. The intercalation mode of binding has been scarcely used with regard to controlling the assembly of nanoparticles.

There are some examples that utilize intercalators to assemble nanoparticles onto DNA, but these intercalators lack sequence specificity. The metal complex Cisplatin binds strongly to GpG steps in DNA and was used to assemble nanoparticles 2-4 nm in diameter onto plasmid DNA. The AFM images showed the nanoparticles were directed onto the DNA only in the presence of the metal complex; however there was not any specific control over nanoparticle spacing (Nyoyong 2002). Psoralen, a DNA-binding molecule which intercalates into ApT steps in DNA, was also used to direct nanoparticle assembly by conjugating the intercalator to 1.4 nm gold nanoparticles from Nanoprobes®. After being irradiated with UV light (>360 nm), the psoralen undergoes a

photo-induced cycloaddition with the thymine residues and leads to the covalent attachment of the intercalator to DNA (Patolsky 2002). Again, there is no direct sequence specificity other than being directed towards AT-rich regions of the DNA, although the covalent attachment of the psoralen does offer a very strong interaction due to the covalent attachment. Another example utilizes nanoparticles coated with a monolayer of ethidium bromide which was modified to contain a thiol that readily exchanged with the phosphine-stabilized gold nanoparticles (Figure 4.2). This led to random attachment of the nanoparticles to plasmid and linear DNA (Murray 2002). Another interesting example used a ruthenium dipyridophenazine intercalating moiety and incorporated a biotin molecule onto the intercalator. After incubation with short strands of DNA (80 base pairs), the addition of streptavidin-functionalized gold nanoparticles (10 nm) led to the formation of nanoparticle dimers and trimers. The nanoparticle spacing was relatively consistent from examination of TEM images, although the short strands of DNA likely dictated the limitation of at most 3 nanoparticles per strand (Slim 2007).

The bis-intercalators developed in our laboratory would offer a novel opportunity to explore the assembly of gold nanoparticles that would be directed based on the intercalator's sequence specificities. Each intercalator binds a different sequence of DNA and also places its peptide linker into different grooves. A long term application may revolve around this groove placement and could allow for the development of a system that intricately controls the 3D placement of gold nanoparticles by having various nanoparticles protrude out of the minor and or major grooves of the DNA. It would be prudent to employ one *bis*-intercalator and use the initial experiments to develop a modular protocol which can then be employed with the second bis-intercalator. A multifaceted system, in which molecules binding different DNA sequences are utilized to

90

assemble nanoparticles should have important implications for the precise control of any type of nanoparticle system in which a unique property could be measured. This chapter should serve as a protocol for the development of a nanoparticle assembly system which can be used for any DNA intercalator which binds a specific sequence of DNA.
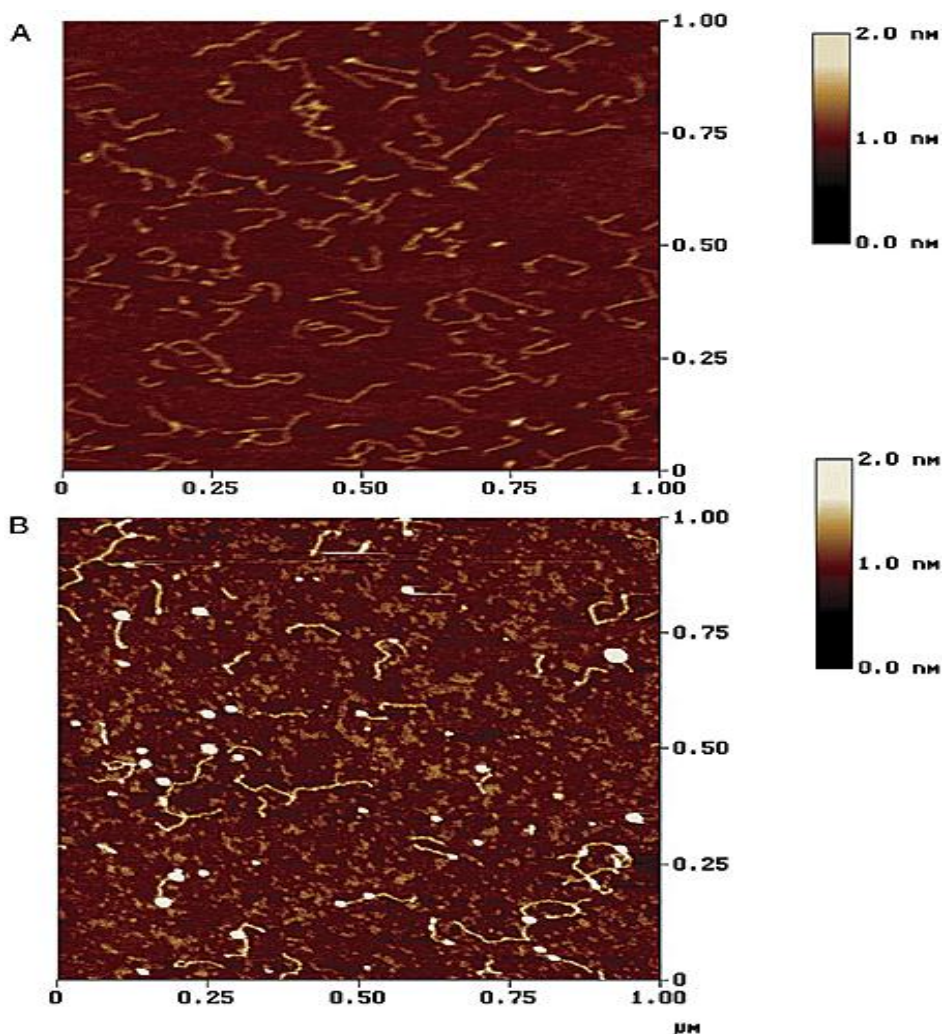
Figure 4.2. AFM images of (A) DNA alone and (B) DNA incubated with the nanoparticles coated with ethidium bromide. The large white dots are the nanoparticles, but the spacing and organization is not controlled. Reprinted from *Analytical Chemistry,* 74, DNA binding of an ethidium intercalator attached to monolayer-protected gold cluster, Murray, R.W., 7320-7327, Copyright 1997, with permission from The American Chemical Society.

4.3 EXPERIMENTAL DESIGN

The previously characterized G_3K bis-intercalator will be used in the first generation development of the nanoparticle assembly system. The first step in the development of this system is to determine an appropriate nanoparticle placement that will not affect the binding specificity. The initial design will incorporate the cysteine on the peptide linker as was done with the cyclic bis-intercalator utilizing the previously designed NDI-cysteine monomer **2**. The solid phase synthesis will utilize a rink amide resin and follow the basic design shown in Figure 4.3.

1st coupling   **2nd coupling**

6

3rd coupling   **4th coupling**
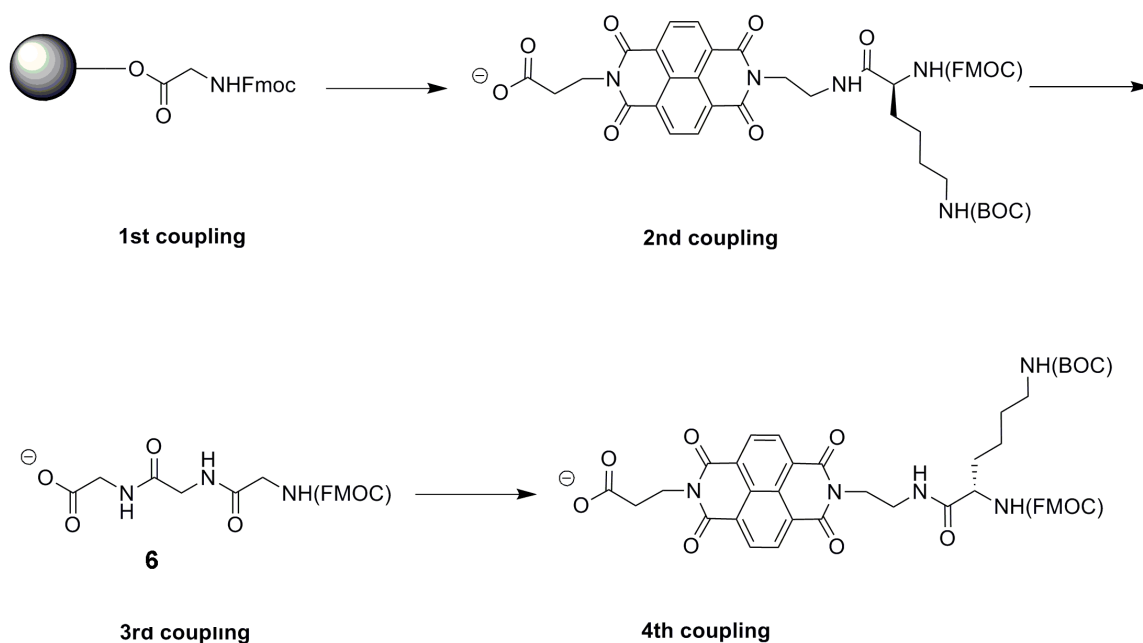
Figure 4.3. Schematic of peptide synthesis protocol. A glycine amino acid is coupled, followed by the NDI-cysteine monomer, then a tri-glycine analog, and finally a NDI-lysine monomer.

Additionally, it is necessary to design a DNA fragment containing multiple binding sites. An approximately 500-base pair double-stranded DNA fragment was designed by Crystal Flowers using standard DNA synthesis protocols that utilized primers containing multiple G_3K binding sites. These primers were annealed, amplified, purified, cut, and again purified prior to ligation into a pMoPac16 plasmid vector, which was previously cut at two SfiI sites. These plasmids were grown in cells, removed, and purified to yield plasmid DNA containing the 500 bp fragment with 26 binding sites spaced 10 base pairs apart (Figure 4.4).
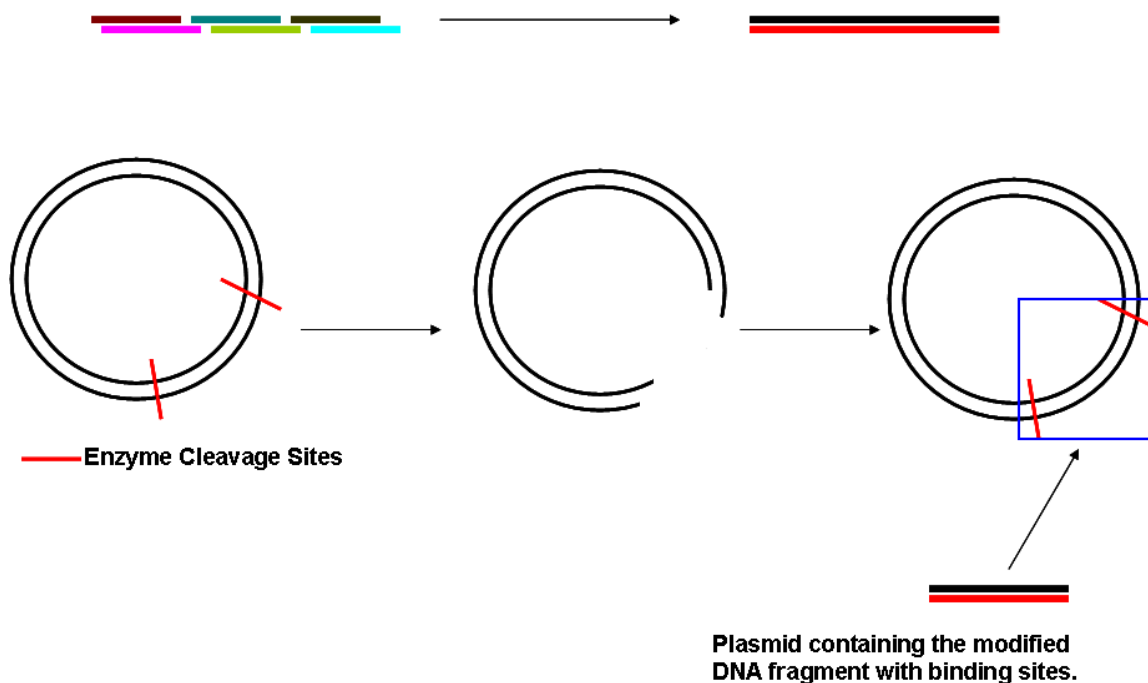
Figure 4.4 Schematic of DNA synthesis.

The versatility of such a design is that either the plasmid DNA or smaller 500 bp insert can be used to examine the nanoparticle assembly, allowing for increased flexibility when developing the microscopy protocols. Using Figure 4.5 as a guide, one can envision how the controlled assembly of the nanoparticles can be investigated. In an

optimal scenario, nanoparticles that are not incubated with DNA will show a random organization, while the nanoparticle-intercalator conjugates incubated with DNA will directly assemble onto the DNA strands in patterns defined by the binding site spacing.

Conjugates without modified DNA   Conjugates with modified DNA
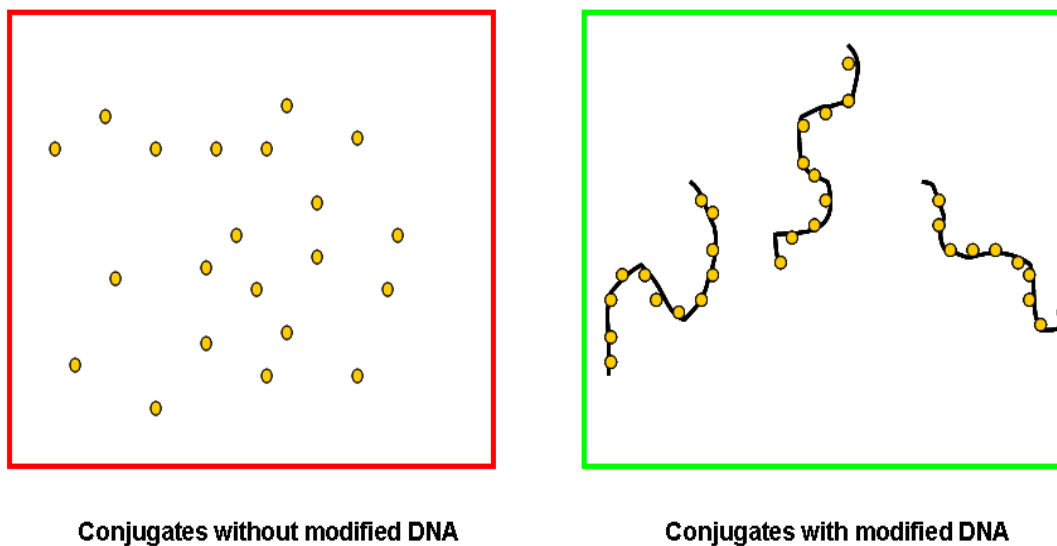
Figure 4.5 Simplistic models showing the drastic difference between random assembly and controlled assembly.

4.4 SUMMARY OF RESULTS

Once a gold nanoparticle was conjugated to the modified G_3K bisintercalator (Figure 4.6), the electron microscopy studies were not conclusive in showing the assembled nanoparticles (Figures 4.8 and 4.9). This led to the design of a gel shift assay that indicated the placement of the nanoparticle directly onto the peptide linker was inhibiting DNA binding (Figure 4.11). This required the design of two new analogues (Figure 4.12) that differed in nanoparticle placement and were shown to successfully bind to DNA (Figure 4.18).

The electron microscopy studies were unable to show the assembly of gold nanoparticles (Figures 4.19 and 4.20). This led to the use of Atomic Force Microscopy to

attempt to visualize the DNA, which should lead to a more conclusive study of the nanoparticle assembly. Large plasmid DNA was successfully imaged (Figure 4.26) using a non-salt based method. It was not immediately apparent if this same methodology was successful in visualizing the smaller DNA fragments (Figure 27).

4.5 SYNTHESIS OF BIS C•AU

4.5.1 Results

The modified NDI-cysteine amino acid used in the SPPS of the cyclic bis-intercalator was used for the SPPS of Bis C (Figure 4.6). A rink amide resin was used as the solid support and the first glycine residue was coupled, followed by addition of the cysteine modified NDI amino acid. After which, a tri-glycine analog was prepared in solution and coupled after the NDI-cysteine, followed by the addition of a lysine modified NDI amino acid and final cleavage from the resin to give the modified intercalator Bis C. The product was purified by HPLC and both the reduced and oxidized forms were identified using similar protocols for the cyclic bis-intercalator. The gold nanoparticle was successfully conjugated to the intercalator, purified via dialysis, and characterized using UV-Vis spectroscopy (Figure 4.7, Table 1).

7
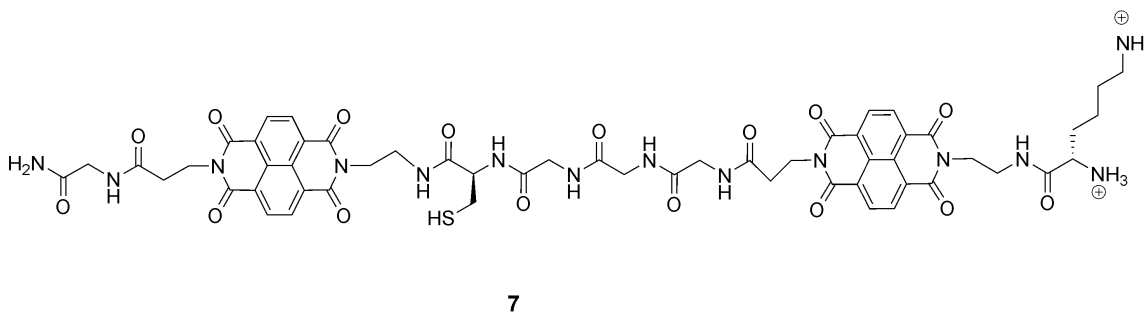
Figure 4.6. Structure of Bis C with a lysine residue substituted by cysteine which can be conjugated to the maleimide functional group of the gold nanoparticle.

4.5.2 Discussion

Since the cysteine residue was replacing one of the lysines of the original G_3K, it was important to maintain an overall +2 charge on the molecule. This was achieved by using the rink amide resin which removes the carboxylic acid terminus. The synthesis of an Fmoc protected tri-glycine shortened the number of solid phase synthesis steps and reduced the overall time required for solid phase synthesis. As previously discussed, it was important to identify the oxidized product prior to conjugation with the gold nanoparticle and this was achieved after the initial purification of Bis C by HPLC.

It was previously shown that an excess of thiol led to ligand exchange with the phosphorous based ligands on the nanoparticles. This new reaction used closer to an initial 1:1 ratio of intercalator and nanoparticle. As the UV-Vis studies showed (Figure 4.7, Table 1), this change avoided the ligand exchange that had occurred previously. One could argue that it is not possible to determine without absolute certainty that each nanoparticle contains only one DNA intercalator. However, this type of analysis via UV-Vis goes beyond the traditional characterization methods for studies using these gold nanoparticles. (Shipley 2000 and Heppelmann 1999).
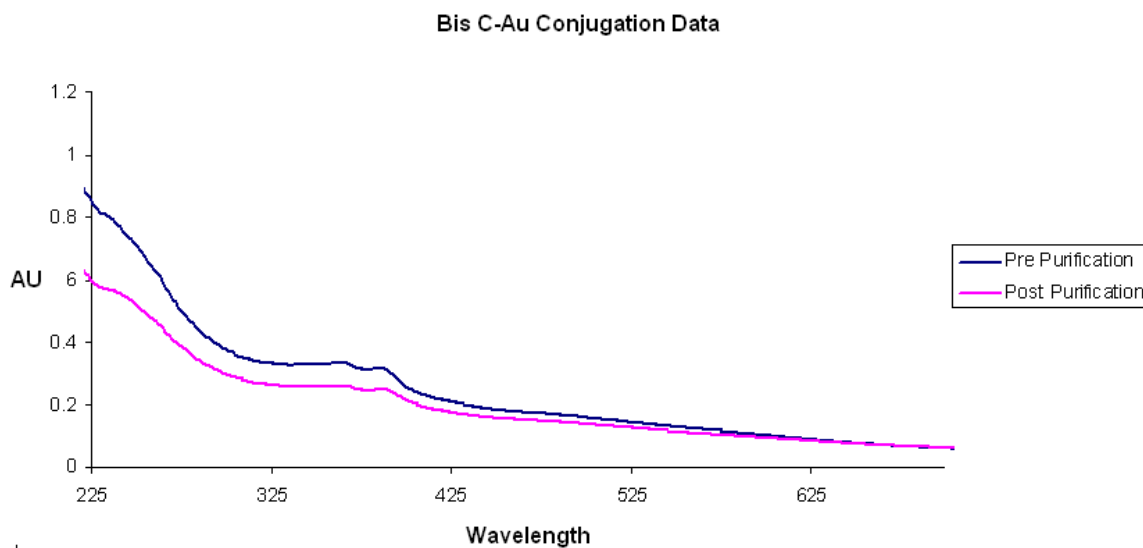
Figure 4.7 UV-Vis data of BisC•Au synthesis pre and post dialysis.

Step	420	385	Abs at 385 of Bis KC	Au (M)	Bis KC (M)	Bis KC to Au Ratio
Pre Dialysis	0.2138	0.3169	0.05178	1.371×10^{-6}	1.889×10^{-6}	1.38
Post Dialysis	0.1802	0.2487	0.02523	1.155×10^{-6}	9.208×10^{-7}	0.79

Table 4.1 Summary of data for Bis C conjugation to AuNP.

4.6 ELECTRON MICROSCOPY OF NANOPARTICLE ASSEMBLY

4.6.1 Results

Initial results did not show the assembly of gold nanoparticles using Bis C•Au and the modified DNA fragments. Various concentrations of both DNA and Bis C•Au were used and all results were similar (Figures 4.8 and 4.9).

97

4.6.2 Discussion

Since appropriate conditions were not determined to visualize individual DNA strands, it was reasoned that appropriate controls could be used that would not require actually seeing the DNA itself in order to establish that the nanoparticles were being assembled. The intercalator-functionalized nanoparticles were added to a control grid without the presence of the modified DNA containing the multiple binding sites and were then added to another incubation containing the modified DNA. These two solutions were compared to each other and there should have been a considerable difference between both incubation images.

Unfortunately, the initial experiments failed to show any discernable difference between the control and experimental images (Figure 4.8 and 4.9, A and B). Initially, it was thought that the DNA may not have been consistently absorbing to the sample grid surface. Both carbon and formvar grids were used and each had inconsistent results. Therefore, a poly-L-lysine coating was used to provide a positively charged surface, which should provide a consistent surface to which the DNA should absorb. However, this modification did not lead to any significant changes in the assembly of the nanoparticles (C and D). It was now apparent that there may be something beyond the microscopy that was not allowing the nanoparticles to assemble in a controlled manner. It is also important to note that while only eight images are shown here, there were approximately 1000 pictures taken using various combinations of conjugate and DNA concentrations. The images depicted here are representative of the inconsistencies seen between various experiments and the inability to decipher significant differences between control and experimental images.
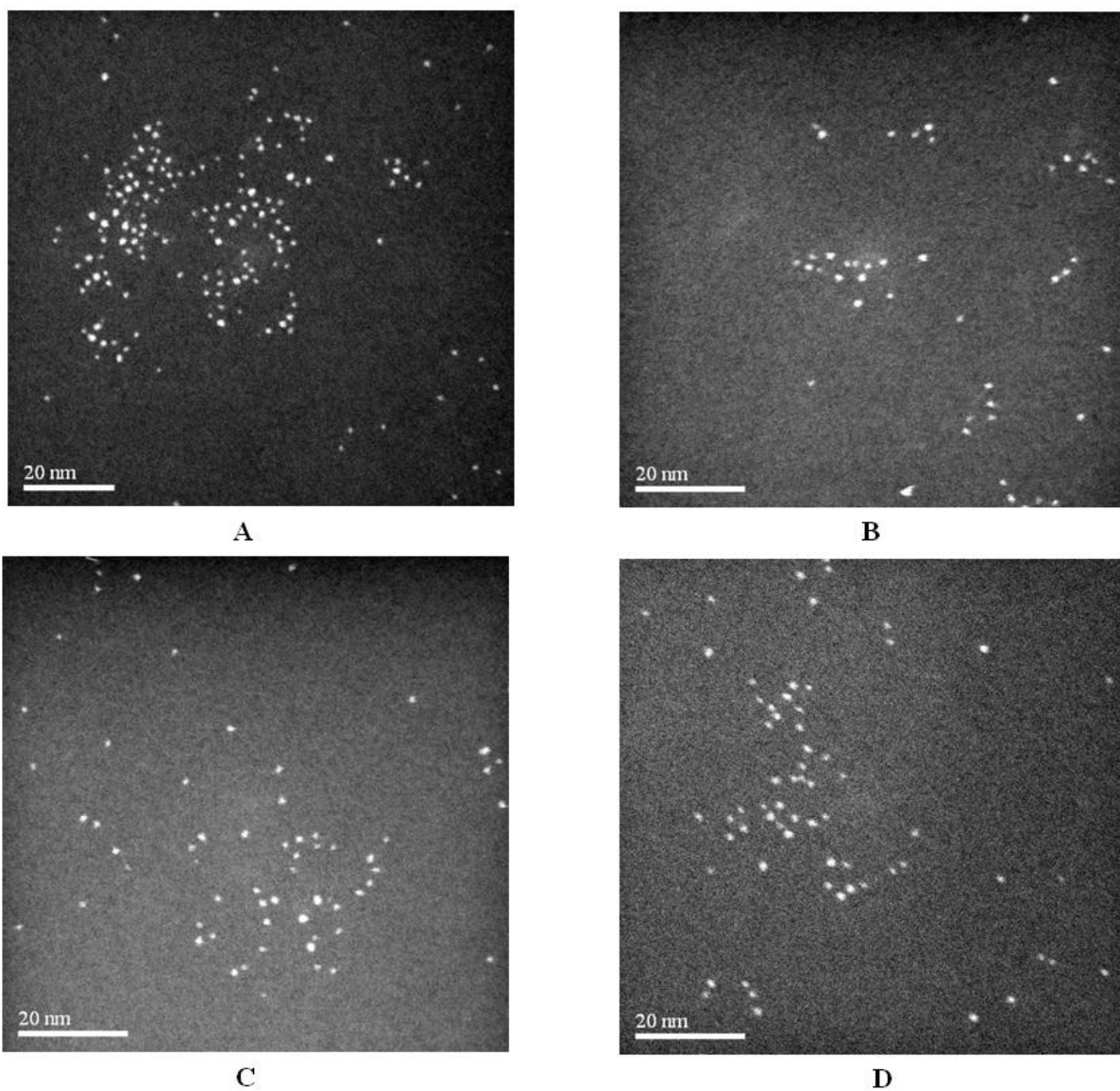
Figure 4.8. Various concentrations represented in A-D of the intercalator functionalized
Au nanoparticles without the binding site DNA present.
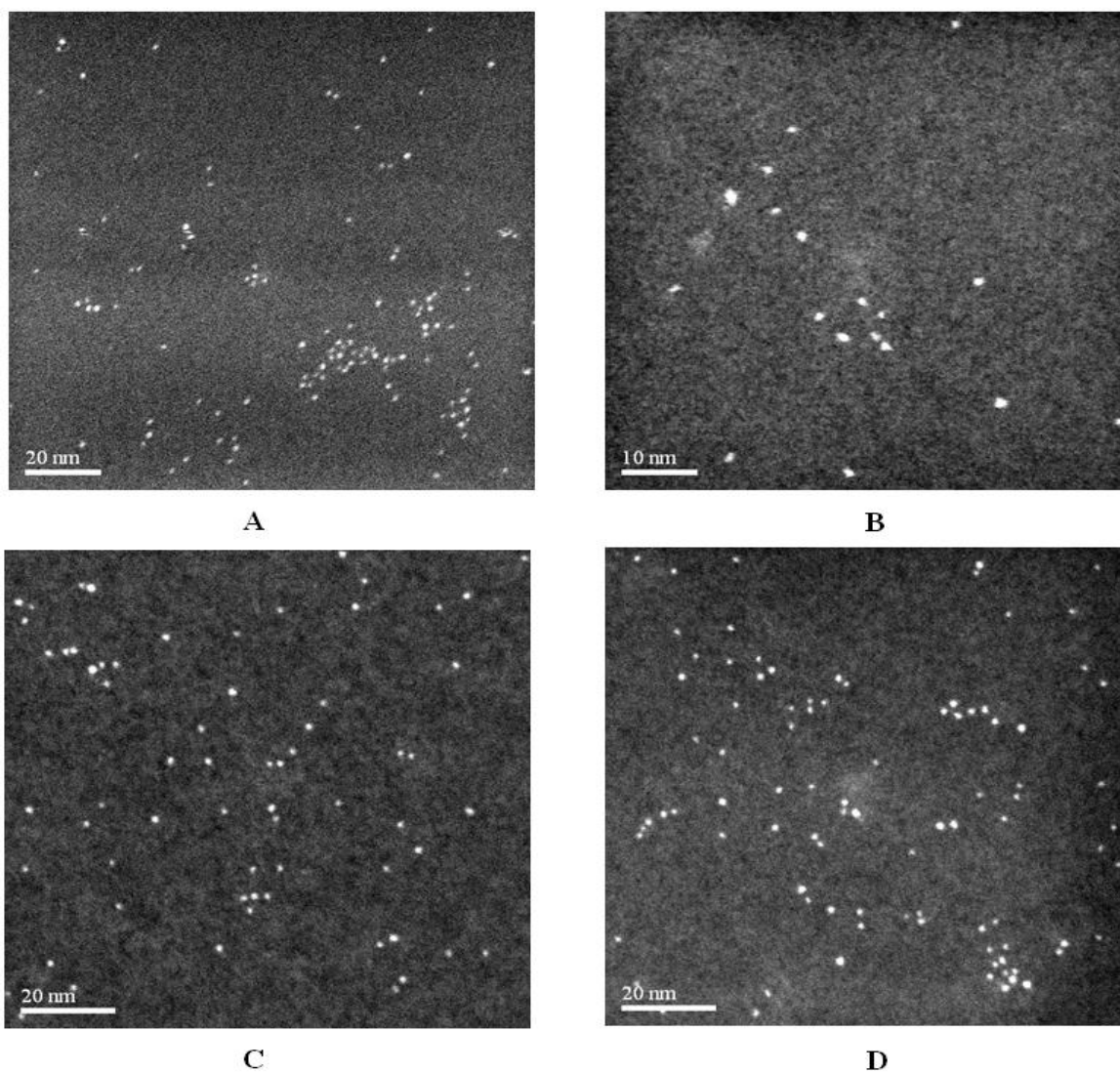
Figure 4.9 Concentrations of the intercalator functionalized nanoparticles are exactly the same as the pictures from figure 3.8 and these incubations included the binding site DNA. There is no clear nanoparticle assembly and all images are representative samples of hundreds of images.

100

4.7 GEL SHIFT ASSAY TO ASSESS DNA BINDING

4.7.1 Results

A gel-shift assay was developed to assess whether or not the Bis C•Au conjugate was binding the DNA and initial gel results were inconclusive (Figure 4.10). A new gel was run using the original G_3K as a control (Figure 4.11) and it was determined that the nanoparticle was inhibiting binding.
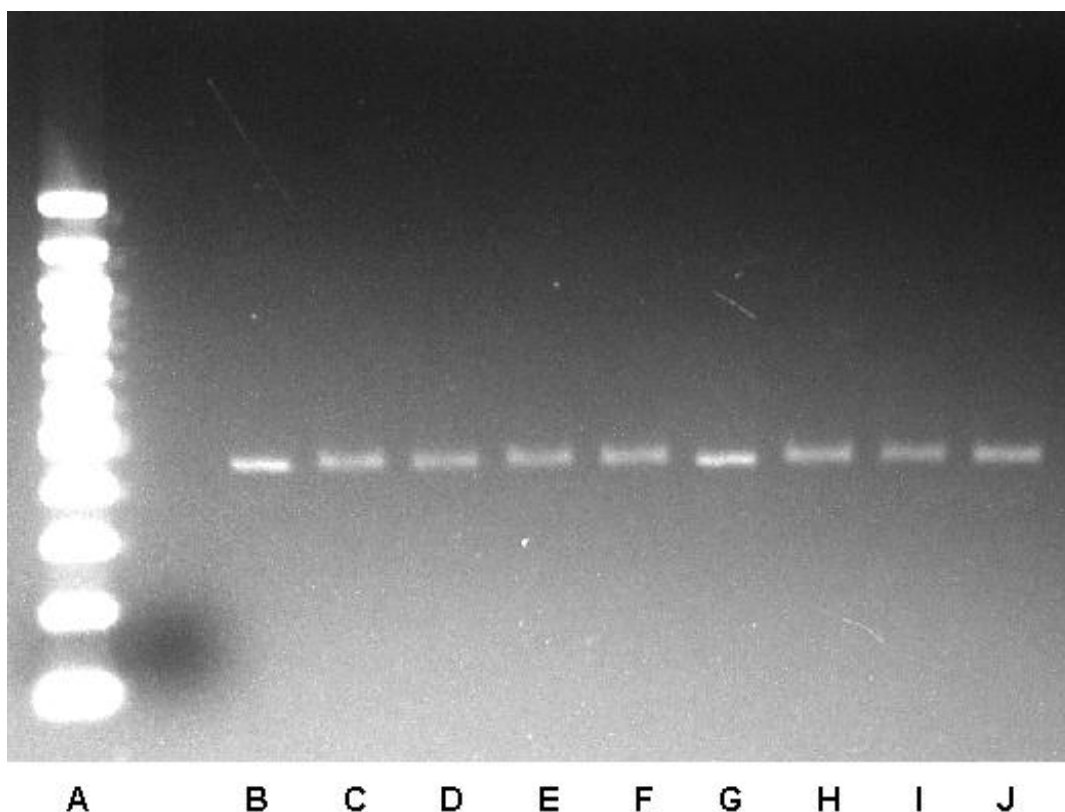
Figure 4.10 Initial Gel studies which do not clearly identify a gel shift. All final DNA concentrations are 169 nM and 624 nM Bis C•Au conjugate. Lane A represents a 100bp ladder. Lanes B and G represent DNA control lanes without any conjugate. Lane C,D,E, F,H,I,J represent varying incubation times at 4, 8, 16, 24, 36, 48, and 72 hours respectively.
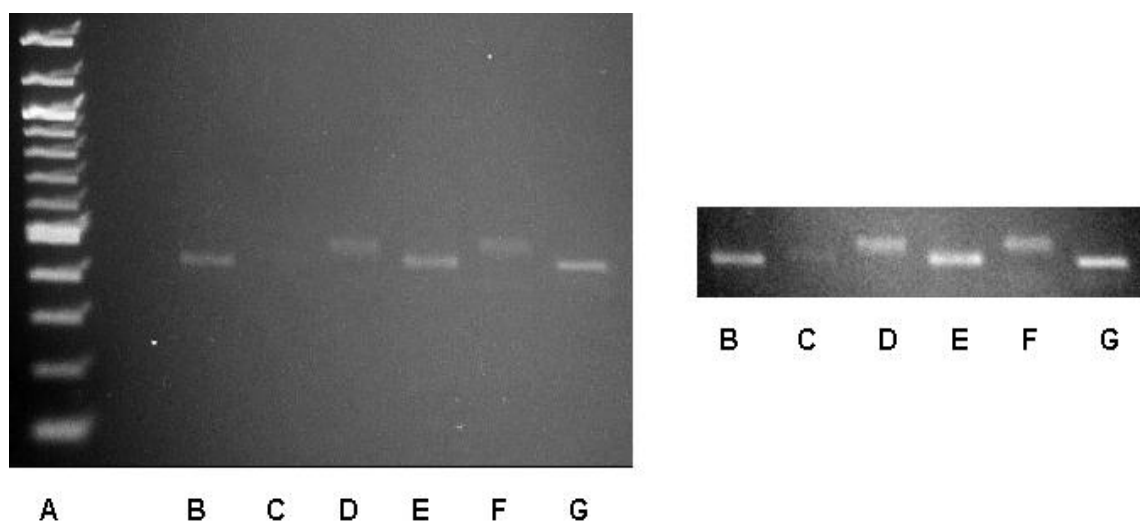
Figure 4.11 Gel shift assay with the G₃K control (Lanes D and F), clearly identifying a lack of a gel shift with respect to the Bis C•Au conjugate. Lanes D and F represent DNA incubated with G₃K. Lanes B and C represent two different concentrations of conjugate incubated with DNA. Lanes E and G represent control DNA, both without any intercalator present.

4.7.2 Discussion

Since DNA will move differently through a gel matrix depending on its size, charge, and conformation, a bound protein or molecule can slow the movement of DNA through the gel matrix. The DNA of interest is 500 base pairs in length and therefore agarose gel electrophoresis is a suitable gel matrix to be used. The initial gels were inconclusive as it was difficult to ascertain if there was a difference in mobility between control lanes and incubation lanes.

The G₃K control was used to show what the anticipated gel shift should look like, since this bis-intercalator has been extensively characterized by both NMR structural studies and DNAseI footprinting. It was fairly obvious with this control that the first

generation conjugate was not binding to the DNA (Figure 11) as there was a substantial gel shift seen with the G_3K control lane. The shift caused by G_3K likely represents the maximum binding that could be achieved for the nanoparticle-intercalator species and future analogues should be targeted to achieve this same gel shift. The G_3K was incubated with the DNA in both water and phosphate buffer and both shifted in a similar manner. This is significant because the conjugation occurs in phosphate buffer and it is important to verify that this does not interfere with binding.

4.8 DESIGN AND ANALYSIS OF SECOND GENERATION CONJUGATES

4.8.1 Results

Two new analogues were designed and synthesized (Figure 4.12) and conjugated to gold nanoparticles in the same fashion as the first analogue (Figure 4.15, Table 2). The dialysis purification protocol was further established through two control experiments (Figures 4.16 and 4.17 and Tables 3 and 4) and the gel shift assay confirmed that the analogue with the nanoparticle conjugated to the *N*-terminus was able to bind to the modified DNA (Figure 4.18).
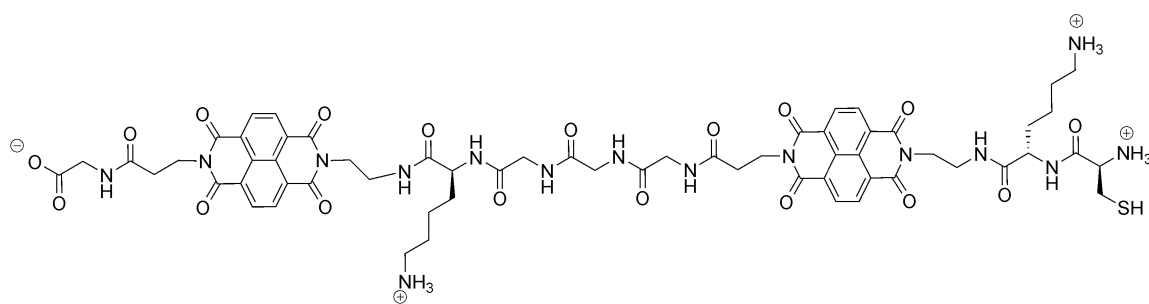
Bis KC

8
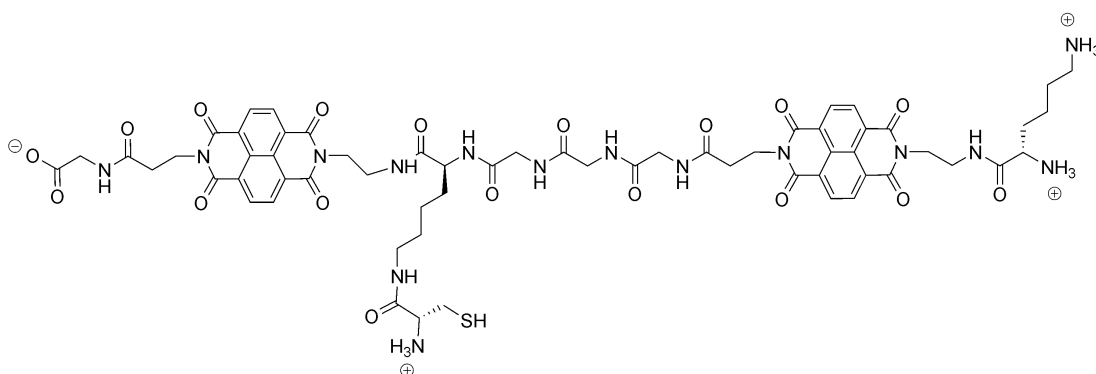
Bis C extend

9

Figure 4.12 Two new analogues with the cysteine residue placed on the N terminus (Bis KC) and extended from the peptide linker (Bis C extend).

4.8.2 Discussion

The same solid phase scheme used for the Bis C analogue was followed. For the Bis KC synthesis, a trityl protected cysteine residue was incorporated in the last coupling step. For the Bis C extend analogue, the idea was to extend the cysteine residue off the peptide linker. The first synthesis attempt utilized an allyl protecting group on the lysine that was removed using a palladium catalyst to allow for the final coupling of the cysteine amino acid to the lysine side chain. However, LC-MS data showed the major product was the original G_3K and no mass was present which would have indicated the

presence of the Bis C extend analogue. This meant that the cysteine coupling did not work and was likely due to the sterics of an internal reaction on the solid phase resin. Therefore, a new lysine-cysteine NDI monomer was synthesized in solution (Figure 4.14), and this was incorporated in one step on the solid phase resin and the molecule was successfully synthesized.

This internal coupling did not occur to any measurable extent.
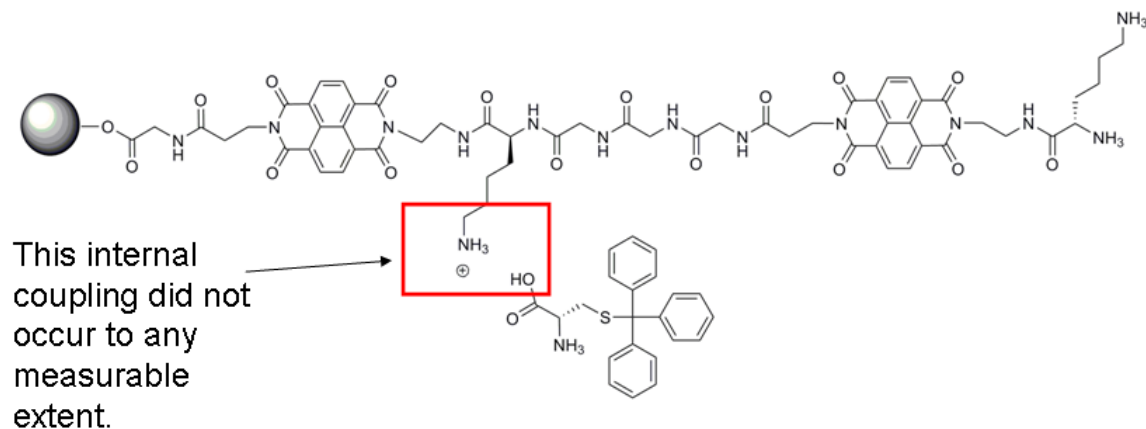
Figure 4.13   Failed internal coupling. The likely reasoning is that the high loading resin sterically inhibited the approach of the trityl protected cysteine amino acid. It was necessary to incorporate the cysteine residue into the lysine-NDI amino acid to avoid this final internal coupling step.
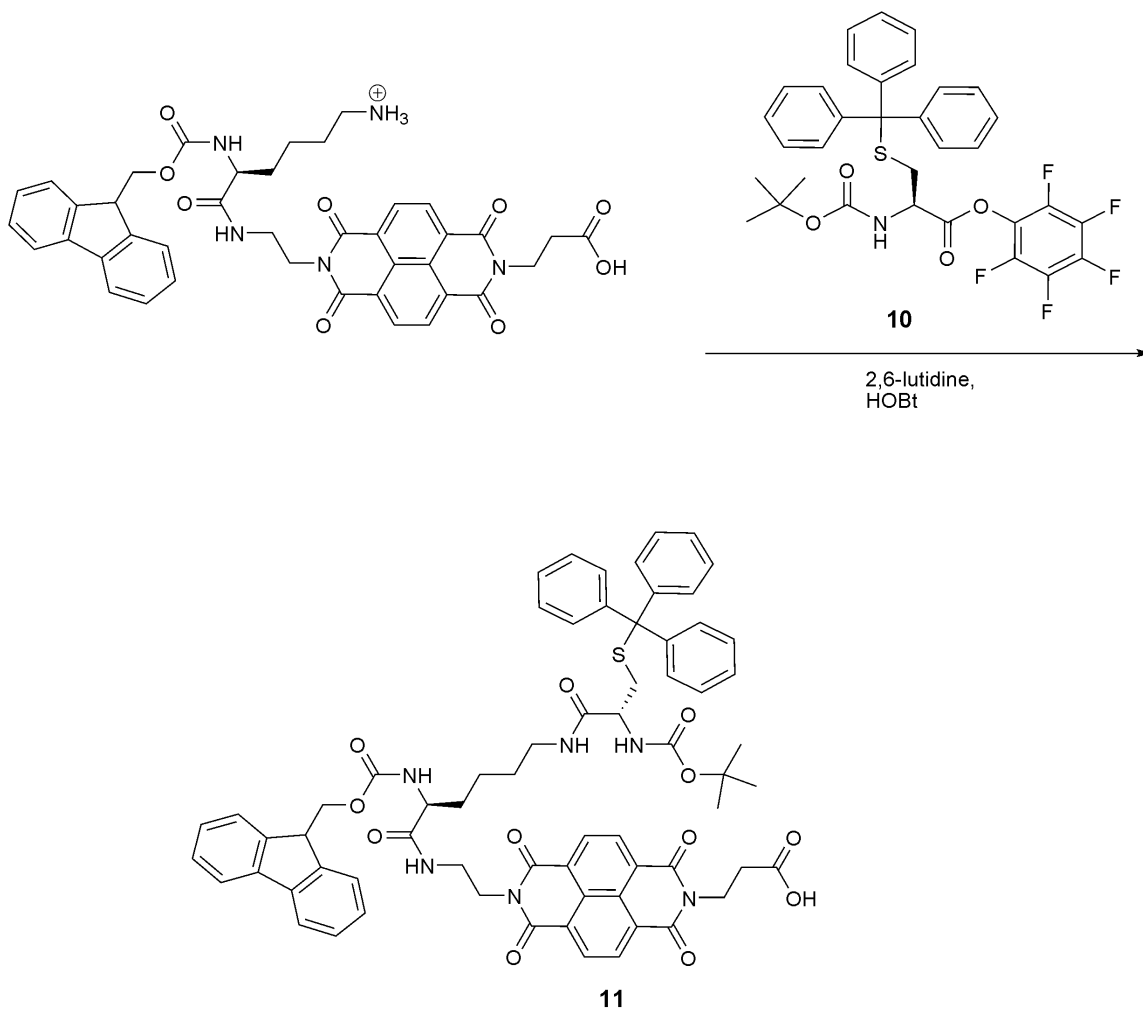
Figure 4.14 Synthesis of Fmoc-Lys(Cys(Trt)-Boc)-NDI-OH.

Both analogues were conjugated to the gold nanoparticles. The UV-Vis data for the conjugation of Bis C extend showed a large decrease in adsorption at 420 nm through the first round of purification, possibly due to a tear in the dialysis unit. Therefore, the Bis KC conjugate was carried through in the analysis (Figure 4.15). To further asses the UV-Vis analysis and the efficacy of dialysis as a means of purification, two sets of control experiments were established. First, it was important to determine the ratio of the absorbance of the gold nanoparticles at A420/A385. This number is used in the

106

calculation for the concentration of intercalator, which has a characteristic absorbance and extinction coefficient at A385. This was established using a dilution series of the same gold nanoparticles (Figure 4.16, Table 3) that were used in the conjugation reaction. The determined ratio was 1.221, close to that of the manufacturer's ratio of 1.24.

To assess the efficacy of the dialysis in removing unreacted intercalator, a control experiment was run in which the same concentration of Bis KC used in the reaction was added to the reaction buffer without gold nanoparticles. This solution was analyzed pre- and post-dialysis and showed that the majority (greater than 90%) of the intercalator was removed. It is therefore reasonable to assume that unreacted intercalator in the reaction will be removed during the dialysis purification.
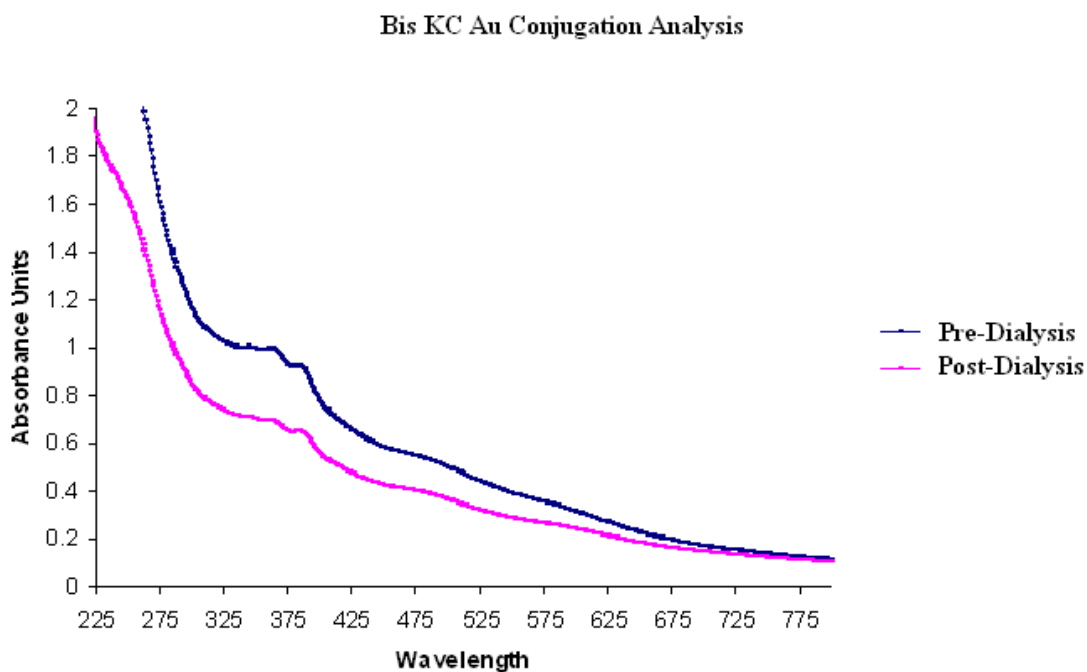
Figure 4.15 UV-Vis Analysis of Bis KC conjugation to the gold nanoparticles.

Step	A420	A385	Abs at 385nm of Bis KC	Au (M)	Bis KC (M)	Bis KC/Au
Pre-Dialysis	0.6745	0.9231	0.11011	4.324×10^{-6}	3.693×10^{-6}	0.854
Post Dialysis	0.4891	0.6483	0.0537	3.135×10^{-6}	1.963×10^{-6}	0.626

Table 4.2 Analysis of the Bis KC to Au ratio from pre- and post-dialysis data. The absorbance at 385 nm of Bis KC was determined using the ratios from Table 3 and inserting them into the following equation: $Abs_{385}-(Ratio*Abs_{420})$.
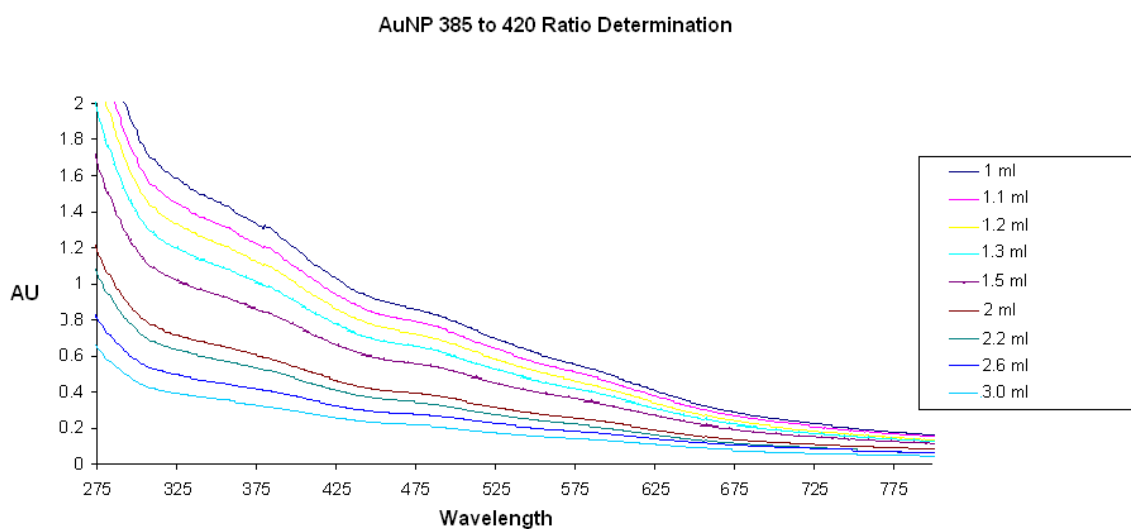
Figure 4.16. Determination of A385/A420 ratio of the gold nanoparticles to be used in calculating the labeling efficiency.

Volume (ml)	Absorbance at 420	Absorbance at 385	385/420 Ratio
1	1.057	1.295	1.2252
1.1	0.969	1.185	1.2291
1.2	0.889	1.087	1.2272
1.3	0.799	0.976	1.2215
1.5	0.682	0.831	1.2185
2	0.478	0.581	1.2155
2.2	0.421	0.512	1.2162
2.6	0.334	0.401	1.2006
3	0.263	0.316	1.2015

Table 4.3 Calculation of the A385/A420 ratio which averaged to be 1.2173

A gel was run using an excess of intercalator and DNA with respect to the K_D of the original G_3K intercalator (Figure 4.18). The fact that the DNA concentration is above the K_D is important because this predicts the bound complex will predominate at equilibrium. There is a distinct difference in DNA movement with the DNA control lane and Bis KC•Au showing that this new conjugate is binding with the nanoparticle now placed in a position where it is not directly associated with the major groove. It is also important to note that the gel shift is similar to that of the G_3K control, perhaps indicating that the maximum binding that could occur in this system has been achieved. And while the Bis C extend•Au conjugate was not extensively characterized by UV-Vis, it did show a gel shift similar to that of the G_3K as well, which suggests that extending the nanoparticle from the peptide linker would allow for maintenance of binding specificity. This is very important when revisiting the cyclic bis-intercalator project.
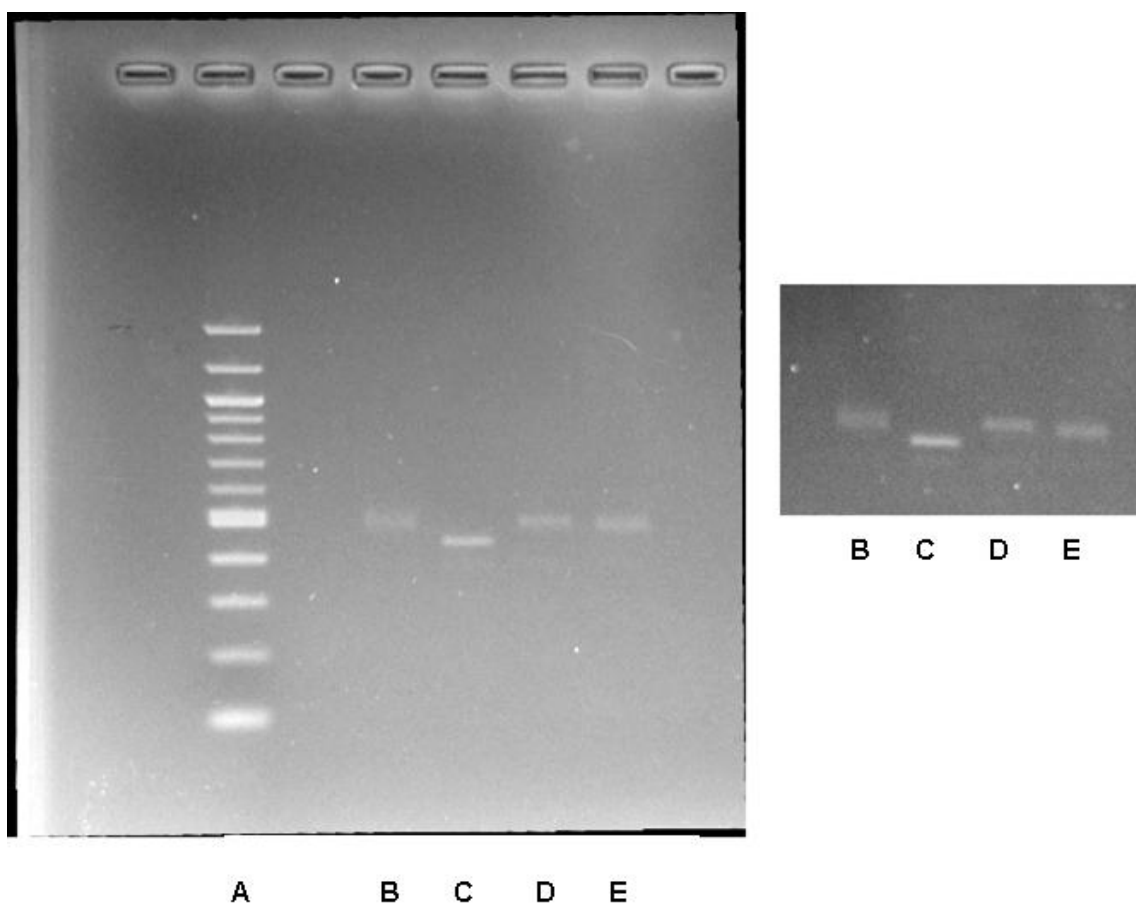
Figure 4.17 Gel-shift assay confirming the binding of the Bis KC•Au conjugate to the DNA. Lane B represents Bis KC•Au. Lane C is control DNA without any intercalator. Lane D is the G_3K control. Lane E is the Bis C extend•Au conjugate, also showing a gel-shift.

4.9 MICROSCOPY OF NEW ANALOGUES

4.9.1 Results

Despite the addition of the poly-l-lysine to the grid sample surface, there were no consistent images of the controlled nanoparticle assembly. Only one set of potentially promising images were obtained (Figure 4.20). Changing concentrations of both the

DNA and the conjugate with respect to the K_D were not able to lead to consistent images of nanoparticle assembly.

4.9.2 Discussion

The initial goal was to avoid direct DNA visualization by examining only the gold nanoparticles. However, the addition of polylysine did not lead to any consistency in sample preparation. Since the chemistry behind DNA sample absorption to the TEM grid is not well documented, it is difficult to assess whether or not the nanoparticle assembly is occurring. It is possible that the gel shifts seen with both the G_3K and Bis KC•Au does not represent a situation where all of the binding sites on the DNA are occupied. This would explain the images (Figure 3.20, B and D) where there seems to be some assembly in comparison to the control images but it is not consistent with regard to number of nanoparticles and nanoparticle spacing expected with the modified DNA.
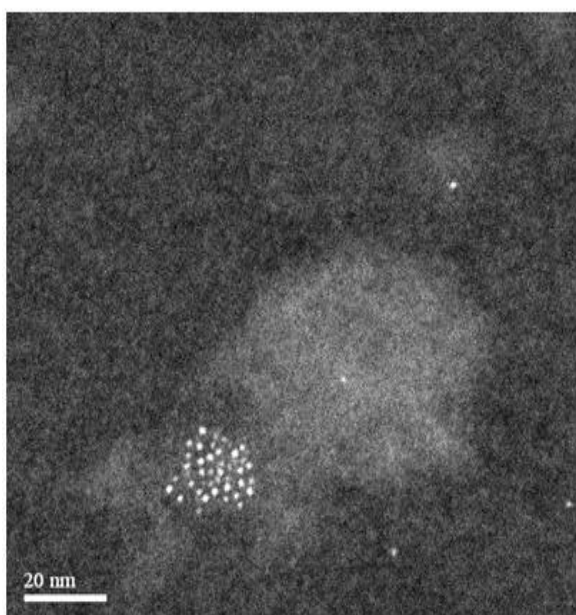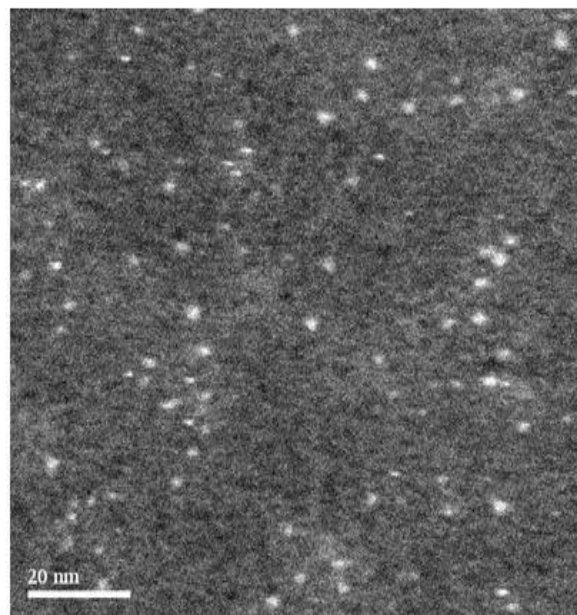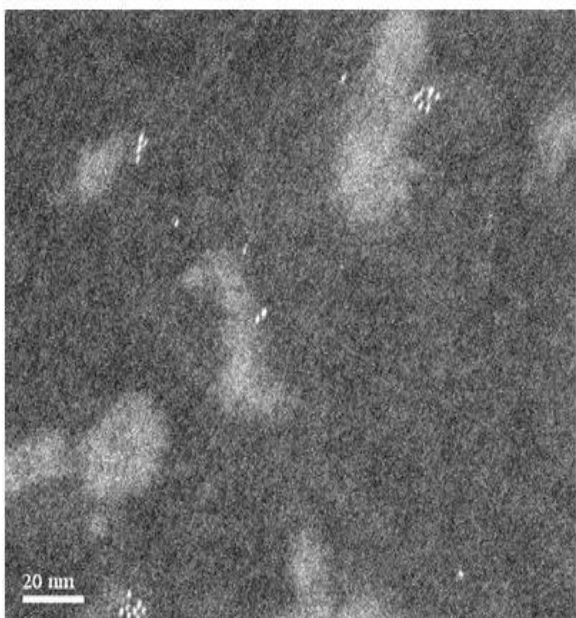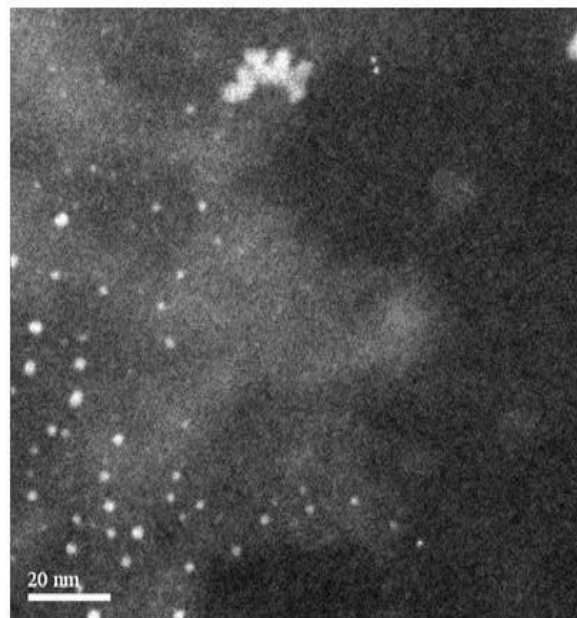
Figure 4.18 Control Images of the functionalized gold nanoparticles without DNA.
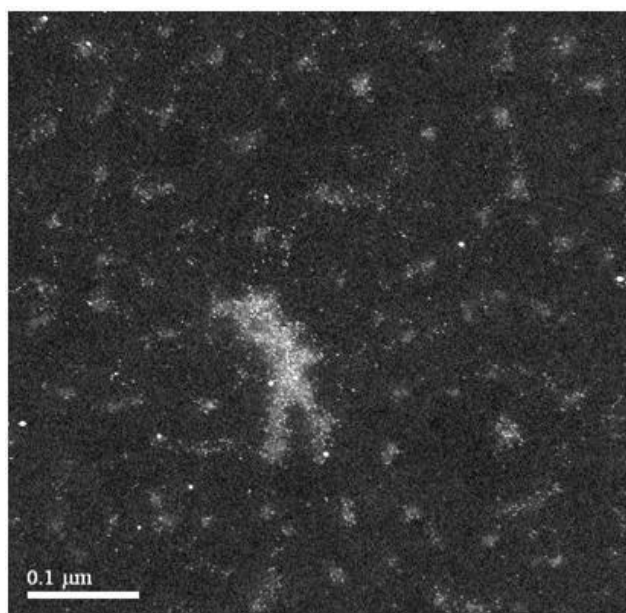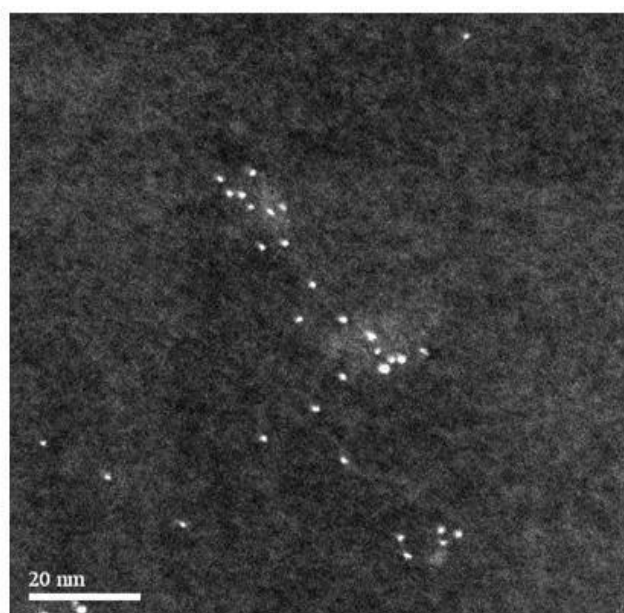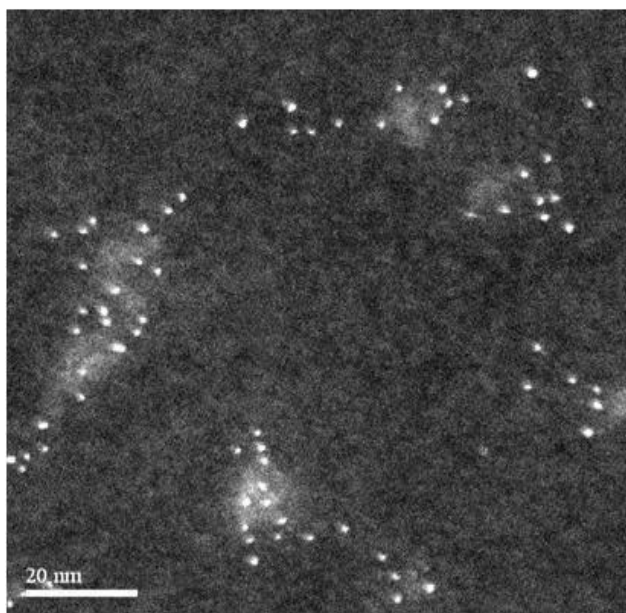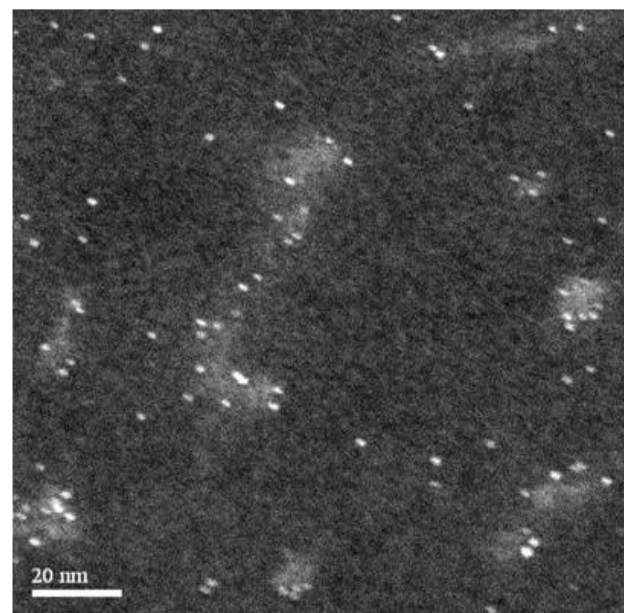
Figure 4.19 Images which show the potential for the control assembly of the
nanoparticles when compared to the control images.

Beyond attempting different sample preparations, it is likely necessary to visualize the individual DNA molecules. This would allow for a statistical analysis where one could determine the average number of gold nanoparticles bound per DNA strand. Even if this does not lead to full occupation of all 26 binding sites, it would still prove that the sequence specificity can be used to control the assembly of nanoparticles and optimization of the DNA design can be pursued.

4.10 REVISITING THE ATOMIC FORCE MICROSCOPE

4.10.1 Results

A new model of an Atomic Force Microscope (Agilent 5500) was used for these new studies. Initial attempts using the divalent salt approach were inconsistent in DNA imaging. A surface modification approach using APS (Figure 4.25) was employed and was successful in imaging plasmid DNA (Figure 4.26); however, shorter individual DNA molecules were not visualized. Table 4.6 summarizes the sample preparation conditions used for the APS modified plasmid DNA imaging.

4.10.2 Discussion

The divalent salt approach was utilized and some images showed promise with regard to identifying possible DNA-like features (Figure 3.21-B). The identified DNA image was only present in a few areas of the grid, leading one to believe that the plasmids may be aggregating. The white feature on the DNA indicates a height of at least 2.4 nm, which is higher than the accepted value of 2nm. Based on the salt control (Figure 3.21-A) image having similar height measurements, it is also possible that the salt concentration is too high and may be coating the DNA giving, it an increased height. A sample was prepared which had a lower salt concentration, but the DNA features were odd in that it appeared as though the plasmids were not intact or completely circular

114

(Figure 4.22). A similar approach was also utilized for the smaller 500-base-pair fragment. A significantly lower salt concentration (2mM) of $MgCl_2$ was used but the images showed that the DNA concentration may have been too high as the wide scan area indicated multiple features that could have been DNA. The salt concentration may still have been too high, making it difficult to clearly identify individual DNA molecules. The zoomed-in image identified a possible DNA strand, however the DNA height exceeds that of 2nm. Table 4.5 summarizes the DNA and salt concentrations used in the subsequent image sets.

Figure	DNA Structure	DNA Concentration	$MgCl_2$ Concentration
1	Plasmid (7300 bp)	0.3 nM	10 mM
2	Plasmid (7300 bp)	0.3 nM	5 mM
3	Insert (500 bp)	41 nM	2 mM

Table 4.4 Summary of salt and DNA concentrations used for the divalent salt DNA preparations.
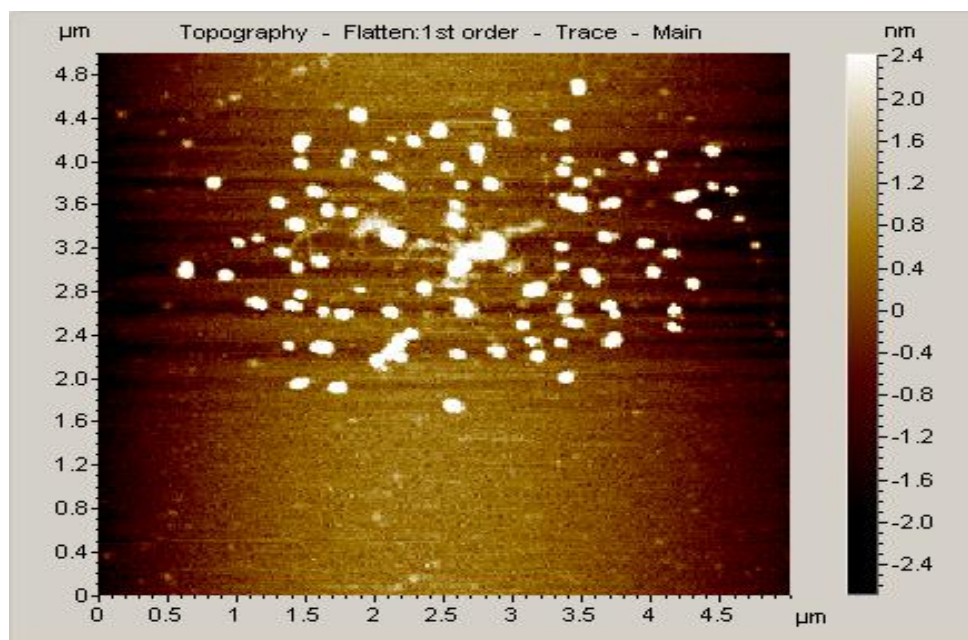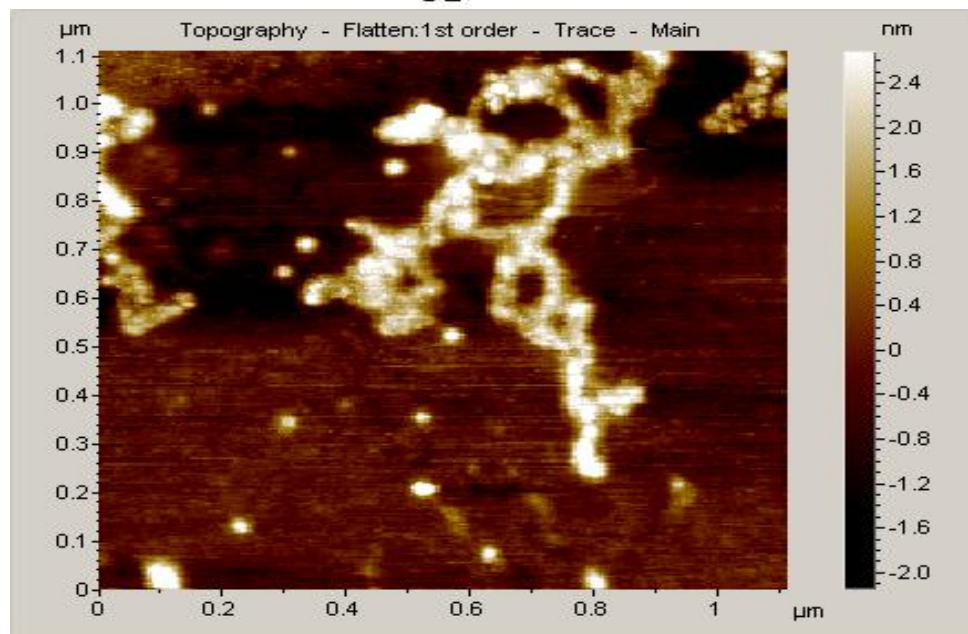
Figure 4.20 Salt control (A) and possible aggregated image of plasmid DNA (B). The overall height scale bar of 2.4nm shows both the salt and DNA features to be near this height.
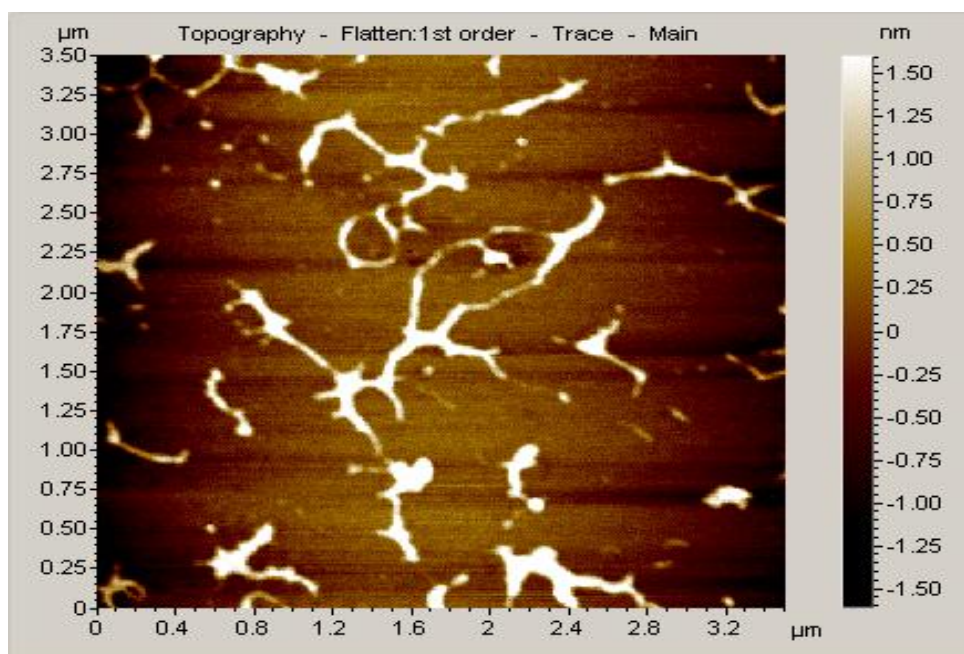
A
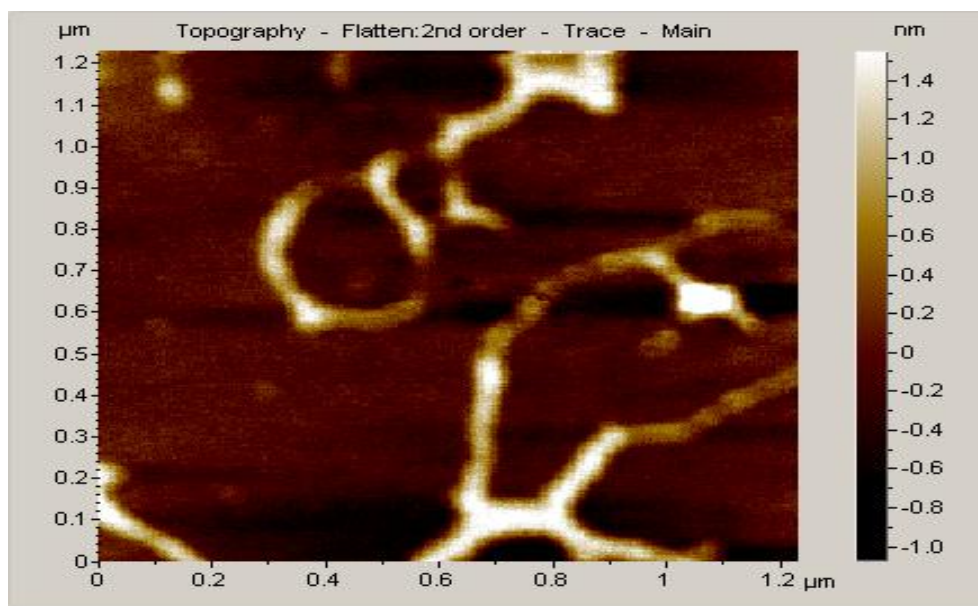
B

Figure 4.21. A represents a wide scan of a large area and B represents a close up image
of the circular feature seen in A.

117
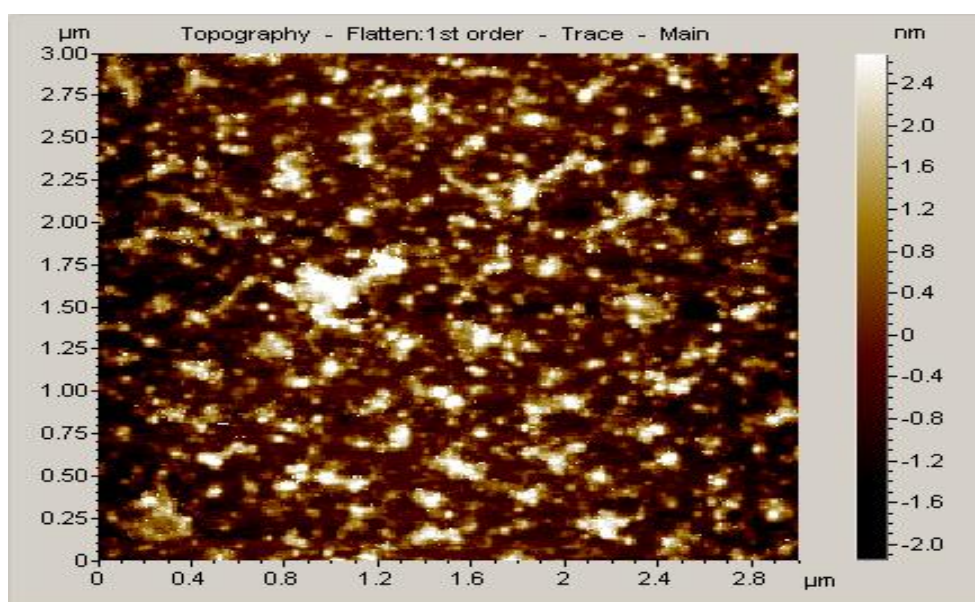
A
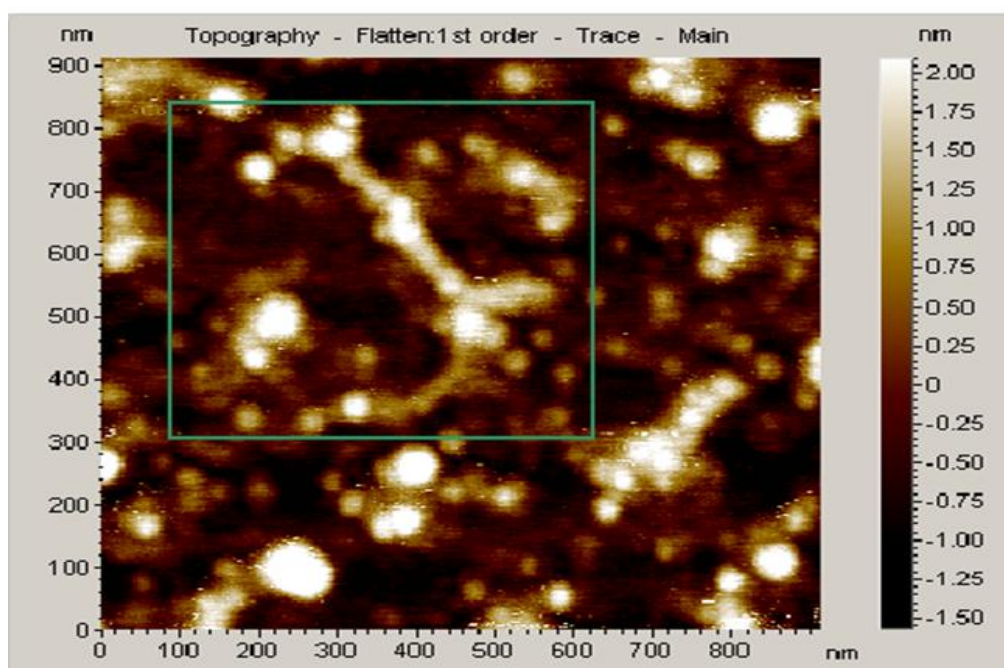
B

Figure 4.22 A represents a large field scan with yellow arrows pointing out possible strand-like DNA features. The green box in B represents a possible DNA structure.

During these investigations, experiments related to the dissociation kinetics of the threading tetraintercalator have shown that the addition of $MgCl_2$ (> 1nM) leads to an increase in the dissociation rate of the tetraintercalator from its binding site. Because the binding affinity of this molecule is higher than that of the bis-intercalators, it is likely that $MgCl_2$ present in sample preparations of the conjugate-DNA complex may lead to an increased dissociation of the intercalator-nanoparticle conjugate. This could interfere with the interpretation of the nanoparticle assembly. At that point, it was decided that an alternative approach that did not rely on divalent salts would be necessary to avoid increased dissociation of the intercalator-nanoparticle conjugate from the DNA. A modification of the aminopropyl tri-ethoxy silate (APTES) approach was recently published (Shlyakhtenko 2003) which utilized 1-(3-Aminopropyl)silatrane (APS) to modify the mica surface.

The APS surface modification approach avoids the use of divalent salts and allows one to focus on the surface chemistry as a means to modify sample preparations. When freshly cleaved, the mica surface contains siloxy groups, with pKa's of approximately 6.8. At neutral pH, there is an equilibrium between protonated and deprotonated forms, giving the mica a negatively charged surface (Figure 24). The deprotonated siloxy group can then act as a nucleophile towards the APS complex, and the amine present, with a pKa of approximately 10, will be protonated and provide a positive sample surface to which the DNA can bind electrostatically.
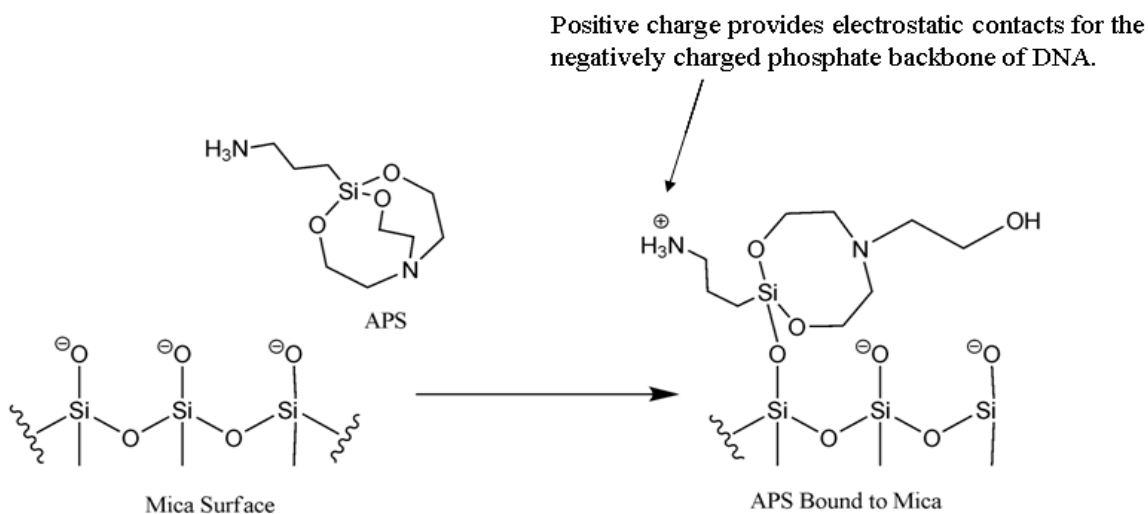
Figure 4.23. Representation of the modification of the mica surface using APS.
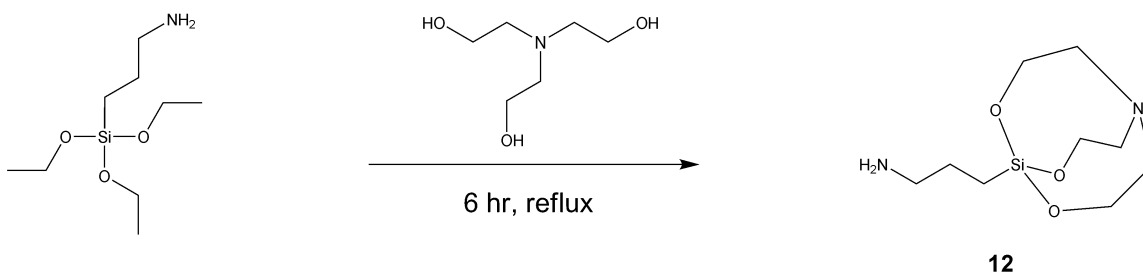
Figure 4.24. APS mica synthesis in which aminopropyl triethoxy silane was refluxed with triethanolamine to give 1-(3-Aminopropy)silatrane (APS).

Three types of DNA were examined with this methodology: Circular plasmid, linearized plasmid, and the 500-base-pair linear strand. Table 6 summarizes the concentrations of DNA and APS used. As seen in Figure 26, the highest concentration used gave conclusive images of plasmid DNA and two wide scan areas are shown. One apparent feature is the lack of aggregated salt features which were present in the other images. While the concentration of DNA is still too high, the height and width seems to match up well against traditional DNA measurements and the images portray the

120

anticipated strand-like features of DNA.   When this same approach was used for the smaller DNA fragments, the identification of distinct DNA fragments was not as clear. In particular, some of the DNA features have an increased width when compared to the plasmid images. The same features seen in the salt based methods, which indicate that something in the DNA buffer solution may be interfering with the DNA visualization. It is also possible that if the identified features are individual DNA fragments, the DNA concentration may still be too high. The linearized plasmid was used (similar in base pair length of the circular plasmid), but at a lower concentration than the circular plasmid and it was difficult to determine if there was DNA present. One area showed a few possible features and Figure 28 represents the most promising image. The simplest reasoning may be that the concentration of DNA was too low to allow for significant coverage of the mica.

Figure	DNA Type	DNA Concentration	APS Concentration
1	Plasmid (7000 bp)	3.03 nM	0.16 mM
2	Linear (500 bp)	12 nM	0.16 mM
3	Linear Plasmid (5000 bp)	0.86 nM	0.16 mM

Table 4.5 Summary of AFM imaging for the APS surface modification.

121
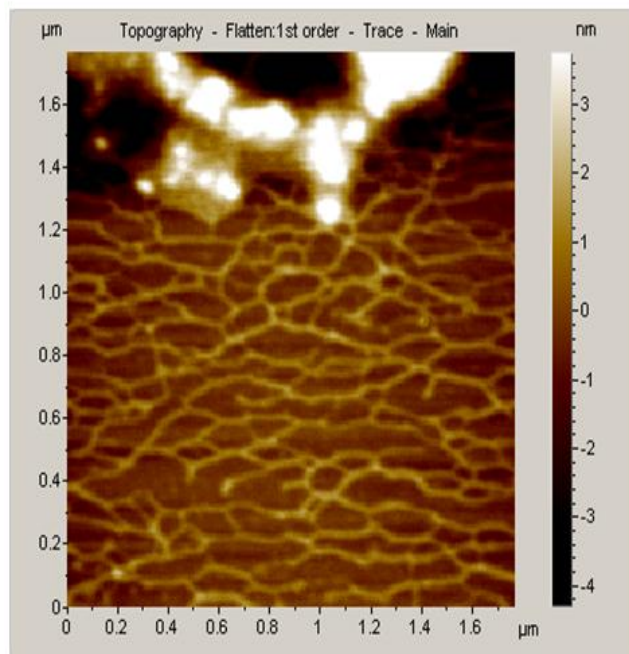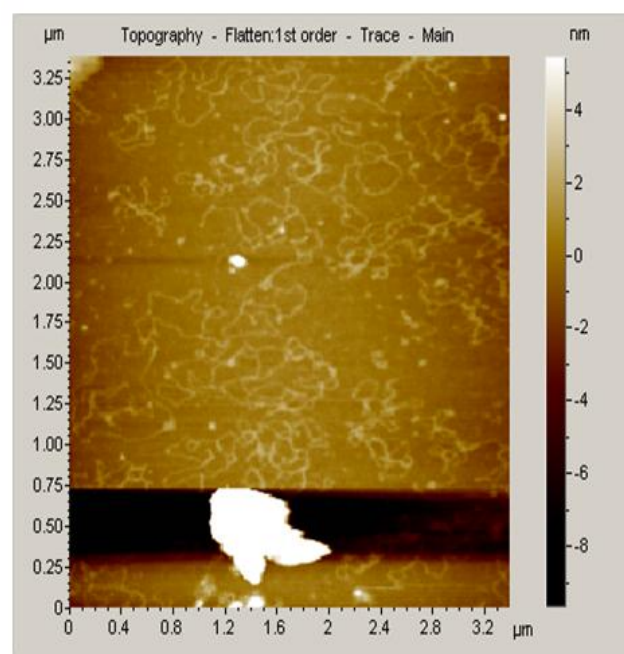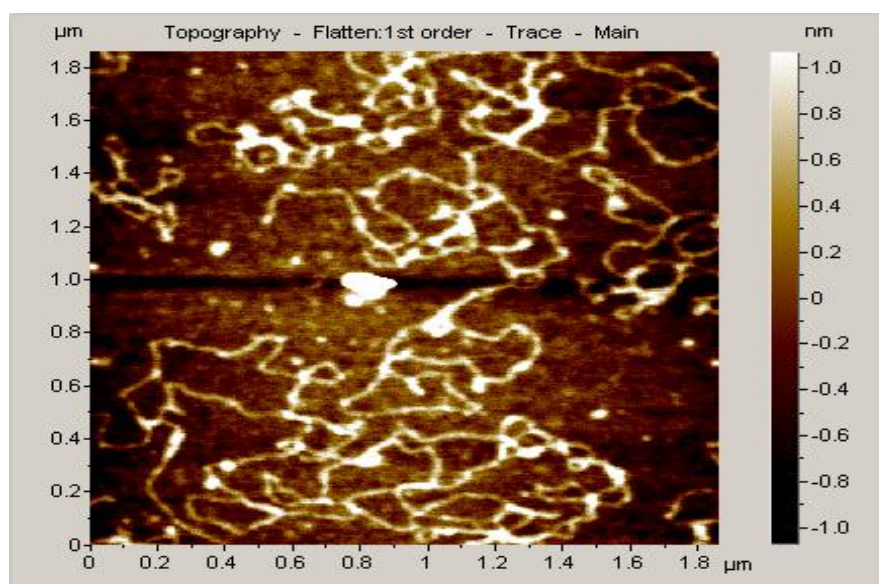
Figure 4.25 Three different wide scan areas of the same plasmid DNA sample via APS
mica modification approach.
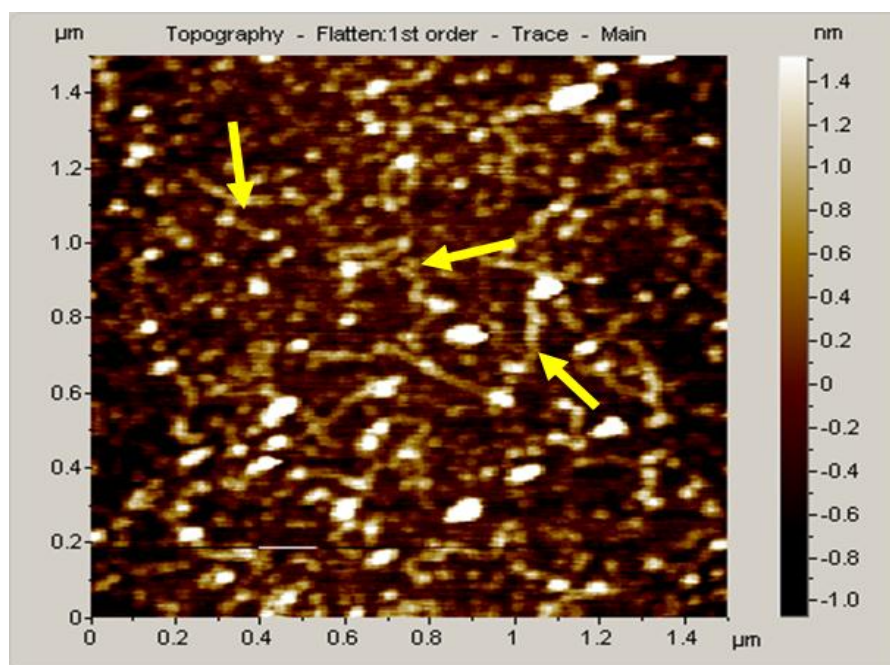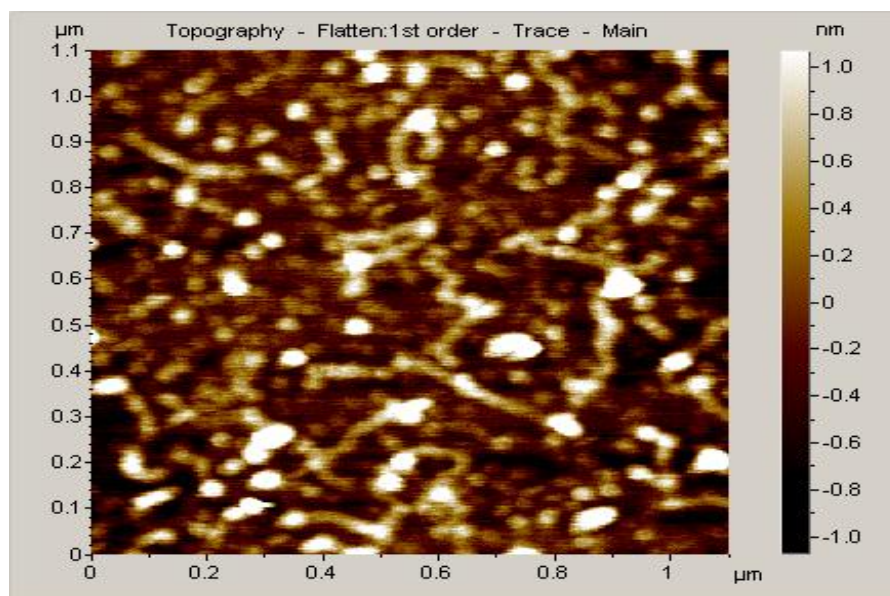
Figure 4.26. Images of the 500 base pair insert using APS modified mica. The yellow arrows in (A) indicated possible DNA strands, with (B) representing the same area.

123
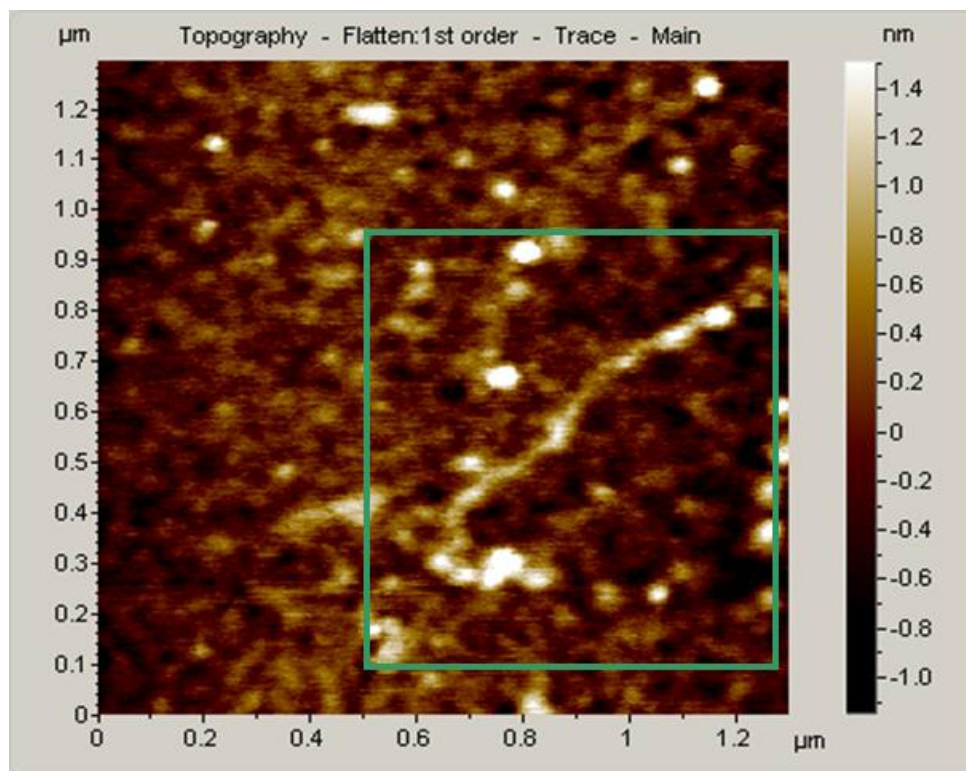
Figure 4.27. Possible linearized DNA feature.

In order to examine the concentration effect, two samples of circular plasmid and linear fragment were prepared at 0.4 and 1.2 nM respectively. The linear fragment images did not show any features that were present in the higher concentration sample. Unfortunately, the plasmid images were unable to be appropriately analyzed, as the mica sheet used had significant surface deformities, making it nearly impossible to identify any features. Before new samples could be prepared, the AFM had electronic failures which required the instrument be serviced and this process has taken several months.

At this point, two assumptions can be made. First is that the surface chemistry is not optimal at these conditions used. For example, if the pH of the APS solution is too

low, then the mica surface will not be fully deprotonated, preventing the APS from maximizing its covalent attachment and the DNA would not uniformly absorb. It is also possible the pH is not the issue and the APS coverage is not optimal causing inconsistencies in overall positive charge on the surface. This could lead to the second assumption, that the DNA plasmids have more points of positive charge and as equilibrium between bound and unbound DNA occurs, the larger DNA has a higher percentage of "sticking" to the mica.

With regard to the plasmid DNA, it is also possible that the highest concentration of DNA has been established with respect to the 3.05 mm mica sheets. If a low concentration threshold could be established, it may be possible to fine tune the protocol to allow for optimal imaging conditions which could clearly identify individual DNA molecules. If this is accomplished, then surface chemistry may be ruled out and that optimal concentration can be used in future experiments. It is also possible to use different concentrations of APS and adjust the pH of sample solutions to examine the surface chemistry effect on DNA sample preparation.

4.11 CHAPTER SUMMARY

A protocol has been established to determine the optimal placement of a gold nanoparticle onto a DNA intercalator of interest and confirm the maintenance of binding specificity. Initial electron microscopy studies were inconclusive as to whether or not the nanoparticle assembly is occurring, however the lack of understanding regarding DNA sample preparation does not allow one to definitively draw any conclusions. The Atomic Force Microscope is the most promising tool to be used for the nanoparticle assembly. In conjunction with a more complete understanding of the surface chemistry behind the sample preparation, there is tangible evidence that the DNA can be visualized. This

breakthrough should lead to the visualization of individual DNA molecules which will allow a more accurate assessment of the nanoparticle assembly.

4.12 FUTURE GOALS

The initial project goals have almost been achieved. The immediate next step is to determine the optimum concentrations of both APS and DNA which will allow for the visualization of individual DNA molecules. If successful, then the blueprint can be established in our laboratory and we can begin to use molecules which bind different sequences to control the assembly of nanoparticles. This potential versatility would provide a truly unique system which can finitely control the placement of multiple types of nanoparticles to begin to explore potential materials and other applications.

EXPERIMENTALS

General

All chemicals were purchased from Sigma-Aldrich or Acros organic. Peptide starting materials and coupling reagents were purchased from Novabiochem. Dialysis membranes and TCEP were purchased from Piercenet. Silica 60 F_{254} glass-based plates (Merck) were used for TLC. Flash Chromatography was carried out using ICN SiliTech 32-63D 60 A^o silica gel. All NMR spectra were recorded on Varian 400 or 600 MHz Instruments. CDCl$_3$ (δ_H = 7.26, δ_C = 77 ppm), DMSO-d$_6$ (δ_H = 2.5, δ_C = 140.9 ppm), and D$_2$O (δ_H= 4.67 ppm) were used as solvents. Nanoparticles were purchased from Nanoprobes Incorporated®. TEM grids and poly-l-lysine were purchased from Electron Microscopy Sciences, containing carbon or formvar coated over copper (400 mesh.) Mica sheets were purchased from Ted Pella Inc, or SPI. AFM probes were purchased from NanoAndMore. PPP-NCH-10 or NCH-10 probes were utilized. All agarose gels were run using standard biochemical apparatus' and DNA ladders and glycerol were purchased from NEB.

TEM Samples of DNA and Bis C•Au Incubations.

All incubations were prepared 24 hours in advance of microscopy imaging. DNA concentrations are measured in binding sites (DNA concentration x 26). All control incubations were prepared with the Bis C•Au conjugates at the same concentration used in the experimental incubations and did not include any DNA. All experimental are described for figures 3.8 and 3.9. For A and B, the samples were prepared as described: The stock solution of Bis C was 0.921 uM and the DNA stock solution was 150 nM. For A, 10 uL of DNA was incubated with 5 uL of Bis C•Au (100 nM DNA, 307 nM Bis C•Au). For B, 15 uL of DNA was incubated with 2 uL of Bis C•Au (133 nM DNA, 109 nM Bis C•Au). The control incubations were prepared by adding the respective amount of Bis C•Au to diH$_2$O to give the same sample volume of the experimental incubations.

The samples were prepared for imaging by first glow discharging the carbon coated grid and then adding approximately 5 uL of sample directly to the grid for 5 minutes. The grid was washed with diH$_2$O (2 x 3 uL) and then dried under a lamp for 1 min. The grids were immediately imaged. Five different areas of each grid were examined and approximately 10-15 pictures of each area were taken. The images shown are representative of the most consistent features. For C and D, the same Bis C•Au stock (0.921 uM) was used. The DNA stock concentration was 300 nM. For C, 10 uL of DNA was added to 5 uL of Bis C•Au (200 nM DNA, 307 nM Bis C•Au). For D, 10 uL of DNA was added to 10 uL of Bis C•Au (150 nM DNA, 461 nM Bis C•Au). The samples were prepared by first glow discharging the carbon coated grid, and adding 5 uL of polylysine (0.001 % v/v) for 1 min. The grid was then washed with diH$_2$O (2 x 5 uL) and then 5 uL of the incubation sample was added for 5 min, washed with diH$_2$O, and then imaged. The controls were prepared in the same manner as described above.

TEM Samples of DNA and Bis KC•Au Incubations

The images for figures 19 and 20 were obtained from the following sample preparation. The DNA stock concentration was 0.6 uM and the Bis KC•Au stock concentration was 2.12 uM. The incubations were prepared 24 hours in advance of imaging. The experimental incubation was prepared by adding 6 uL of DNA to 2 uL of Bis KC•Au (450 nM DNA, 544 nM Bis KC•Au) and the control image was prepared by adding 6 uL of diH$_2$O to 2 uL of Bis KC•Au. The samples were prepared by first glow discharging the carbon coated grid, and then adding 5 uL of polylysine (0.001 % v/v) for 1 minute, washing with diH$_2$O, and then adding 5 uL of the sample for 5 minutes. The grid was again washed with water and imaged immediately. The images were obtained by examining four different areas of each grid and taking approximately 15-20 pictures of each area.

128

AFM Samples

For the divalent salt approach, plasmid DNA (7000 bp) and a smaller DNA fragment (500 bp) was prepared. After freshly cleaving a mica sheet (3.05 mm), a solution of DNA was mixed with $MgCl_2$, at the concentrations listed in Table 3.5, and the salt-DNA solution was incubated on the mica sheet for 10 minutes. The solution was blotted off with filter paper, washed with 5 uL of diH_2O three times, and dried under a stream of nitrogen. An Agilent 5500 AFM with a Nanoscope IV controller was utilized. The height scale bar was adjusted to 5nm as the flattest areas of the mica were examined. All images were first order flattened during imaging. Tip used had resonant frequencies around 320 kHz.

For the APS mica approach, APS was synthesized as discussed below and fresh solutions of approximately 50 mM in diH_2O were prepared for daily use. The final APS concentration was 0.167 M for all sample preparations. A freshly cleaved mica sheet (3.05 mm) was incubated with 10 uL of APS for 30 minutes. The mica was washed with water and then the DNA sample of varying concentrations (Table 3.6) were added and incubated for 10 minutes. The solution was removed with filter paper, washed with water, and dried under a stream of nitrogen. Samples were immediately imaged after preparation.

Fmoc-Gly-Gly-Gly-OH (Fmoc-triglycine) (6).

Sodium carbonate (10.578 mmoles, 1.12 g) was dissolved in 12 mL of diH_2O in a 100 mL round bottom flask. To this stirring suspension was added triglycine (5.289 mmoles, 1 g) and the solution was cooled to 0° C. The solution was relatively clear at this point and then 9-Fluorenylmethyl succinimidyl carbonate (Fmoc-OSu) (5.289 mmoles, 1.78 g) was dissolved in 20 mL of DMF and added to the aqueous solution. A precipitate immediately formed and the suspension was stirred for 1 h. The suspension was diluted

with 500 mL of water and the aqueous layer extracted with ethyl acetate (2 x 250 mL). The water (pH ~8) was cooled in an ice bath and acidified with 0.1M HCl until a pH of 3 was attained. A precipitate had formed and the suspension was extracted with ethyl acetate (2 x 250 mL). The precipitate had transferred from the aqueous to organic layer during the extraction. The ethyl acetate aliquots were combined, washed with sat. NaCl (3 x 100 mL) and water (3 x 100 mL), and then the ethyl acetate was dried with sodium sulfate. The organic layer was filtered, evaporated under reduced pressure, and dried under vacuum to afford a powdery yellow solid (1.05 g, 48% yield). LC-MS analysis indicated one major peak. ^{1}H NMR (400 MHz, CDCl$_3$) δ 8.05 (d, 2H, J= 7.1), 7.81 (d, 2H, J= 7.8), 7.58 (t, 2H, J= 8), 7.35 (t, 2H, J= 7.6), 4.63 (d, 2H), 4.37-4.44 (m, 3H), 4.21 (s, 2H), 3.95 (s, 2H). HRMS (ESI) calculated for C$_{21}$H$_{21}$N$_3$O$_6$ [M+H]$^+$ 411.143, found 411.308.

Solid Phase Synthesis of BisC (7). All washes consisted of NMP (3 x 5 mL)-isopropanol (4 x 5 mL)-NMP (3 x 5 mL) unless otherwise specified. All Fmoc deprotections used 20% piperidine in DMF (6 mL, 2 x 15min) followed by a wash. Capping steps consisted of adding 8 mL of 5% 2,6-lutidine and 5% acetic anhydride in NMP (2 x 10 min) followed by a wash. All coupling steps utilized 3 equivalents of amino acid, 3 equivalents of PyBop, and 6 equivalents of N-methylmorpholine (NMM). The synthesis was accomplished on a 0.2 mmole scale.

Resin Loading: Rink amide resin (0.350 g, 0.72 mmol/g) was swollen with NMP (10 mL) for 30 min in a 10 mL filter fritted syringe. A solution of 20% piperidine in DMF was added (2 x 20 mL) to remove the Fmoc protecting group. The resin was then washed and was ready for the peptide couplings.

Synthesis: The first coupling used an Fmoc protected glycine amino acid (Fmoc-Gly-OH) (0.225 g), which was dissolved in 4 mL of NMP along with PyBop (0.390 g) and NMM

(165 uL). The coupling occurred for 1 hour, followed by washing and capping steps. The Fmoc group was removed and the cysteine-NDI monomer (**3**) (0.711 g), PyBop (0.390 g), and NMM (165 uL) were dissolved in 4.5 mL of NMP and coupled for 1.5 hours. The resin was then washed with NMP (3 x 5 mL) and a second coupling solution was added for an additional 1.5 hours. The resin was washed with DMSO-NMP-isopropanol-DMSO-NMP (3 x 5 mL each) and then capped. Three successive glycine residues (Fmoc-Gly-OH) (0.225 g) were coupled as previously described. The Fmoc group of the third glycine residue was removed and the lysine-NDI monomer (Fmoc-Lys(Boc)-NDI-OH) (0.625 g) was dissolved in 5 mL of NMP along with PyBop (0.390 g) and NMM (165 uL). The coupling occurred overnight (12 h) and the resin then washed with DMSO (3 x 5 mL) and NMP (3 x 5 mL). A second coupling solution was added for an additional 2 h. The resin was washed with DMSO-NMP-DMSO-NMP (3 x 5 mL), followed by a regular wash. The final Fmoc group was removed and the peptide was ready for resin cleavage. A mixture of 95%/2.5%/2.5% TFA/diH$_2$O/TIPS (5 mL total) was added to the resin for 3 h. The solution was collected in a 100 ml round bottom flask and the TFA was removed under a N$_2$ stream. The oily residue was dissolved in water, frozen, and lyophilized overnight. The solid was then washed with cold ether and again dissolved in water, frozen, and lyophilized overnight. The crude material was dissolved in 0.1% TFA/H$_2$O and purified by reverse-phase preparative HPLC (Waters, C18 VYDAC HPLC column, (Cat. #218TP1022) using 0.1% TFA/water (v/v) as solvent A and 0.1% TFA/AcCN (v/v) as solvent B. A starting gradient of 16.5% A and 83.5% B was used and transitioned to 19% A and 81% B over a 40 minute period. The major peak was the desired product in its reduced form which was confirmed by LC-MS, ESI-MS, and ^{1}H NMR. The oxidized product was characterized by taking pure product, dissolving in water, and analyzed via HPLC using a gradient of 18% A to 21.5%

A over 40 minutes. The second peak was identified by LC-MS and ESI-MS as the oxidized product. HRMS (ESI) calculated for $C_{55}H_{60}N_{14}O_{16}S$ $[M+H]^+$ 1204.403, found 1204.395. HRMS (ESI) calculated for $C_{110}H_{118}N_{28}O_{32}S_2$ $[M+H]^{2+}$ 1203.395, found 1203.387.

BisC•Au Conjugation (Figure 4.7). Crude Bis C was purified and used when needed. Prior to conjugation, an aliquot of purified material was dissolved in diH$_2$O and approximately 100 uL was analyzed via HPLC to assess the level of oxidation. A series of dilutions from this stock solution were prepared and the stock concentration of Bis C was determined to be 3.345 x 10^{-5} M. The HPLC analysis indicated approximately 8% oxidation which was based on comparing the peak areas of the reduced and oxidized peaks. The maleimide functionalized gold nanoparticles® (6 nmol) were dissolved in 5.5 mL of diH$_2$O and the solution was vortexed several times over a five minute period. To this vortexed solution was added 200 uL of the Bis C stock solution. The reaction solution was vortexed several times and then stored at room temperature overnight. The reaction occurred for approximately 15 hours prior to purification. The solution was analyzed via UV-Vis prior to purification and the analysis revealed a 1.38:1 ratio of Bis C to AuNP. The reaction solution was added to a pre-rinsed membrane centrifugation tube with a 3,500 MWCO and was centrifuged for 10 min at 3,000 rpm. The solution was reconstituted to its original volume using phosphate buffer (0.02 M, 75 mM NaCl, pH ~7.4) and again centrifuged for 10 min at 3,000 rpm. The solution was reconstituted to a total volume of 3 mL, centrifuged for 10 min at 3,000 rpm, and reconstituted to a final volume of 2.1 mL. This final solution was then analyzed via UV-Vis and revealed a final ratio of 0.79:1 Bis C to AuNP, indicating that there are likely nanoparticle which do not contain an intercalator. This final solution was 1.115 uM in AuNP and 0.921 uM in Bis C.

Solid Phase Synthesis of Bis KC (8). All washes consisted of NMP (3 x 5 mL)-isopropanol (4 x 5 mL)-NMP (3 x 5 mL) unless otherwise specified. All Fmoc deprotections used 20% piperidine in DMF (6 mL, 2 x 15min) followed by a wash. Capping steps consisted of adding 8 mL of 5% 2,6-lutidine and 5% acetic anhydride in NMP (2 x 10 min) followed by a wash. All coupling steps utilized 3 equivalents of amino acid, 3 equivalents of PyBop, and 6 equivalents of N-methylmorpholine (NMM). The synthesis was accomplished on a 0.1 mmole scale.

Resin Loading: Fmoc-Gly Wang resin (0.155 g, 0.65 mmol/g) was swollen with NMP (10 mL) for 30 min in a 10 mL filter fritted syringe. A solution of 20% piperidine in DMF was added (2 x 20 mL) to remove the Fmoc protecting group. The resin was then washed and was ready for the peptide couplings.

Synthesis: The lysine-NDI monomer (Fmoc-Lys(Boc)-NDI-OH) (0.250 g) was first coupled for 1 hour in a solution of 4 mL of NMP. The lysine-NDI monomer was first dissolved in NMP, and then PyBop (0.156 g) and NMM (65 uL) were added immediately prior to coupling. The resin was then washed with DMSO (3 x 5 mL) and NMP (3 x 5 mL) and a second coupling solution was added for an additional hour. The resin was washed with NMP-DMSO-Isopropanol-NMP (3 x 5 mL of each component) and capped. The Fmoc group was removed using the deprotection solution. Then, Fmoc-triglycine (0.170 g, 3 equivalents) and PyBop (0.156 g) was dissolved in 2.5 mL of NMP and then NMM (65 uL) was added immediately prior to addition to the resin. The coupling occurred for 1.5 hours, followed by washing and capping steps. The Fmoc group was again removed using the deprotection solution and the lysine-NDI monomer was again coupled twice as described above using the same washing steps. The resin was capped and the Fmoc group removed using the deprotection solution. For the final coupling,

Fmoc-Cys(Trt)-OH (0.152 g, 4 equivalents) and O-(7-Azabenzotriazol-1-yl)-N, N, N', N'-tetramethyluronium hexafluorophosphate (HATU) (0.234 g, 4 equivalents) were dissolved in 3 mL of DMF. Then, collidine (TMP) (53 uL, 4 equivalents) was added immediately prior to addition to the resin. The coupling occurred for 1.5 h, followed by a wash. The final Fmoc group was removed using the deprotection solution, and a final wash was done. The boc and trityl protecting groups were removed as the peptide was simultaneously cleaved from the resin using a combination of TFA (4.75 mL), tri-isopropylsilane (TIPS, 0.125 mL), and diH$_2$O (0.125 uL) which was added to the resin for 1.5 hours. The solution was removed and a second solution then added for 30 min. The cleavage solution was placed under a stream of nitrogen to remove the majority of the TFA. The remaining residue was dissolved in water and lyophilized overnight. The lyophilized solid was washed with cold ether, dissolved in water, and again lyophilized overnight. The crude material was purified was dissolved in 0.1% TFA/H$_2$O and purified by reverse-phase preparative HPLC (Waters, C18 VYDAC HPLC column, (Cat. #218TP1022) using 0.1% TFA/water (v/v) as solvent A and 0.1% TFA/AcCN (v/v) as solvent B. A starting gradient of 16.5% A and 83.5% B was used and transitioned to 19% A and 81% B over a 40 minute period. The major peak was the desired product in its reduced form which was confirmed by LC-MS, ESI-MS, and ^{1}H NMR. The oxidized product was characterized by taking pure product, dissolving in water, and analyzed via HPLC using a gradient of 18% A to 21.5% A over 40 minutes. The second peak was identified by LC-MS and ESI-MS as the oxidized product. ^{1}H NMR (600 MHz, D$_2$O) δ 8.36-8.15 (m, 8H), 4.72-4.64 (m, 6H), 4.36-4.24 (m, 4H), 4.04-3.76 (m, 12H), 3.44-3.32 (m, 2H), 2.79-2.65 (m, 8H), 1.52-1.44 (m, 9H), 1.16-1.20 (m, 4H). HRMS (ESI) calculated for C$_{61}$H$_{72}$N$_{15}$O$_{18}$S [M+H]$^+$, 1334.490, found 1334.978. HRMS (ESI) calculated for C$_{122}$H$_{141}$N$_{30}$O$_{36}$S$_2$ [M+H]$^{2+}$ 1332.4822, found 1332.4713.

Solid Phase Synthesis of Bis C ex' (9). All washes consisted of NMP (3 x 5 mL)-isopropanol (4 x 5 mL)-NMP (3 x 5 mL) unless otherwise specified. All Fmoc deprotections used 20% piperidine in DMF (6 mL, 2 x 15min) followed by a wash. Capping steps consisted of adding 8 mL of 5% 2,6-lutidine and 5% acetic anhydride in NMP (2 x 10 min) followed by a wash. All coupling steps utilized 3 equivalents of amino acid, 3 equivalents of PyBop, and 6 equivalents of N-methylmorpholine (NMM). The synthesis was accomplished on a 0.05 mmole scale.

Resin Loading: Fmoc-Gly Wang resin (0.77 g, 0.65 mmol/g) was swollen with NMP (5 mL) for 30 min in a 5 mL filter fritted syringe. A solution of 20% piperdine in DMF was added (2 x 20 mL) to remove the Fmoc protecting group. The resin was then washed and was ready for the peptide couplings.

Synthesis: The lysine-cysteine-NDI monomer (Fmoc-Lys(Cys(Trt))-Boc)-NDI-OH) (0.18 g, 3 equivalents) and PyBop (0.78 g, 3 equivalents) were dissolved in 2.5 mL of NMP. NMM (35 uL) was added immediately prior to adding the solution to the resin. The coupling occurred for 1.5 hours. The coupling solution was removed; the resin washed with DMSO (3 x 5 mL) and NMP (3 x 5 mL), and a second coupling solution was added for 1.5 h. The resin was washed with NMP-DMSO-Isopropanol-NMP (3 x 5 mL of each component) and capped. The Fmoc group was removed using the deprotection solution. Then, Fmoc-triglycine (0.65 g, 3 equivalents) and PyBop (0.80 g, 3 equivalents) was dissolved in 2.5 mL of NMP and then NMM (35 uL) was added immediately prior to addition to the resin. The coupling occurred for 1.5 hours, followed by washing and capping steps. The Fmoc group was again removed using the deprotection solution and the lysine-NDI monomer coupled twice as described above using the same washing steps. The resin was capped and the Fmoc group removed using the deprotection solution. A final wash was done and the boc and trityl protecting groups were removed as the

135

peptide was simultaneously cleaved from the resin using a combination of TFA (4.75 mL), tri-isopropylsilane (TIPS, 0.125 mL), and diH$_2$O (0.125 uL) which was added to the resin for 1.5 hours. The solution was removed and a second solution then added for 30 min. The cleavage solution was placed under a stream of nitrogen to remove the majority of the TFA. The remaining residue was dissolved in water and lyophilized overnight. The lyophilized solid was washed with cold ether, dissolved in water, and again lyophilized overnight. The crude material was purified was dissolved in 0.1% TFA/H$_2$O and purified by reverse-phase preparative HPLC (Waters, C18 VYDAC HPLC column, (Cat. #218TP1022) using 0.1% TFA/water (v/v) as solvent A and 0.1% TFA/AcCN (v/v) as solvent B. A starting gradient of 16.5% A and 83.5% B was used and transitioned to 19% A and 81% B over a 40 minute period. The major peak was the desired product in its reduced form which was confirmed by LC-MS and high resolution ESI-MS. The oxidized product was characterized by taking pure product, dissolving in water, and analyzed via HPLC using a gradient of 18% A to 21.5% A over 40 minutes. The second peak was identified by LC-MS and ESI-MS as the oxidized product. HRMS (ESI) calculated for C$_{61}$H$_{71}$N$_{15}$O$_{18}$S [M+H]$^{2+}$, 666.7405, found 666.7408. HRMS (ESI) calculated for C$_{110}$H$_{118}$N$_{28}$O$_{32}$S$_2$ [M+H]$^{3+}$ 888.315, found 888.313.

(R)-perfluorophenyl-2-(*tert*-butoxycarbonylamino)-3-(tritylthio)-propanoate (Boc-Cys(Trt)-Opfp) (10). To 100 mL of ethyl acetate (dried over molecular sieves for 48 hours) was added Boc-Cys(Trt)-OH (6.47 mmol, 3g). Pentafluorophenol (7.87 mmol, 1.45g) was added and the solution was cooled to 0° C, followed by the addition of DCC (6.49 mmol, 1.34 g) leading to the formation of a while precipitate. The solution was kept at 0° C for 12 hours before being removed from the ice bath. Upon removal from the ice bath, the solution stirred for an additional 12h. TLC (2.5 % MeOH/DCM) indicated complete consumption of starting material and two new spots after 24 hr

reaction time. The precipitate was filtered, the ethyl acetate evaporated under reduced pressure, and dried under vacuum. The crude product was purified via column chromatography using 1-3% MeOH in DCM (3 g, 75%) ^{1}H NMR (400 MHz, CDCl$_3$) δ 7.44 (d, 6H, J= 7.2), 7.33 (t, 6H, J= 7.6), 7.25 (t, 3H, J= 7.6), 4.95 (d, 1H, J= 7.6), 2.68 (m, 2H), 1.44 (s, 9H); ^{19}F NMR (400 MHz, CDCl$_3$) -151.55 (d, 2F, J= 23.6 Hz), -157.46 (t, 1F, J= 23.2 Hz), -162.06 (t, 2F, J= 22.4 Hz). (ESI) calculated for C$_{33}$H$_{28}$F$_5$NO$_4$S [M+H]$^+$, 629.1659 found, 629.21.

3-(7-((6S,13S)-13-(((9H-fluoren-9-yl)methoxy)carbonylamino)-2,2-dimethyl-4,7,14-trioxo-6-(tritylthiomethyl)-3-oxa-5,8,15-triazaheptadecan-17-yl)-1,3,6,8-tetraoxo-7,8-dihydrobenzo[lmn][3,8]phenanthrolin-2(1H,3H,6H)-yl)propanoic acid Fmoc-Lys(Cys(Trt))-Boc)-NDI-OH (11). To 15 ml of methylene chloride was added 2 g of the lysine-NDI monomer (Fmoc-Lys(Boc)-NDI-OH and stirred as a suspension. Then 5 mL of TFA was added and the solid immediately went into solution. After 2 h of stirring at r.t., TLC (5% MeOH/DCM) indicated complete removal of the Boc protecting group. The solution was then evaporated under reduced pressure and triturated with heptanes (3 x 50 mL) and dried under vacuum overnight. A small sample was submitted for ESI-MS analysis in MeOH and indicated the deprotected product (Fmoc-Lys-NDI-OH). The crude product (1.37 mmol, 1g) was dissolved in NMP (50 mL) followed by the addition of Oxyma Pure (1.37 mmol, 0.195 g), and Boc-Cys(Trt)-Opfp (1.37 mmol, 0.860 g). After all solids dissolved in solution, 2, 6-lutidine (4.8 mmol, 0.550 mL) was added dropwise over 5 minutes. The dark orange solution was stirred at r.t. for 48 hours. The reaction solution was diluted with 500 ml of ethyl acetate, washed with 0.1 M HCl (2x 250 mL) and was the organic layer was then divided into two separate aliquots. To each aliquot was added 300 mL of hexanes and the resulting precipitate was filtered and the material was used crude for the solid phase synthesis (2 g). ^{1}H NMR (400 MHz,

CDCl$_3$) δ 8.71 (m, 4H), 4.51), 7.81 (d, 2H), 7.61 (d, 2H), 7.41-7.23 (m, 18H), 4.79-4.68 (m, 3H), 4.56-4.42 (m, 2H), 3.81 (t, 2H), 3.56 (t, 2H), 3.47 (t, 2H), 3.25 (t, 2H), 2.73 (t, 2H), 1.38 (s, 9H), 1.29-1.18 (m, 4H). (ESI) calculated for C$_{67}$H$_{63}$N$_6$O$_{12}$S [M+H]$^+$, 1176.315, found 1176.4.

3-(2,8,9-trioxa-5-aza-1-silabicyclo[3.3.3]undecan-1-yl)proan-1-amine (APS) (12).

To a stirring solution of triethanolamine (15 mL, 113 mmoles) was added 3-aminopropyl(triethoxy)silane (APTES) (26 mL, 113 mmoles). The round bottom flask was fitted with a dean stark trap, and the solution was refluxed in an oil bath (120-150°C) for five hours. During the first three hours, a constant distillate was collected and analyzed every 1 hour by ^{1}H and ^{13}C NMR, which indicated the composition to be pure ethanol. After four hours, the rate of distillate slowed and no distillate had been collected during the last hour, indicating reaction completion. The solution was placed in the refrigerator overnight and a white precipitate had formed. The precipitate was stirred in hexanes for an hour, filtered, and dried overnight under vacuum. The white solid was crystalline in nature (15 g, 50%) ^{1}H NMR (400 MHz, CDCl$_3$) δ 3.39 (t, 6H, J= 6 Hz), 2.44 (t, 6H, J= 5.6 Hz), 2.25 (t, 2H, J= 6.8 Hz), 1.22; (m, 2H), 1.15 (m, 2H), 0.03 (t, 2H); ^{13}C (400 MHz, CDCl$_3$) δ 57.6, 51.1, 45.6, 29.7, 12.9. HRMS (ESI) calculated for C$_9$H$_{20}$N$_2$O$_3$Si [M+H]$^+$ 232.1243, found 232.2522.

BisC•Au Binding Gel (Figure 4.10). A total of nine incubations were prepared including two controls. All of the incubations contained 120 ng of linear DNA and the DNA stock solution had a concentration of 3.248 uM in binding sites (0.0781 uM in DNA x 26 binding sites per strand). For the Bis C•Au conjugate, the stock solution was 971 nM. The times on the various incubations were 92, 72, 47, 37, 28, 16, and 4 h respectively. For the control lanes, 1.5 uL of DNA stock was diluted with 18.5 uL of diH$_2$O to give a final DNA concentration of 203 nM in binding sites. One was prepared

138

and incubated for 48 hours, the other prepared within an hour of running the gel. For the time point incubations, 1.5 uL of DNA stock solution was mixed with 18.5 uL of BisC •Au to give final concentrations of 203 nM and 749 nM of DNA and BisC •Au respectively. A 2% agarose gel was then prepared by dissolving 2 g of agarose in 100 ml of TEA buffer and the gel was cast for an hour. Prior to addition to the gels, 4 uL of a 12% glycerol solution were added to all the controls and incubations. A 100 bp DNA ladder was also prepared according to NEB protocols. The gel was run at 80 V for 1.5 hours, removed, and stained with an ethidium bromide solution for 30 min. Images were acquired on a Kodak gel visualization camera and contrast was alerted to provide the strongest signals.

BisC•Au Binding Gel with G₃K Control (Figure 4.11)

The G$_3$K analog was synthesized and purified using previously established laboratory protocols in the Iverson laboratory and stock solutions of 2.1 uM G$_3$K in water and 0.02 M phosphate buffer were prepared. A stock solution of the linear DNA fragment (677 nM in binding sites) was used in all incubations. Each incubation contained DNA at a concentration of 169 nM in binding sites. The BisC •Au stock concentration was 971 uM. Two controls were prepared which contained only DNA by adding 5 uL of stock DNA with 13 uL of diH$_2$O and 13 uL of 0.02 M phosphate buffer. The BisC •Au and DNA incubation was prepared by adding 5 uL of DNA, 12.3 uL of BisC •Au, and 0.7 uL of diH$_2$O to give a final concentration of 664 nM of BisC •Au. Two G$_3$K and DNA incubations were prepared by combing 5 uL of DNA with 7.1 uL of G$_3$K, with one incubation containing 5.9 uL of diH$_2$O and another 5.9 uL of phosphate buffer. The final G$_3$K concentrations were 829 nM in both incubations. All incubations and controls were prepared 24 hours prior to running the gel. A 1.8% agarose gel was prepared and prior to adding the incubations, 3.4 uL of 12% glycerol was added to each of the incubations. A

139

100 bp DNA ladder was prepared using NEB protocols. The gel was run at 80 V for 1hr, and then increased to 90 V for an additional 30 min. The gel was stained with ethidium bromide for 30 min and images were recorded using a Kodak camera.

BisKC•Au Conjugation (Figure 4.15). The purified Bis KC was divided into several aliquots and placed in the freezer to prevent oxidation. Immediately prior to conjugation to the gold nanoparticles, Bis KC was dissolved in diH_2O and several dilutions were prepared from the stock solution which remained in the freezer. The diluted solutions concentrations were measured via UV-Vis spectroscopy to determine the concentration of the stock solution which was determined to be 3.3356×10^{-4} M. While this was occurring, 100 uL of the stock solution was analyzed via HPLC to determine the extent of oxidation. The column was equilibrated in 18% water/TFA (0.1%) and 82% MeCN/TFA (0.1%) and was increased to 21.5% water/TFA (0.1%) and 78.5% MeCN/TFA (0.1%) over 40 minutes. After confirming minimal oxidation and determining the concentration of the stock solution, 6 nmol of monomaleimido gold nanoparticles® (AuNP) were dissolved in 1.4 mL of diH_2O to provide a 4.28×10^{-6} M nanoparticle solution (measured as 4.34×10^{-6} M) in phosphate buffer (0.02 M, pH ~7, 75 mM NaCl). This brownish gold solution was vortexed several times over a five minute period. To this solution was added 17 uL of the Bis KC stock solution (1 eq, 4.05×10^{-6} M final concentration) and the reaction solution was vortexed every 30 minutes for 4 hours and then allowed to sit overnight. The total reaction time was approximately 16 hours and after this time, the reaction mixture was analyzed by UV-Vis using phosphate buffer at the above concentrations as a background control. The initial concentrations of both Bis KC and AuNP were calculated and the initial ratio was determined to be 0.85:1 of Bis KC to AuNP. Phosphate buffer (2L, 0.02 M, pH 7.4, 75 mM NaCl) was prepared and used as the dialysis solution. The reaction solution (1.4 mL) was added to a dialysis membrane

from Piercenet (molecular weight cutoff 7,000) and dialyzed against 500 mL of buffer (4 x 30 min). The solution was removed and again measured by UV-Vis to reveal a labeling efficiency of 59%. This solution was used for the Bis KC•Au binding gel.

Determination of 420/385 AuNP Absorbance Ratio (Figure 4.16)

The gold nanoparticles (6 nmol) were dissolved in 1 mL of diH$_2$O and vortexed several times over a 10 minute period. This resulted in a gold nanoparticle solution of 6.77 x 10^{-6} M in phosphate buffer (0.02 M, 75 mM NaCl, pH~7). This buffer concentration was used as the background check. Several dilutions of the gold nanoparticle solutions were performed using this buffer solution and the solution measure via UV-Vis. The first six dilutions followed 0.1 mL increments, the following three dilutions followed 0.2 mL increments, and the final two dilutions followed 0.4 mL increments. A total of 12 dilutions were used and the average ratio was 1.213.

BisKC•Au Binding Gel with G$_3$K Control (Figure 4.17)

A total of four incubations were prepared and the DNA concentration was 282 nM in binding sites for each of the incubations from a stock DNA solution 677 nM in binding sites. The BisKC •Au and BisC ex' •Au solutions were 2.177 and 4.267 uM respectively. A G$_3$K stock solution of 3.409 uM was also prepared. Lane B contained the BisKC •Au conjugate (7 uL), and 5 uL of DNA stock. Lane C contained the DNA control which contained 5 uL of DNA and 7 uL of diH$_2$O. The G$_3$K control (Lane D) incubation was prepared using 4.5 uL of G$_3$K, 2.5 uL of diH$_2$O, and 5 uL of DNA. Lane E contained BisC ex' •Au and was prepared with 5 uL DNA, 3.5 uL of BisC ex' •Au, and 3.5 uL of diH$_2$O. The incubations were prepared 24 hours prior to running the gel. A 1.85% agarose gel was prepared and cast for an hour and prior to addition to the gel, 2.4 uL of 12% glycerol was added to the incubations. The gel was run at 85 V for 2 hours. The gel

was then stained with ethidium bromide and pictures were taken using the Kodak software.

References

Aldaye, F.A.; Sleiman, H.F. Modular access to structurally switchable 3D discrete DNA assemblies. *J. Am. Chem. Soc.* **2007**, 129, 13376-13377.

Alivisatos, P.A.; Johnsson, K.P.; Peng, X.; Wilson, T.E.; Loweth, C.J.; Bruchez, M.P.; Schultz, P.G. Organization of nanocrystal molecules using DNA. *Nature.* **1996**, 382, 609-611.

Bailly, C.; Chaires, J. Sequence-Specific DNA minor groove binders. Design and synthesis of netropsin and distamycin. *Bioconj. Chem*. **1998**, 9, 513-538.

Banerjee, T.; Mukhopadhyay. Structural effects of nogalamycin, an antiobiotic antitumor agent, on DNA. *Biochem. Biophys. Res. Commun.* **2008**, 374, 264-268.

Bartlett, P.A.; Bauer, B.; Singer, S.J. Synthesis of water-soluble undecagold cluster compounds of potential importance in electron microscopic and other studies of biological systems. *J. Am. Chem. Soc.* **1978**, 100, 5085-5089.

Bates, A.D. DNA Topology. **2005**, Oxford University Press.

Berge, T.; Jenkins, N.S.; Hopkirk, R.B.; Waring, M.J. Edwardson, J.M.; Henderson, R.M. Structural perturbations in DNA caused by bis-intercalation of ditercalinium visualized by atomic force microscopy. *Nuc. Acids. Res.* **2002**, 30, 2980-2986.

Bozolla, J.J.; Russell, L.D. Electron microscopy: principles and techniques for biologists. **1999**. 2nd edition. Jones and Bartlett Publishers Inc.

Carter, J.D.; LaBean, T.H. Organization of Inorganic Nanomaterials *via* Programmable DNA Self-Assembly and Peptide Molecular Recognition. *ACS Nano.* **2010**, 5, 2200-2205.

Cases, I.; de Lorenzo, V. Promoters in the environment: transcriptional regulation in its natural content. *Nat. Rev. Microbiol*. **2005**, 3, 105-118.

Chaires, J. B.; Drug-DNA Interactions. *Curr. Opin. Struct. Biol*. **1998**, 44, 201-215.

Chu, Y.; Hoffman, D.W.; Iverson, B.L. A Pseudocatenane between DNA and a cyclic bisintercalator. *J. Am. Chem. Soc*. **2009**, 131, 3499-3508.

Claridge, S.A.; Goh, S.L.; Frechet, J.M.J.; Williams, S.C.; Micheel, C.M.; Alivisatos, P.A. Directed assembly of discrete gold nanoparticle groupings using branched DNA scaffolds. *Chem. Mater*. **2005**, 17, 1628-1635.

Clore, M.G.; Eason, P.; Nermut, M.V.; Gronenborn, A.M. Visualization of cAMP receptor protein-induced DNA kinking by electron microscopy. *J. Mol. Biol.* **1984**, 179, 751-757.

Crothers, D.M. Calculation of binding isotherms for heterogeneous polymers. *Biopolymers*. **1968**, 6, 575-584.

Crothers, D.M.; Wu, H.M. The locus of sequence-directed and protein induced DNA bending. *Nature*. **1984**, 308, 509-513.

Daniel, M.C.; Astruc, D. Gold nanoparticles: Assembly, supramolecular chemistry, quantum-size related properties, and applications towards biology, catalysis, and nanotechnology. *Chem. Rev.* **2004**, 104, 293-346.

Dervan, P.B. Molecular recognition of DNA by small molecules. *Bioorg. & Med. Chem*. **2001**, 9, 2215-2235.

Dickerson, R.; Pjura, P; Goodsell, D.; Yoon, C.; Kopka, M. The molecular origin of DNA-drug specificity in netropsin and distamycin. *Proc. Natl. Acad. Sci. USA*. **1985**, 82, 1376-1380.

Dickinson, L. A.; Gulizia, R.J.; Trauger, J.W.; Baird, E.E.; Mosier, D.E.; Gottesfeld, J.M.; Dervan, P.B. Inhibition of RNA polymerase II transcription in human cells by synthetic DNA-binding ligands. *Proc. Natl. Acad. Sci. USA*. **1998**, 95, 12890-12895.

Domborski, D.F.; Scraba, D.G.; Bradley, R.D.; Morgan, A.R. Studies of the interaction of RecA protein with DNA. *Nucl. Acids. Res*. **1983**, 11, 7487-7504.

Fernandez-Forner, D.; Casala, D.; Navarro, E.; Ryder, H.; Albericio, F. Solid-phase synthesis of 4-aminopiperidine analogues using the Alloc protecting group: an investigation of Alloc removal from secondary amines. *Tetrahedron Lett.* **2001**, 42, 4471-4474.

Fox, K.R.; Waring, M.J. *Eur. J. Biochem*. **1984**, 145, 579.

Fox, K R..; Woolley, C. The strong binding of luzopeptin to DNA. *Biochem. Pharmacol.* **1991**, 39, 941-946.

Gottesfeld, J. M.; Neely, L.; Trauger, J.W.; Baired, E.E.; Dervan, P.B. Regulation of gene expression by small molecules. *Nature*. **1997**, 387, 202-205.

Green, M.N. Avidin. *Adv. Protein Chem.* **1975**, 29, 85-133.

Griffith, J.; Cavallo, L.; Lee, S. Human p53 binds holliday junctions strongly and facilitates their cleavage. *J. Biol. Chem.* **1997**, 272, 7532-7539.

Guelev, V.; Harting, M.T.; Lokey, R.S.; Iverson, B.L. Altered sequence specificity identified from a library of DNA-binding small molecules. *Chemistry & Biology* **2000**, 7, 1-8.

Guelev, V.; Sorey, S.; Hoffman, D.W.; Iverson, B.L. Changing DNA grooves- a 1,4,5,8,-napthalene tetracarboxylic diimide bis-intercalator with the Linker (β-Ala)3Lys in the minor groove. *J. Am. Chem. Soc*. **2002**, 124, 2864-2865.

Hang, F.E.; Corcoran, J. W. Antibiotics III: Mechanism of Action of Antimicrobial and Antitumor Agents, (Springer, New York), pp. 79-100.

Haq, I.; Ladbury, J. Drug-DNA recognition: energetics and implications for design. *J. Mol. Recognit*. **2000**, 13, 188-197.

Heppelmann, B.; Segon von Blanchet, G.; Schmidt, K. Labeling of peptides with 1.4nm-gold particles to demonstrate their binding sites in the rat spinal cord. *J. Neurosci. Methods.* **1999**, 87, 195-200.

Hnilova, M.; Oren, E. E.; Seker, U. O. S.; Wilson, B. R.; Collino,S.; Evans, J. S.; Tamerler, C.; Sarikaya, M. Effect of Molecular Conformations on the Adsorption Behavior of Gold-Binding Peptides. *Langmuir* **2008**, 24, 12440–12445.

Holliday, R. A mechanism for gene conversion in fungi. *Genet. Res*. **1964**, 5, 282-304.

Huang, C.H.; Mirabelli, C.K.; Mong, S.; Crooke, S.T. Intermolecular cross-linking of DNA through bifunctional intercalation of an antitumor antibiotic, luzopeptin A. *Cancer Res*. **1983**, 43, 2718-2724.

Hyesung, J.; Shipley, G.G. Localization of the N-terminal domain of the low density lipoprotein receptor. *J. Biol. Chem.* **2000,** 275, 30465-30470.

Ivanov, V.; Grzeskowiak, K.; Zocchi, G. Evidence for an intermediate state in the B-to-Z transition of DNA. *J. Phys. Chem. B*. **2003**, 107, 12847-12850.

Kaguni, J. M. DnaA: Controlling the initiation of bacterial DNA replication and more. *Annu. Rev. Microbiol*. **2006**, 60, 351-371.

Katz, E.; Wilner, I. Integrated nanoparticle-biomolecule hybrid systems; synthesis, properties, and applications. *Angew. Chem. Int. Ed.* **2004**, 43, 6024-6108.

Kolb, A.; Spassky, A.; Chapon, C.; Blazy, B.; Buc, H. On the different binding affinities of CRP at the lac, gal, and malT promoter regions. *Nucl. Acids Res*. **1983**, 11, 7833-7852.

Le, D.J.; Pinto, Y.; Seeman, N.C. ; Musier-Forsyth, K. ; Taton, A.T. ; Kiehl, R.A. DNA-templated self-assembly of metallic nanocomponent arrays on a surface. *Nano. Lett.* **2004**, 4, 2343-2347.

Lee, J.; Guelev, V.; Sorey, S.; Hoffmann, D.W.; Iverson, B.L. NMR structural analysis of a modular threading tetraintercalator bound to DNA. *J. Am. Chem. Soc*. **2004**, 126, 14036-14042.

Lokey, R.S.; Kwok, Y.; Guelev, V.; Pursell, C.; Hurley, L.H.; Iverson, B.L. A new class of polyintercalating molecules. *J. Am. Chem. Soc*. **1997**, 119, 7202-7210.

Manning, G. S. The molecular theory of polyelectrolyte solutions with applications to the electrostatic properties of polynucleotides. *Q. Rev. Biophys*. **1978**, 97, 3930.

Mastroianni, A.J.; Claridge, S.A.; Alivisatos, P.A. Pyramidal and chiral groupings of gold nanocrystals assembled using DNA scaffolds. *J. Am. Chem. Soc.* **2009,** 131, 8455-8459.

Mazur, A. K. Titration in silico of reversible B↔A transitions in DNA. *J. Am. Chem. Soc*. **2003**, 125, 7849-7859.

McPartlin, M.; Mason, R.; Malatesta, L. Novel clusters complexes of gold (0) and gold (I). *J. Chem. Soc. D.* **1969**, 334.

Mendoza, R.; Markovitz, J.; Jaffrezou, J.P.; Muzard, G. DNaseI susceptibility of bent DNA and its alteration by ditercalinium and distamycin. *Biochemistry*. **1990**, 29, 5035-5043.

Meyer, R.R.; Laine, P.S. The single-stranded DNA-binding protein of Escherichia coli. *Microbiol. Mol. Biol. Rev.* **1990**, 54, 342-380.

Mirkin, C.A.; Letsinger, R.L.; Mucic, R.C.; Storhoff, J.J. A DNA-based method for rationally assembling nanoparticles into macroscopic materials. *Nature.* **1996**, 382, 607-609.

Morrical, S.W.; Lee, J.; Cox, M.M. Continuous association of Escherichia coli single-stranded DNA binding protein with stable complexes of recA protein and single-stranded DNA. *Biochemistry*, **1986**, 25, 1482-1494.

Mucic, R.C.; Storhoff, J.J.; Mirkin, C.A.; Letsinger, R.L. DNA-directed synthesis of binary network nanoparticle materials. *J. Am. Chem. Soc.* **1998**, 120, 12674-12675.

Murray, R.W.; Zhang, J.; Wang, G. DNA binding of an ethidium intercalator attached to monolayer-protected gold cluster. *Anal. Chem.* **2002**, 74, 4320-4327.

Nangreave, J.; Han, D.; Liu, Y.; Yan, H. DNA origami: a history and current perspective. *Curr. Opin. Chem. Biol.* **2010**, 14, 608-615.

Niemeyer, C.M.; Burger, W.; Peplies, J. Covalent DNA–Streptavidin Conjugates as Building Blocks for Novel Biometallic Nanostructures. *Angew. Chem. Int. Ed.* **1998**, 37, 2265-2268.

Noyong, M.; Gloddek, K.; Ulrich, S. Assembly of gold nanoparticles on DNA strands. *Mat. Res. Soc. Symp. Proc.* **2002** 735, 153-158.

Park Scientific Instruments. A practical guide to scanning probe microscopy. **1997**.

Park, S.H.; Yin, P.; Liu, Y.; Reif, J.H.; LaBean, T.H.; Yan, H. Programmable DNA self-assemblies for nanoscale organization of ligands and proteins. *Nano Lett.* **2005**, 5, 729-733.

Patikoglu, G.; Burley, S. K. Eukaryotic transcription factor-DNA complexes. *Ann. Rev. Biophys. Biomol. Struct*. **1997**, 26, 289-325.

Patolsky, F.; Weizmann, Y.; Lioubashevski, O.; Willner, I. Au-nanoparticle nanowires based on DNA and polylysine templates. *Angew. Chem. Int. Ed.* **2002**, 41, 2323-2327.

Pelton, J.G.; Weemer, D.E. Structural characterization of a 2:1 distamycin A·d(CGCAAATTGGC) complex by two-dimensional NMR. *Proc. Natl. Acad. Sci. USA*. **1989**, 86, 5723-5727.

Qiu, H.; Dewan, J.C.; Seeman, N.C. A DNA decamer with a sticky end: The crystal structure of d-CGACGATCGT. *J. Mol. Biol.* **1997**, 267, 881-898.

Reddy, M.S.; Moreshwar, B.; Vaze, M.K.; Muniyappa, K. Binding of SSB and RecA Protein to DNA-Containing Stem Loop Structures: SSB Ensures the Polarity of RecA Polymerization on Single-Stranded DNA. *Biochemistry*, **2000**, 39, 14250-14262.

Safer, D.; Hainfeld, J.; Wall, J.S.; Reardon, J.E. Biospecific labeling with undecagold: Visualization biotin-binding site on avidin. *Science* **1982**, 218, 290-291.

Savva, C. Texas A&M University Electron Microscopy Imaging Center.

Sawaya, M.R. *et al.* Atomic structures of amyloid cross-β spines reveal varied steric zippers. *Nature*. **2007**, 447, 453-457.

Schnos, M.; Ingman, R.B. Applications of electron microscopy for studying protein-DNA complexes. *Electron Microscopy Methods and Protocols*. **1999,** 117, 229-243.

Seeman, N.C. At the crossroads of chemistry, biology, and materials: structural DNA nanotechnology. *Chem. Biol.* **2003,** 10, 1151-1159.

Seeman, N.C. Nucleic acids junctions and lattices. *J. Theor. Biol.* **1982,** 99, 237-247.

Seeman, N.C. Overview of structural DNA nanotechnology. *Mol. Biotechnol.* **2007**, 37, 246-257.

Sharma, J.; Chhabra, R.; Cheng, A.; Brownell, J.; Liu, Y.; Yan, H. Control of self-assembly of DNA tubules through integration of gold nanoparticles. *Science.* **2009**, 323, 112-116.

Sharma, N.; Top, A.; Kiick, K.L.; Pochan, D.J. One-Dimensional gold nanoparticle arrays by electrostatically directed organization using polypeptide self-assembly. *Angew. Chem. Int. Ed.* **1998**, 48, 7078-7082.

Shlyakhtenko, L.S.; Gall, A.A.; Filonov, A.; Cerovac, Z.; Lushnikov, A.; Lyubchencko, Y.L. Silatrane based surface chemistry for immobilization of DNA, protein-DNA, complexes and other biological materials. *Ultramicroscopy.* **2003**, 97, 279-287.

Slim, M.; Durisic, N., Grutter, P. and Sleiman, H. F. DNA–Protein Noncovalent Cross-Linking: Ruthenium Dipyridophenazine Biotin Complex for the Assembly of Proteins and Gold Nanoparticles on DNA Templates. *ChemBioChem.* **2007**, 8, 804-812.

Spolar, R.; Record, M.T. Coupling of local folding to site-specific binding of proteins to DNA. *Science.* **1994**, 263, 777-784.

Top, A.; Kiick, K.L.; Roberts, C.J. Modulation of Self-Association and Subsequent Fibril Formation in an Alanine-Rich Helical Polypeptide. *Biomacromolecules.* **2008**, 9, 1595-1603.

Tseng, Y.D.; Ge, H.; Wang, X.; Edwardson, J.M.; Waring, M.J.; Fitzgerald, W.J.; Henderson, R.M. Atomic force microscopy study of the structural effects induced by echinomycin binding to DNA. *J. Mol. Biol.* **2005**, 345, 745-758.

Waring, M.J. Variation of the supercoils in closed circular DNA by binding of antibiotics and drugs. Evidence for molecular models involving intercalation. *J. Mol. Biol.* **1970**, 54, 247.

Westerlund, F.; Bjornhold, T.; Directed assembly of gold nanoparticles. *Curr. Opin. Colloid Interface Sci.* **2009**, 14, 126-134.

White, S.; Baird, E. E.; Dervan, P.B. On the pairing rules for recognition in the minor groove of DNA by pyrrole-imidazole polyamides. *Chem. Biol.* **1997**, 4, 569-578.

Williams, L.D.; Egli, M.; Gao, Q.; Bash, P.; Van Der Marel, G.A.; Frederick, C.A. Structure of nogalamycin bound to a DNA hexamer. *Proc. Natl. Acad. Sci. USA*. **1990**, 87, 2225-2229.

Willner, I.; Willner, B. Biomolecule-Based nanomaterials and nanostructures. *Nano Lett.* **2010**, 10, 3805-3815.

Wilson, W.D.; Tanious, F.; Yen, S. Kinetic and equilibrium analysis of a threading intercalation mode: DNA sequence and ion effects. *Biochemistry*. **1991**, 30, 1813-1819.

Winfree E.; Furong, W.; Lisa, A.; Seeman, N.C. Design and self-assembly of two-dimensional DNA crystals. *Nature*. **2003**, 394, 539-544.

Woehrle, G.H.; Warner, M.G.; Hutchison, J.E. Molecular-Level Control of Feature Separation in One-Dimensional Nanostructure Assemblies Formed by Biomolecular Nanolithography. *Langmuir* **2004,** 20, 5982-5988.

Zou, B.; Ceyhan, B.; Simon, U.; Niemeyer, C.M. Self-assembly of cross-linked DNA-gold nanoparticle layers visualized by in-situ scanning force microscopy. *Adv. Mater.* **2005**, 17, 1643-1647.

Zweng, J.; Constantinou, P.E.; Micheel, C.; Alivisatos, P.A.; Kiehl, R.A.; Seeman, N.C. Two-Dimensional nanoparticle arrays show the organizational power of robust DNA motifs. *Nano. Lett.* **2006**, 6, 1502-1504.

Michael L. Elmuccio was born in Brooklyn, NY and spent his childhood growing up in north Ogdensburg, NJ. He was inspired to begin a career in chemistry after completing his high school chemistry class taught by Mr. George Lyons. He received a Bachelor's degree in Chemistry from The Pennsylvania State University in 2007 and spent his spare time as an elite leader of the Penn State football student section along with the inspirational Colin K. McGowan, which was named the best student section in the country during the 2005 and 2006 football seasons and has remained as one of the best since that time. In the fall of 2007, he began his graduate career at the University of Texas and joined Dr. Iverson's group to further his knowledge in the field of bio-organic chemistry. The interdisciplinary approach to his research project has prepared him well for a challenging career in either a bio-organic or government laboratory.

Permanent Address:

elmuccio@gmail.com

This thesis was typed by the author.